Rod-Coil Copolymer Structures - Scaling and Field Theory

Dissertation
zur Erlangung des Grades

"Doktor der Naturwissenschaften"

am Fachbereich Physik
der Johannes Gutenberg-Universität
in Mainz

Christian Nowak
geb. in Hannover

Mainz, den 19. Januar 2006

Für Miriam

Zusammenfassung

In dieser Arbeit werden Copolymere, die abwechselnd aus steifen Stäbchen und flexiblen Ketten zusammengesetzt sind (Rod-Coil Copolymere), mit Hilfe von Skalenbetrachtungen und feldtheoretischen Rechnungen untersucht.

Skalenargumente werden verwendet, um Rod-Coil Copolymere mit fester Zusammensetzung von steifen Stäbchen und flexiblen Ketten zu studieren. In einem selektiven Lösungsmittel, in dem sich nur die Ketten lösen, bildet ein Rod-Coil Multiblock zylinderförmige Micellen aus aggregierten Stäbchen verbunden durch flexible Kettenstücke. Die Stäbchen aggregieren, um Energie zu gewinnen. Dieser Prozeß wird durch den Entropieverlust der flexiblen Ketten ausgeglichen. Für Einzelmicellen-Konfigurationen wird die mittlere Anzahl an aggregierten Stäbchen berechnet, für Multimicellen-Konfigurationen die mittlere Anzahl der Micellen. Die Auffaltung einer einzelnen Micelle unter dem Einfluß einer externen Kraft wird für den Fall quasistatischen Ziehens untersucht. Für physikalisch sinnvolle Parameter kann der Auffaltungsprozeß in einem Schritt geschehen. Die Kraft-Ausdehnungskurve weist dann ein großes Plateau auf.

Das Adsorptionsverhalten von Aggregaten aus einzelnen Rod-Coil Diblöcken in selektivem Lösungsmittel wird anhand von erweiterten Skalenbetrachtungen diskutiert. Es wird angenommen, daß sich die Stäbchen ausschließlich parallel aneinanderlagern und somit ein Maximum an Energie gewinnen, wenn sie flüssig-kristalline Strukturen bilden. Wenn ein solches Aggregat mit den Stäbchen parallel zur Oberfläche adsorbiert, verschieben sich die Stäbchen gegeneinander, um es den Ketten zu ermöglichen Entropie zu gewinnen. Das Profil dieser Verschiebung wird berechnet, indem die freie Energie des Systems minimiert wird. Zusätzlich werden die Stabilität der adsorbierten Aggregate und andere an der Oberfläche mögliche Konfigurationen untersucht.

Um einen Rod-Coil Multiblock mit variabler Zusammensetzung zu studieren, wird eine Feldtheorie entwickelt. Jedes Segment kann entweder steif oder flexibel sein. Zwei Felder werden eingeführt, eines für die flexiblen und eines für die steifen Segmente. Um eine variable Zusammensetzung zu ermöglichen, wird das großkanonische Ensemble verwendet. Die Theorie wird im Rahmen der selbstkonsistenten Feld Approximation behandelt. Die Differentialgleichungen, durch die die selbstkonsistenten Felder bestimmt werden, werden numerisch mit Hilfe von Finite Elemente Methoden gelöst. Das System zeigt drei Phasenzustände, offene Kette, amorphe Globule und flüssig-kristalline Globule. Die flüssig-kristalline Globule bildet sich ohne eine explizit winkelabhängige Wechselwirkung zwischen den Stäbchen. Beim Übergang von amorpher zu flüssig-kristalliner Globule steigt der Anteil an steifen Segmenten rapide an. Es wird gezeigt, daß dieser Übergang durch die isotrope Zwei-Körper-Wechselwirkung zwischen den steifen Segmenten und die anisotrope Oberflächenenergie der Globule verursacht wird.

Abstract

In this thesis rod-coil copolymers are theoretically investigated by means of scaling methods and field theory.

Scaling arguments are used to study rod-coil copolymers with a fixed composition of stiff rods and flexible chain parts. A rod-coil multiblock immersed in a solvent selective for the flexible parts forms cylindrical micelles of aggregated rods connected by flexible chain parts. The rods aggregate in order to lower the energy. This process is counterbalanced by the loss of entropy of the flexible parts. For single micelle configurations the average aggregation number of rods is calculated and for multi-micelle configurations the average number of micelles. The unfolding of a single micelle under an external force is investigated for the case of quasi static pulling. It is shown that for physically reasonable parameters the unfolding process is likely to be a one-step process with one large plateau in the force-extension curve.

The adsorption behaviour of an aggregate of individual rod-coil diblocks in selective solvent is discussed by means of extended scaling methods. The rods are assumed to align only parallel to each other, so that they gain a maximum energy by forming liquid-crystalline structures. It is shown that, if an aggregate of these copolymers adsorbs with the rods parallel to the surface, the rods shift with respect to each other to allow the chains to gain entropy. The profile of this shift away from the surface is calculated by minimisation of the free energy of the system. In addition, the stability of such an adsorbed aggregate and other possible configurations at the surface are discussed.

A field theory is constructed to study a rod-coil multiblock with variable composition. Each segment can adopt one of two states, stiff or flexible. Two fields are introduced. One is associated with the flexible segments and one with the stiff segments. To allow for a variable composition a grand canonical ensemble formulation is used. The theory is treated in the self-consistent field approximation. The differential equations which determine the self-consistent fields are solved numerically with finite element methods. The system shows three different phase states, open chain, amorphous globule and nematic liquid-crystalline globule. The formation of the liquid-crystalline globule occurs without an orientation dependent alignment interaction between the rods. The crossover transition from amorphous to liquid-crystalline globule coincides with a rapid increase in the fraction of stiff segments. It is shown that this transition is driven by the isotropic two-body interaction between stiff segments and the anisotropy of the globule surface energy.

Contents

List of Figures

1. Introduction

Polymers are a very diverse and multi-functional class of materials [1]. Synthetic polymers are used for many purposes, for instance in cling film, plastic bags and high performance materials for the clothing industry. It is also possible to design specific self assembling micro- and nanostructures with polymers. In the future, a new generation of semiconductor devices of polymeric origin might be formed by self assembly. An even wider range of polymers can be found in living matter [2], such as DNA, RNA and proteins.

A Polymer is a chain molecule, characterised by the repetition of small chemical units (monomers) connected to each other by covalent bonds. In the case of a homopolymer all these repeat units are the same. Some polyesters are examples of such polymers. If a polymer consists of chemically different monomers, it is called a heteropolymer. DNA or proteins are examples of heteropolymers. Apart from single linear chains there are also topologically more complex variants of polymers or polymer compounds such as stars, combs, networks or brushes, see Figs.(1.1,1.2)

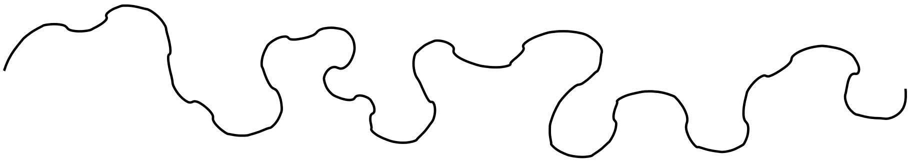

Figure 1.1: Linear Polymer chain

Different polymers can be dissolved in different solvents. These solvents can vary in quality [1]. A solvent is referred to as good if the polymer is easily dissolved in it. This gives rise to effective repulsive interactions between the monomers and the polymer adapts a very open state of low density. A solvent is referred to as poor if the polymer does not like to be dissolved in it. This gives rise to effective attractive interactions between the monomers, and the polymer adapts a globular state of high density. In between these two solvent conditions is the Θ-regime which corresponds to a cancellation between steric repulsion and van der Waals attraction between the monomers. For many polymer-solvent systems the quality of the solvent is a decreasing function of temperature. These qualitative characterisations will be

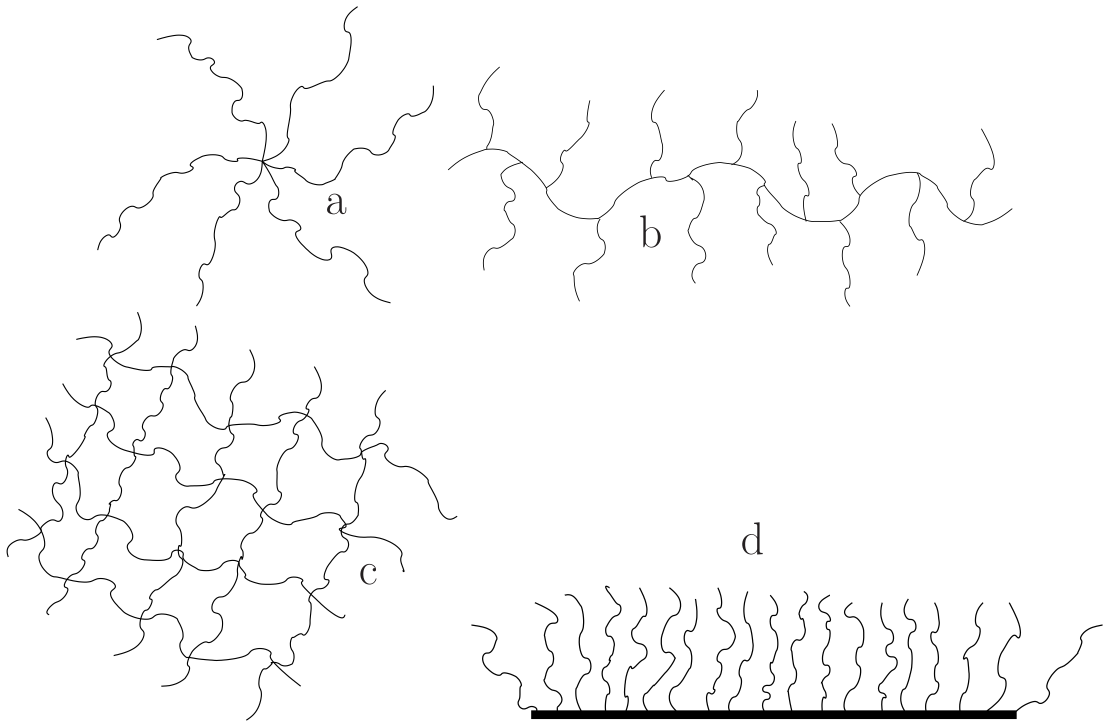

Figure 1.2: Different polymer topologies: a) star-polymer, b) comb-polymer, c) polymer network, d) polymer brush

put in a more formal description in Chapter 2. A dense system of polymers in the absence of solvent can form a bulk liquid state which is referred to as polymer melt.

This work focuses on a special kind of polymers called rod-coil copolymers. Rod-coil multiblock copolymers are heteropolymers which are composed of multiple alternating blocks of flexible chains and stiff rods, see Fig.(1.3). In a melt, rod-coil multiblock copolymers are able to self assemble into supramolecular structures [3–7]. These structures, assembled by the rod segments in rod-coil systems include, for example sheets, cylinders, finite nanostructures and even 1,2 or 3 dimensional lattices [7]. To which structure the system assembles depends on the length and diameter of the

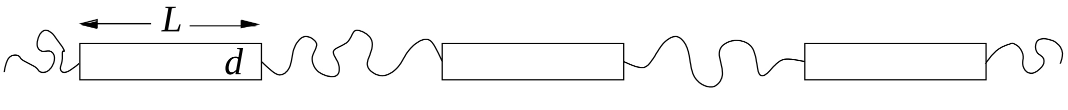

Figure 1.3: This figure shows a rod-coil multiblock copolymer with rods of length L and diameter d. The stiff rods are connected by flexible chain parts.

rods and the length and flexibility of the chains. When dissolved in a selective solvent, usually a solvent which is good for the flexible parts and poor for the stiff parts, rod-coil multiblocks segregate into distinct microdomains. These microdomains can also form supramolecular structures [7]. In this case the adopted structures depend also on the quality of the solvent. Rod-coil copolymers are therefore good candidates to design self-assembled materials with specific physical properties.

Not only the bulk properties of rod-coil copolymers in the melt or in solution are of interest, but also the properties of a single rod-coil multiblock copolymer immersed in a selective solvent. Such a polymer shows a rich phase behaviour. The rods can aggregate to form highly oriented, liquid-crystalline-like structures. Depending on the geometric properties of the rods, the length of the flexible chains and the quality of the solvent, they might form one big cylindrical micelle, several connected micelles or no aggregates at all. Hence a rod-coil multiblock copolymer can serve as a model system for many exemplary studies of various physical phenomena with specific interactions and geometrical or steric restrictions. As will be shown at the end of Chapters 3 and 8 it might also provide a simple physical explanation for the formation of helix bundles in certain proteins.

Two different kinds of rod-coil copolymers are considered in this work. Copolymers with a fixed composition of stiff and flexible parts as shown in Fig.(1.3) and copolymers with a variable composition of stiff and flexible parts. Variable composition means that each segment can either form a flexible part or a stiff part. The equilibrium composition of stiff and flexible parts is determined by the specific structure formed by the complete polymer. On the other hand, these specific structure is also influenced by the composition of stiff and flexible parts. This interplay of microscopic (a segment can be either flexible or stiff) and mesoscopic structure gives rise to a very interesting phase behaviour as will be shown in Chapter 8. Helix-forming polymers, for instance polypeptides, are polymers which a show a variable composition of stiff and flexible segments. Each segment of such a polymer can either stay flexible and disordered or coil up to a helix. These helices are usually very stiff (for instance due to the formation of hydrogen bonds between their turns, which leads to a persistent length of $l_{\mathrm{p}} \sim 100$ nm [8]) and can therefore be regarded as rods.

Each of the two kinds of rod-coil copolymers is investigated by a different technique. Thus the thesis can be divided into two parts. The first part includes Chapters 3-5 in which copolymers of fixed composition are investigated using scaling methods. The second part includes Chapters 6-8 in which copolymers with variable composition are investigated by means of a self-consistent field theory.

The detailed outline of the thesis is as follows:

- Chapter 2 gives an introduction to some of the theoretical concepts used to describe polymers. It starts with the description of an ideal polymer chain as a random walk. The self avoiding walk of a real chain is briefly discussed. Scaling methods and in particular the notion of a blob are introduced. Finally, the force-extension behaviour of a real chain under tension is described.
- In Chapter 3 rod-coil multiblock copolymers of fixed composition are discussed by means of scaling arguments. The configurations of a single rod-coil copolymer in a selective solvent and their stability are considered in detail. It is shown, that the copolymer can form stable single and multi-micelle configurations. The equilibrium size and number of these micelles is calculated. The predicted micelle size is compared to experimental values for helix-bundles in proteins.
- Chapter 4 describes how a rod-coil multiblock copolymer forming one micelle unfolds under an external force. This corresponds to a single molecule experiment with an atomic force microscope or an optical tweezer. An example of a typical force-extension curve is calculated and the influence of finite extensibility of the flexible parts is briefly discussed.
- An excursion to rod-coil diblock copolymers is made in Chapter 5. The adsorbtion behaviour of aggregates of these diblocks at a surface is discussed by means of an extended scaling theory. The diblocks are assumed to aggregate with the rods being aligned parallel to each other such that the chains all stick out to one side. If such an aggregate adsorbs to a surface the rods shift with respect to other. The explicit form of this shift is calculated. In addition, other possible configurations close to the surface are discussed.
- The self-consistent field theory for copolymers with variable composition is derived in Chapter 6. A grand canonical formulation is used to allow for a variable composition. Two fields are introduced, a position and orientation dependent one associated with the stiff segments and a position dependent one associated with the flexible segments. The details of the field theoretical representation of the partition function are discussed in Appendix A. As a simplification for the subsequent numerical calculations the field associated with the stiff segments is expanded in Legendre polynomials which makes it possible to integrate out the orientation dependence.
- In Chapter 7 the self-consistent field equations for a flexible homopolymer are solved numerically and the coil-globule transition of the homopolymer is studied as a test case. The numerical routines used to solve the differential equations in Chapters 7 and 8 are briefly described in Appendix B.

- The numerical results of the full self-consistent field equations for the copolymer are presented in Chapter 8. The coil-globule transition of the copolymer is investigated as well as the change in the composition in terms of fraction of stiff segments. An additional crossover transition from an amorphous disordered globule to a nematic liquid-crystalline globule with high fraction of stiff segments can be observed. This transition is studied in great detail and its relevance for helix-bundle formation in proteins is discussed.
- Finally, conclusions are drawn in Chapter 9. The chapter also presents an outlook on further interesting investigations for future work.

Parts of this thesis have already been published or have been submitted for review, i.e. in [11–14].

2. Description of polymers - basic aspects

2.1. Random walk of a flexible chain

The simplest model of a polymer is the ideal polymer chain [8]. In an ideal chain the monomers are simply connected segments without any correlations. The polymer configuration performs a random walk in space. The mean square end-to-end distance of a chain consisting of N segments (or monomers) each of length b is given by

$$\begin{aligned} R_{\mathrm{e}}^2 = &= \left\langle (\mathbf{R}_N - \mathbf{R}_1)^2 \right\rangle = \left\langle \left(\sum_{n=1}^{N} [\mathbf{R}_{n+1} - \mathbf{R}_n] \right)^2 \right\rangle \qquad (2.1) \\ &= \left\langle \left(\sum_{n,m=1}^{N} [\mathbf{R}_{n+1} - \mathbf{R}_n][\mathbf{R}_{m+1} - \mathbf{R}_m] \right) \right\rangle = \left\langle \sum_{n=1}^{N} [\mathbf{R}_{n+1} - \mathbf{R}_n]^2 \right\rangle \\ &= Nb^2. \end{aligned}$$

The second to last equality holds due to the absence of correlations. Only the diagonal terms contribute to the average.

In real polymers neighbouring monomers are correlated due to finite rotational and bending stiffness of the covalent bonds between the monomers. However, the directional correlation of two monomers diminishes exponentially with the growth of the chain length separating them [8]. The constant characterising this exponential decay for each specific polymer is called persistence length l_{p}. Knowing the persistence length it is possible to describe the polymer as an ideal chain with l_{p} being the effective segment length b.

An experimentally accessible measure for the size of a polymer is the radius of gyration

$$R_{\mathrm{gyr}} = \left(\frac{1}{2N^2} \sum_{n,m=1}^{N} \left\langle [\mathbf{R}_n - \mathbf{R}_m]^2 \right\rangle \right)^{1/2} = \left(\frac{1}{N} \sum_{n=1}^{N} \left\langle [\mathbf{R}_{\mathrm{cm}} - \mathbf{R}_n]^2 \right\rangle \right)^{1/2}, \qquad (2.2)$$

where $\mathbf{R}_{\mathrm{cm}}$ denotes the position of the centre of mass of the chain. As can be seen from Eq.(2.2) the radius of gyration averages over all distances between monomers on a chain. It can be measured for instance by small angle neutron scattering or light scattering [9].

For the ideal chain the radius of gyration is related to the mean square end-to-end distance by [9]

$$R_{\mathrm{gyr}}^2 = \frac{R_{\mathrm{e}}^2}{6}. \tag{2.3}$$

For long chains $N \gg 1$ the end-to-end vector $\mathbf{R}_{\mathrm{e}} = \mathbf{R}_N - \mathbf{R}_1$ obeys a Gaussian distribution

$$P(\mathbf{R}_{\mathrm{e}}) = \left(\frac{3}{2\pi R_{\mathrm{e}}^2}\right)^{3/2} \exp\left(-\frac{3R_{\mathrm{e}}^2}{2Nb^2}\right). \tag{2.4}$$

Therefore an ideal polymer chain is also called Gaussian chain. Several segments can be combined to a new segment of length $b' > b$. The end-to-end vector of a chain built up from these longer segments also obeys a Gaussian distribution in Eq.(2.4). The specific local structure of the chain is not necessary to describe its behaviour on larger scales. The chain is Gaussian on all scales and thus scale invariant (provided that $b > l_{\mathrm{p}}$).

An end-to-end distance dependent entropy can be defined as follows

$$S(\mathbf{R}_{\mathrm{e}}) = k_{\mathrm{B}} \ln(P(\mathbf{R}_{\mathrm{e}})) + S_0 = -\frac{3k_{\mathrm{B}}R_{\mathrm{e}}^2}{2Nb^2} + S_0. \tag{2.5}$$

The entropy defined above has its maximum at $\mathbf{R}_{\mathrm{e}} = 0$, that is the chain reacts to stretching with a restoring force $\mathbf{K}(\mathbf{R}_{\mathrm{e}})$ of entropic nature. It acts like a spring with spring constant $\frac{3k_{\mathrm{B}}T}{2Nb^2}$.

$$\mathbf{K}(\mathbf{R}_{\mathrm{e}}) = T\frac{\mathrm{d}}{\mathrm{d}\mathbf{R}_{\mathrm{e}}}S(\mathbf{R}_{\mathrm{e}}) = -\frac{3k_{\mathrm{B}}T}{Nb^2}\mathbf{R}_{\mathrm{e}} \tag{2.6}$$

For a Gaussian chain not only the probability of the end-to-end vector obeys a Gaussian distribution but also every distance vector $\mathbf{r}_{nm} = \mathbf{R}_n - \mathbf{R}_m$ between two segments n and m along the chain.

$$P(\mathbf{r}_{nm}) = \left(\frac{3}{2\pi|n-m|b^2}\right)^{3/2} \exp\left(-\frac{3r_{nm}^2}{2|n-m|b^2}\right). \tag{2.7}$$

Consider the probability distribution for the distance between neighbouring segments

$$P(\mathbf{r}_{nn+1}) = \left(\frac{3}{2\pi b^2}\right)^{3/2} \exp\left(-\frac{3r^2_{nn+1}}{2b^2}\right). \tag{2.8}$$

The entire conformational distribution function of the Gaussian chain is then given by

$$\begin{aligned}\Psi\left(\{\mathbf{r}_{nn+1}\}\right) &= \prod_{n=1}^{N} \left(\frac{3}{2\pi b^2}\right)^{3/2} \exp\left(-\frac{3r^2_{nn+1}}{2b^2}\right) \\ &= \left(\frac{3}{2\pi b^2}\right)^{3/2} \exp\left(\sum_{n=1}^{N} -\frac{3(\mathbf{R}_{n+1}-\mathbf{R}_n)^2}{2b^2}\right). \end{aligned} \tag{2.9}$$

The Gaussian chain is often represented by a mechanical model of $N+1$ beads connected by harmonic springs. The potential energy of such a chain of beads and springs is given by

$$U\left(\{\mathbf{R}_n\}\right) = \frac{3k_{\mathrm{B}}T}{2b^2} \sum_{n=1}^{N} (\mathbf{R}_{n+1}-\mathbf{R}_n)^2. \tag{2.10}$$

The Boltzmann distribution of such a bead spring model at equilibrium is exactly the same as Eq.(2.9).

It is often useful to regard the suffix n of the Gaussian chain as a continuous variable. The continuum limit is taken as follows [10]

$$\begin{aligned}\mathbf{R}_{n+1}-\mathbf{R}_n &\rightarrow \frac{\partial \mathbf{R}_n}{\partial n} \\ \sum_{n=1}^{N} &\rightarrow \int_0^N \mathrm{d}n. \end{aligned} \tag{2.11}$$

Eq.(2.9) can then be written in continuous form as

$$\Psi\left(\mathbf{R}_n\right) = \mathcal{N} \exp\left(-\frac{3}{2b^2} \int_0^N \left(\frac{\partial \mathbf{R}_n}{\partial n}\right)^2\right). \tag{2.12}$$

The distribution given by Eq.(2.12) is called Wiener distribution. For a detailed mathematical discussion of the continuum limit defined above, see [43].

2.2. Real chains

In the previous section the segments along the polymer backbone were assumed not to interact with each other. In a real polymer chain the segments do interact. A polymer cannot cross itself. Two segments cannot be at the same position, which they could if the chain was described by a random walk as in the case of an ideal or Gaussian chain. Under good solvent conditions this leads to a description of the polymer as a self avoiding walk. Self avoidance just means that the walk cannot return to a position where it has already been, i.e. two segments of the polymer cannot be at the same spatial position. This can be achieved by introducing a repulsive interaction between the polymer segments. Hence the polymer swells if immersed in a good solvent. This is referred to as the excluded volume effect.

To introduce interactions it is convenient to consider the canonical partition function

$$Z = \int \mathcal{D}\mathbf{R}(n) \exp(-\beta H(\{\mathbf{R}(n)\})), \tag{2.13}$$

where $\beta = 1/k_{\mathrm{B}}T$. The Hamiltonian H_0 for a non-interacting polymer chain reads

$$\beta H_0(\{\mathbf{R}(n)\}) = \frac{3}{2b^2} \int_0^N \mathrm{d}n \left(\frac{\partial \mathbf{R}}{\partial n} \right)^2 . \tag{2.14}$$

Now interactions can be introduced. To model good solvent conditions it is sufficient to introduce a repulsive two-body interaction. For simplicity, this is usually done by means of a point contact interaction

$$\beta H_{\mathrm{int}} = \frac{v}{2} \int_0^N \mathrm{d}n \int_0^N \mathrm{d}m\, \delta(\mathbf{R}(n) - \mathbf{R}(m)). \tag{2.15}$$

The interaction constant v determines the strength of the interaction. Its given by

$$v = b^3 \left(1 - \frac{\Theta}{T} \right) \equiv b^3 \tau, \tag{2.16}$$

where b^3 is the volume of one segment and Θ is the temperature at which v vanishes and the chain becomes ideal and behaves like a Gaussian one. The dimensionless parameter τ is called reduced temperature.

$H_{\mathrm{E}} = H_0 + H_{\mathrm{int}}$ is called Edwards Hamiltonian. To model poor solvent conditions a three-body interaction has to be introduced. This will be discussed in detail in Chapter 6.

As already mentioned, a polymer coil in good solvent swells. Hence the mean square end-to-end distance R_{e} is larger than the one for an ideal chain, compare Eq.(2.1).

An exact calculation of R_e for the interacting polymer is impossible. For the ideal chain R_e is proportional to $N^{1/2}$. Hence, for the real chain in good solvent R_e must be proportional to N^ν, with the excluded volume exponent $\nu > 1/2$. Significant work has been done to calculate this exponent [10]. The Flory argument [15] yields a simple though surprisingly good estimate for R_e. The size of the polymer is given by the balance of two effects. The repulsive two-body excluded volume interaction tries to swell the polymer. On the other hand the elastic energy arising from the chain connectivity tries to shrink the polymer. Recalling the expression for the entropy in Eq.(2.5), the free energy of a non-interacting chain as a function of end-to-end vector $\mathbf{R}_\mathrm{e}$ is given by

$$F(\mathbf{R}_\mathrm{e}) = k_\mathrm{B}T\frac{3R_\mathrm{e}^2}{2Nb^2} + F_0. \tag{2.17}$$

The effect of the excluded volume interaction is estimated by considering a segment gas confined to a volume R_e^3. The interaction energy can then be estimated as $vk_\mathrm{B}T\bar{c}^2R_\mathrm{e}^3$, where the average concentration is - up to numerical prefactors - given by $\bar{c} \simeq N/R_\mathrm{e}^3$. The free energy of the interacting polymer is thus approximatively given by

$$\beta F(\mathbf{R}_\mathrm{e}) \simeq \frac{3R_\mathrm{e}^2}{2Nb^2} + v\frac{N^2}{R_\mathrm{e}^3} + \beta F_0. \tag{2.18}$$

Minimisation of F with respect to R_e yields the mean square end-to-end distance

$$R_\mathrm{e} \simeq b\left(\frac{v}{b^3}\right)^{1/5} N^{3/5} \to \nu \approx 3/5. \tag{2.19}$$

The value of the excluded volume exponent $\nu \approx 3/5$ is very close to the actual value obtained by more refined techniques such as perturbation calculation [16]. This gives the following value of ν

$$\nu = 0.588 \pm 0.001. \tag{2.20}$$

In the following chapters the value $\nu = 3/5$ will be used.

For good solvent (at high temperature $T \gg \Theta$) it is quite common to set the excluded volume parameter equal to the volume occupied by one monomer, i.e. $v \simeq b^3$. Eq.(2.19) reduces then to

$$R_\mathrm{e} \simeq bN^\nu, \tag{2.21}$$

which can be used in both the good solvent ($\nu = 3/5$) and Θ-solvent ($\nu = 1/2$) case. Eq.(2.21) will be used frequently in Chapters 3 and 4.

2.3. Scaling and the blob picture

For the discussion of rod-coil multiblock copolymers of fixed composition in Chapters 3, 4 and 5 scaling arguments are used. The general ideas are introduced in this section with a simple example.

Consider a real polymer chain (good solvent conditions) trapped in a thin tube [41]. The diameter D of the tube is assumed to fulfil $b \ll D \ll R_\mathrm{e}$. The length of the polymer parallel to the tube $R_\parallel$ and the energy required to squeeze the chain in the tube are estimated below.

Since R_e and D are the only relevant length scales in the problem, the length $R_\parallel$ must have the scaling form

$$R_\parallel = R_\mathrm{e}\, g\left(\frac{R_\mathrm{e}}{D}\right), \tag{2.22}$$

where $g(x) \to 1$ for $x \to 0$ ($D \to \infty$: thick tube) and $g(x) \to x^m$ for $x \to \infty$ ($D \to 0$: thin tube). For a thin tube the problem becomes one-dimensional and $R_\parallel$ must be proportional to N. On the other hand, $R_\mathrm{e} \sim N^{3/5}$. This yields

$$N^{3/5(1+m)} \simeq N \Rightarrow m = \frac{2}{3}. \tag{2.23}$$

The length of the chain in the tube is hence given by

$$R_\parallel \simeq Nb\left(\frac{b}{D}\right)^{2/3}, \tag{2.24}$$

or for general exponent ν

$$R_\parallel \simeq Nb\left(\frac{b}{D}\right)^{1/\nu-1}. \tag{2.25}$$

There is also another way to derive Eq.(2.24). The tube diameter sets a length scale in the problem. This length can be associated with the size of a blob [41], see Fig.(2.1). The chain is confined to the tube and therefore behaves as a sequence of blobs of diameter D. Inside the blobs the chain is undisturbed and still behaves like a self-avoiding walk. The number of monomers per blob n_B is therefore given by

$$D \simeq n_\mathrm{B}^{3/5} b. \tag{2.26}$$

As it is pictured in Fig.(2.1), the blobs are densely packed into a one-dimensional array. The number of blobs $\#_\mathrm{B}$ is given by $\#_\mathrm{B} = N/n_\mathrm{B}$ and $R_\parallel$ is therefore given

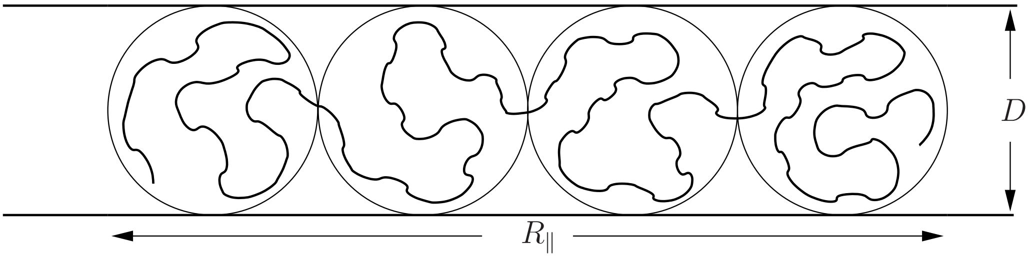

Figure 2.1: A polymer chain trapped in a tube. The chain behaves like a string of blobs. Within the length scale of a blob the chain is almost unperturbed and behaves like a free one.

by

$$R_\parallel = \#_\mathrm{B} D = \frac{N}{n_\mathrm{B}} D \simeq Nb \left(\frac{b}{D}\right)^{2/3}, \tag{2.27}$$

in agreement with Eq.(2.24).

Having calculated $R_\parallel$, the confinement energy F_conf can now be estimated. This is the energy required to squeeze the chain in the tube. It measures the loss of entropy of the chain and must therefore be proportional to T. On the other hand the confinement energy must be proportional to the number of blobs and therefore proportional to N. Likewise $R_\parallel$ it must have the scaling form

$$F_\mathrm{conf} \simeq k_\mathrm{B} T g_\mathrm{F} \left(\frac{R_\mathrm{e}}{D}\right), \tag{2.28}$$

where $g_\mathrm{F}(x) \to x^l$ for $x \to \infty$. Since F_conf is proportional N, R_e^l must be proportional to N and therefore $l = 5/3$. The confinement energy is then given by

$$F_\mathrm{conf} \simeq k_\mathrm{B} T N \left(\frac{b}{D}\right)^{5/3} = k_\mathrm{B} T \#_\mathrm{B}, \tag{2.29}$$

or for general exponent ν

$$F_\mathrm{conf} \simeq k_\mathrm{B} T N \left(\frac{b}{D}\right)^{1/\nu}. \tag{2.30}$$

The result in Eq.(2.29) can also be explained by a physical argument. The confinement blobs are all independent of each other and therefore each blob accounts for a confinement energy of the order of the inherent energy scale $k_\mathrm{B}T$. The total confinement energy is thus given by the number of blobs $\#_\mathrm{B}$ times $k_\mathrm{B}T$.

This analysis can be generalised to chains confined to other geometries, such as wedges or cones. In all these cases the confinement energy scales linearly with the number of confinement blobs. The calculation of the confinement energy in Chapter 3 is similar to the calculation of the confinement energy of a polymer chain inside a truncated cone. The latter one is therefore presented below.

Fig.(2.2) shows a polymer chain confined to the inside of a truncated cone. The blob size $\zeta(r)$ is given by

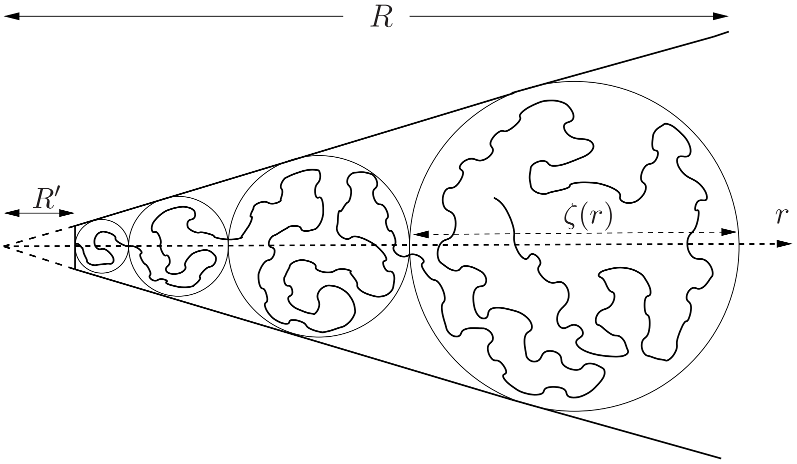

Figure 2.2: A polymer chain inside a truncated cone. The chain is grafted to the truncated tip of the cone at position R_{trunc} from the inside. The blob size ζ is an increasing function of the distance r from the tip.

$$\zeta(r) = 2\sin(\alpha)r, \tag{2.31}$$

where 2α is the cone angle. For the confinement energy of the chain the number of blobs $\#_{\mathrm{B}}$ has to be calculated. It is given by the following integral

$$\#_{\mathrm{B}} = \int_{R_{\mathrm{trunc}}}^{R} \frac{1}{\zeta r}\mathrm{d}r = \frac{1}{2\sin(\alpha)}\ln\left(\frac{R}{R_{\mathrm{trunc}}}\right). \tag{2.32}$$

The number of monomers per blob is given by

$$n_{\mathrm{B}} \simeq \left(\frac{\zeta(r)}{b}\right)^{1/\nu} = \left(\frac{2\sin(\alpha)r}{b}\right)^{1/\nu}, \tag{2.33}$$

compare Eq.(2.26). Knowing n_{B} it is possible to calculate R.

$$\begin{aligned} N &= \int_{R_{\mathrm{trunc}}}^{R} \frac{n_{\mathrm{B}}}{\zeta(r)}\mathrm{d}r \approx \int_{0}^{R} \frac{n_{\mathrm{B}}}{\zeta(r)}\mathrm{d}r = \left(2\sin(\alpha)\right)^{1/\nu-1}\left(\frac{R}{b}\right)^{1/\nu} \\ \Rightarrow R &= \left(2\sin(\alpha)\right)^{\nu-1} N^{\nu} b, \end{aligned} \tag{2.34}$$

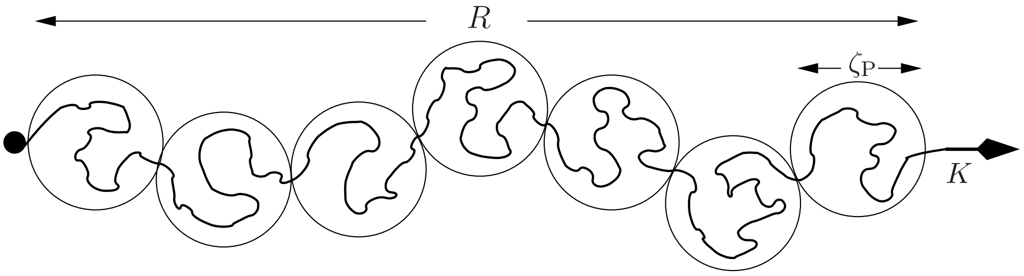

Figure 2.3: A polymer chain under tension. The force K is applied to one end of the chain, the other end is held fix. The chain breaks up into a series of blobs. The blob size ζ_P is set by the force.

where $R_{\text{trunc}} \ll R$ has been used. The confinement energy can now be calculated

$$F_{\text{conf}} \simeq k_B T \#_B = k_B T \frac{1}{2\sin(\alpha)} \ln\left(\frac{(2\sin(\alpha))^{\nu-1} N^{\nu} b}{R_{\text{trunc}}}\right). \tag{2.35}$$

In Section 3.2 it will be shown that the confinement energy of a starlike corona formed by polymer chains has a similar structure, compare Eq.(3.7).

2.4. Real chain under tension

Scaling arguments and the blob picture can also be used to describe the behaviour of a real chain under tension. A force K is applied to the ends of polymer immersed in good solvent. There are then two characteristic length scales: $R_e \simeq bN^{\nu}$ and $\zeta_P = k_B T/K$ [26]. The extension R of the chain as a function of the force may be written as [41]

$$R(K) = R_e g_K\left(\frac{R_e}{\zeta_P}\right). \tag{2.36}$$

At very low force ($x < 1$) the extension R should be linear in x, hence $g_K(x \to 0) \simeq x$. This yields

$$R(K) \simeq \beta R_e^2 K, \quad \text{for } KR_e < k_B T. \tag{2.37}$$

The more interesting situation at larger force ($x \gg 1$) can be described as follows. The chain breaks up into a series of blobs each of size ζ_P as shown in Fig.(2.3). As in the case of the chain confined to a tube, the chain inside the blobs is almost unperturbed and behaves like a self-avoiding walk. At length scales larger than ζ_P

it behaves like a string of independent blobs. Similar to Eq.(2.26) the number of monomers inside each blob n_{P} is given by

$$\begin{aligned} \zeta_{\mathrm{P}} &\simeq n_{\mathrm{P}}^{\nu} b \\ \Leftrightarrow n_{\mathrm{P}} &\simeq \left(\frac{k_{\mathrm{B}}T}{bK}\right)^{\frac{1}{\nu}} . \end{aligned} \tag{2.38}$$

The chain extension R is given by the number of blobs $\#_{\mathrm{P}}$ times the blob size ζ_{P}.

$$R \simeq \#_{\mathrm{P}}\zeta_{\mathrm{P}} \simeq \frac{N}{n_{\mathrm{P}}}\zeta_{\mathrm{P}} \simeq Nb(\beta K b)^{\frac{1-\nu}{\nu}} \tag{2.39}$$

The corresponding elastic free energy can be estimated by $k_{\mathrm{B}}T$ per blob and is thus given by

$$\beta F_{\mathrm{stretch}} \simeq \#_{\mathrm{P}} \simeq N(\beta b K)^{\frac{1}{\nu}} \simeq N\left(\frac{R}{Nb}\right)^{\frac{1}{1-\nu}} = \left(\frac{R}{N^{\nu}b}\right)^{\frac{1}{1-\nu}} \simeq \left(\frac{R}{R_{\mathrm{e}}}\right)^{\frac{1}{1-\nu}} . \tag{2.40}$$

The total free energy of a chain at an applied force K reads

$$\beta F \simeq \left(\frac{R}{R_{\mathrm{e}}}\right)^{\frac{1}{1-\nu}} - \beta K R. \tag{2.41}$$

The arguments used to derive the force-extension relation and the elastic free energy hold not only in the case of good solvent ($\nu = 3/5$) but also in the case of Θ-solvent ($\nu = 1/2$). The linear force-extension relation of an ideal chain, compare Eq.(2.6), can thus be recovered.

For very large forces, the extension of the chain might come close to its contour length Nb. In this case the picture described above is no longer valid. Obviously, the maximal extension of the chain is given by its contour length. When approaching the contour length, the force diverges. The effect of this finite extensibility is briefly discussed at the end of Chapter 4.

3. Rod-coil copolymer in selective solvent

3.1. Introduction

As already mentioned in Chapter 1, the phase behaviour of rod-coil multiblock copolymers in selective solvent is a very rich field of study. In this chapter a single rod-coil multiblock copolymer immersed in selective solvent will be studied. It represents a model system for the formation of structural elements on the single molecule level. It will be shown in Section 3.5 that a single rod-coil multiblock copolymer might even serve as a very simple model to explain the specific structure of α-helix bundles in certain classes of proteins.

In several papers [27–37] the phase diagram for melts of rod-coil polymers is studied as an extension of the case of flexible copolymers under different architectures.

Significant work has been done for di- and triblock rod-coil copolymers using scaling arguments, see [29–32]. In Chapter 5 the adsorbtion at a surface of rod-coil diblocks in selective solvent will be discussed.

The behaviour of a single multiblock polymer containing stiff parts (rods) rods and flexible parts (coils) is less established, especially concerning the stability of certain micellar and brushlike structures, see e.g. [38, 39].

Rod-coil multiblock copolymers typically consist of stiff, rodlike blocks of a certain length L and diameter d which are connected by flexible chains containing N monomers each as pictured in Fig.(3.1). In this chapter the solvent is always assumed to be poor for the stiff parts of the copolymer such that they tend to aggregate. For the flexible parts the solvent is assumed to be either Θ-like or good, such

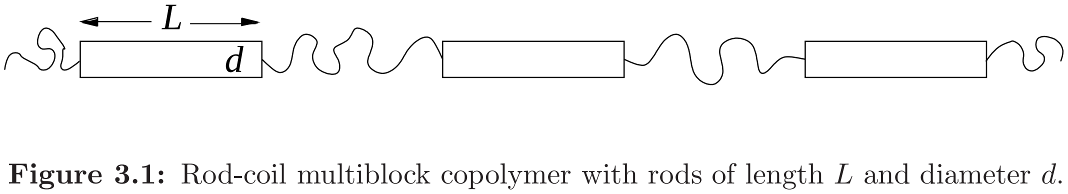

Figure 3.1: Rod-coil multiblock copolymer with rods of length L and diameter d.

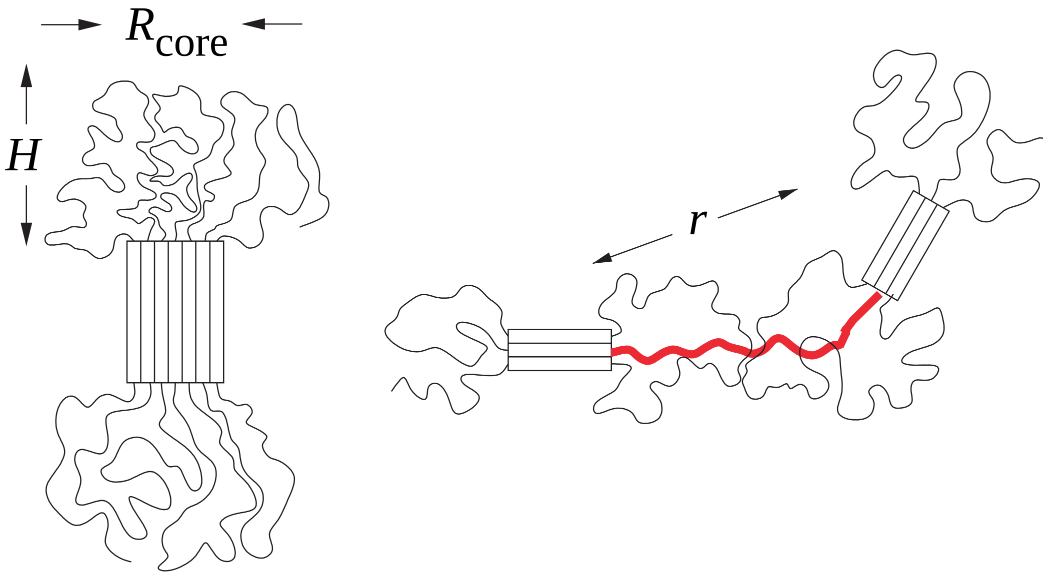

Figure 3.2: This figure shows two possible configurations: (a) One big micelle with a starlike corona is formed. (b) The system forms several connected micelles. The height of the corona is denoted by H, the radius of the micelle core by R_{core} and the distance between the cores by r. The stretching of the red chain results in additional loss of entropy.

that the monomers of the flexible parts repel each other. Under these assumptions the effective attraction of the rods drives the system into a compact structure. This compact structure imposes a confinement on the flexible chains and therefore lowers their entropy. It is this interplay between chain entropy and rod-rod attraction which determines the final equilibrium structure of the system. The precise form of the compact structure depends strongly on the molecular parameters such as interaction energies, but also on the entropic parameters like the number of monomers between two consecutive rods.

If the attractive forces between the rods are strong enough they typically form a cylindrical micelle surrounded by a corona of confined coils, see Fig.(3.2). The overall size of the micelle is naturally limited by the corona, which is itself determined by the length of the flexible parts and the solvent conditions. The stronger the confinement of the chains in the corona, the more they try to break up the aggregate of the rods in order to gain entropy. The size is also limited by the confinement close to the rod-flexible interface, where the chain segments close to the surface - created by the aggregating rods - suffer under grafting conditions as in a polymer brush. On the other hand, if the equilibrium number of rods f forming an individual submicelle is smaller than the total number of rods, the system might form several connected micelles, as depicted in Fig.(3.2b).

Of course there is also the possibility that the energy penalty of the corona becomes too large and micelle formation is not probable at all (i.e. $f \leq 1$). However, if the system actually forms micelles, there are two limiting cases for the shape of the corona:

(i) For very long connecting chains the height H of the corona may be much larger than the radius R_{core} of the micelle core formed by the rods. In this limit the corona almost resembles a star shaped object as shown in Fig.(3.2a). It is therefore referred to as the starlike limit.

(ii) For short enough connecting chains, H may be much smaller than R_{core}. In this limit the corona looks like a brush and it is therefore referred to as the brushlike limit.

In the next section the equilibrium aggregation number of rods in the starlike limit is calculated. In Section 3.3 multi-micelle configurations are discussed in the starlike limit. The equilibrium aggregation number of rods in the brushlike limit is calculated in Section 3.4 And finally in Section 3.5 the results of this theory are compared to experimental values for proteins.

3.2. Starlike Limit

In this section the spherical, starlike limit is discussed. This limit covers a much wider range of physical parameters than the brushlike limit. It is therefore discussed in greater detail. Furthermore, multi-micelle configurations will only be discussed for the starlike limit in Section 3.3.

The free energy of the system consists of the following terms

$$F = F^{\text{rods}}_{\text{surface}} + F^{\text{rods}}_{\text{entropy}} + F^{\text{coils}}_{\text{conf}} + F^{\text{coils}}_{\text{connect}}. \tag{3.1}$$

The first term in Eq.(3.1) is the energy penalty associated with the surface of the micelle core that is exposed to the solvent. The entropic contribution of the rods is taken into account by the second term. $F^{\text{coils}}_{\text{conf}}$ specifies the free energy cost due to the confinement of the coils in the corona and the last term takes into account that the end-to-end distance of each coil connecting two rods is limited to the radius of the micelle core. In the following, the individual contributions are introduced and calculated term by term.

The surface free energy $F^{\text{rods}}_{\text{surface}}$ of the rods is given by

$$\beta F^{\text{rods}}_{\text{surface}} \simeq \beta\gamma d^2 \left(f + f^{1/2} L/d\right). \tag{3.2}$$

This contribution to the free energy has its origin in the surface exposed to the solvent that is created by the aggregation of the rods. γ is the surface tension of the rods and is of the order of $\gamma \sim \mathcal{O}(k_\mathrm{B}T/d^2)$. The exact value depends on how poor the solvent is for the rods. The term $\sim d^2 f$ represents the free energy contribution of the surface of all caps of the rods. It is proportional to the number of rods in the micelle and therefore does not contribute to the equilibrium micelle size. The term $\sim d^2\, f^{1/2} L/d$ represents the contribution of the hull of the micelle. It is this term which favours the formation of micelles, compare e.g. [30].

The entropy of the rods is simply given by the exchange possibilities of the rods in the micelle, hence it is of the usual combinatoric form $\beta F^\mathrm{rods}_\mathrm{entropy} = -f \ln f$ which has its origin in the number of $f!$ exchange possibilities of f rods.

To calculate the confinement energy $F^\mathrm{coils}_\mathrm{conf}$, a specific model to describe the corona is needed. In the starlike limit the height H of the corona is much larger than the core radius R_core. Thus the corona is essentially spherical, that is starlike. The Daoud-Cotton model [40] used here has become the standard model to describe the confinement of the polymer chains for such starlike structures.

To estimate the confinement energy in this model the notion of confinement blobs is used, as introduced in Chapter 2. Inside one of these blobs the chain behaves like a free unconfined chain. The blobs are densely packed and each blob accounts for a confinement energy of the order $\mathcal{O}(k_\mathrm{B}T)$. Hence the blob sets a length scale in the system.

The coils are confined to f virtual truncated cones beginning at the end of each rod. The wall of the cones sets the blob size ζ as a function of the distance r from the micelle core, compare Fig.(3.3) and Section 2.3. To derive this function a spherical shell of the corona of radius r and thickness $\zeta(r)$ is considered. This shell contains f blobs. Its volume is approximatively given by $r^2\zeta(r)$. On the other hand its volume is also given by the volume of a single blob times the number of blobs $\zeta^3(r)f$. Hence

$$r^2\zeta(r) \simeq \zeta^3(r) f \;\rightarrow\; \zeta(r) \simeq r/f^{1/2}. \tag{3.3}$$

To actually calculate the confinement free energy in units of $\mathrm{k_B}T$ one now simply has to count the total number of confinement blobs in the corona.

$$\beta F^\mathrm{coils}_\mathrm{conf} \simeq \int_{R_\mathrm{core}}^{R_\mathrm{core}+H} r^2 \zeta^{-3}(r)\,\mathrm{d}r = f^{3/2} \ln\left(\frac{R_\mathrm{core}+H}{R_\mathrm{core}}\right). \tag{3.4}$$

In the starlike limit considered here the height of the corona H is much larger than the radius of the micelle core $R_\mathrm{core} \simeq f^{1/2} d$, therefore R_core can be neglected in the numerator of Eq.(3.4).

The height of the corona H is calculated in a similar way. One sums up all blobs until running out of monomers. To do so a quantity $n_\mathrm{B}(r)$ is introduced that denotes the number of monomers inside one blob at distance r from the core. Since the chain behaves like a free chain within the length scale of the blob, $\zeta(r)$ is given in terms

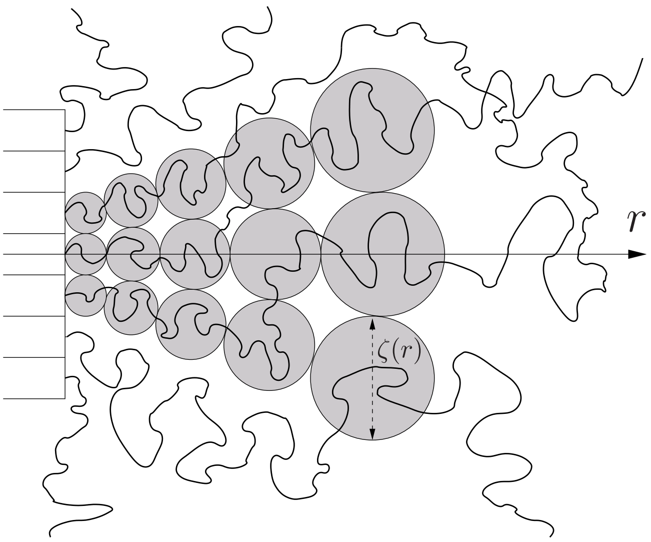

Figure 3.3: This figure shows the blob representation of the model for the corona in the starlike case. The blobs are shaded in grey for better visibility. The blob size $\zeta(r)$ increases from the micelle core to the outside.

of n_B and the monomer size b by $\zeta(r) \simeq n_\mathrm{B}^\nu(r) b$. The exponent ν is kept general to allow for either Θ-solvent ($\nu = 1/2$) or good solvent ($\nu = 3/5$). Now the height of the corona H can be calculated in the following way

$$N \simeq \int_{R_\mathrm{core}}^{R_\mathrm{core}+H} \frac{n_\mathrm{B}(r)}{\zeta(r)} \,\mathrm{d}r \simeq \int_0^H \frac{n_\mathrm{B}(r)}{\zeta(r)} \,\mathrm{d}r \simeq f^{\frac{\nu-1}{2\nu}} \left(\frac{H}{b}\right)^{1/\nu}. \tag{3.5}$$

In the above calculation $H \gg R_\mathrm{core}$ has been used. This result immediately yields

$$H \simeq f^{\frac{1-\nu}{2}} N^\nu b. \tag{3.6}$$

The contribution $F_\mathrm{conf}^\mathrm{coils}$ is now fully determined. It is given by

$$F_\mathrm{conf}^\mathrm{coils} \simeq f^{3/2} \ln\left(\frac{bN^\nu}{df^{\nu/2}}\right). \tag{3.7}$$

The last contribution to the free energy that has to be calculated is $F_\mathrm{connect}^\mathrm{coils}$. It is the one that tells the free energy that the entire polymer is connected and has its origin in the partition function of the chains in the corona. To estimate this term one first has to notice that the end-to-end distance R of the connecting coils is limited to the discrete values $R = nd$, where $n = 1, ..., f^{1/2}$. The partition function of each chain is therefore given by the sum of the probabilities of the end-to-end distances over all possible discrete end-to-end distances. The case of Θ-solvent is discussed first.

For Θ-solvent the contribution to the free energy is given by

$$\beta F^{\text{coils}}_{\text{connect}} \simeq -f \ln \left(\sum_{R^2=d^2}^{fd^2} \mathcal{N}(N) \exp\left\{ -\frac{3R^2}{2b^2N} \right\} \right) , \tag{3.8}$$

where the normalisation factor $\mathcal{N}(N)$ contains a within this scaling approach irrelevant N-dependence, which does not contribute to the free energy in a significant way. Since the sum in Eq.(3.8) corresponds to a simple geometric series it can be performed and - omitting all numerical prefactors - one obtains

$$\begin{aligned} \beta F^{\text{coils}}_{\text{connect}} &\simeq -f \left(\ln \left[\frac{1-\exp\{-fd^2/b^2N)\}}{1-\exp\{-d^2/(b^2N)\}} \right] - \frac{d^2}{b^2N} \right) \\ &\simeq -f \ln f + \frac{f^2\, d^2}{b^2N} . \end{aligned} \tag{3.9}$$

The second line in the above equation is a next to leading order approximation. This result is physically remarkable and deserves some explanation. The first term in Eq.(3.9) reflects the f discrete possibilities for the end-to-end distance and therefore - as an entropy term - lowers the free energy. It is identical to the term for the entropy of the rods $F^{\text{rods}}_{\text{entropy}}$. This is not surprising, since exchanging two chain end points is equivalent to exchanging two rods within the micelle due to the connectivity of the entire system. The second term in Eq.(3.9) reflects the energy penalty associated with the stretching of the connecting chains.

In the case of good solvent conditions the situation concerning this contribution is slightly subtle, since there is no closed form for the probability distribution of the end-to-end distance $P_R(R, N)$. Fortunately there are limiting expressions. The best known one is the limit of long end-to-end distances $R > R_{\text{e}}$, where R_{e} denotes the root mean square end-to-end distance (see Section 2.2). It is given by the des Cloizeaux form $P_R(R, N) \sim e^{-\frac{3}{2}(R/Re)^{5/2}}$, see e.g. [42, 43]. However, in the starlike limit the height of the corona H is much larger than the radius of the micelle core R_{core}. To ensure that this is the case the contour length of the chains Nb must be sufficiently large. This implies that the root mean square end-to-end distance of one free chain in Θ-solvent R_{e} is larger than the radius of the micelle core $R_{\text{core}} = fd^{1/2}$. Hence, the largest possible end-to-end distance of the chains confined in the corona is smaller than the root mean square end-to-end distance of a free chain. On the other hand the inequality $d \gg b$ surely holds which means that the smallest possible end-to-end distance is much larger than the segment length. For these intermediate end-to-end distances it has been shown by Edwards and Singh [42], that a quasi Gaussian regime in the distribution function exists. Within the range given above the end-to-end distance distribution for a polymer in good solvent scales like $P_R(R, N) \sim e^{-\frac{3}{2}(R/Re)^2}$ see [42], rather than the well known des

Cloizeaux form $\sim e^{-\frac{3}{2}(R/Re)^{5/2}}$. Thus $F^{\text{coils}}_{\text{connect}}$ for good solvent can be formulated in a similar way as in the Θ-solvent case.

$$\begin{aligned}
\beta F^{\text{coils}}_{\text{connect}} &\simeq -f \ln \left(\sum_{R^2=d^2}^{fd^2} \mathcal{N}(N) \exp\left\{ -\frac{3R^2}{2b^2 N^{6/5}} \right\} \right) \\
&\simeq -f \left(\ln \left[\frac{1-\exp\left\{-fd^2/b^2N^{6/5})\right\}}{1-\exp\left\{-d^2/(b^2N^{6/5})\right\}} \right] - \frac{d^2}{b^2 N^{6/5}} \right) \\
&\simeq -f \ln f + \frac{f^2\, d^2}{b^2 N^{6/5}}. \qquad (3.10)
\end{aligned}$$

The two results - Eqs.(3.9,3.10) - can be summarised in a general form using the exponent ν.

$$\beta F^{\text{coils}}_{\text{connect}} \simeq -f \ln f + \frac{f^2\, d^2}{b^2 N^{2\nu}} \qquad (3.11)$$

Collecting all essential terms - and omitting those which are linear in f and all numerical prefactors - the free energy of the system is given by

$$\beta F(f) \simeq \beta f^{1/2} \gamma d^2 \frac{L}{d} + f^{3/2} \ln \left(\frac{bN^\nu}{d f^{\nu/2}} \right) - f \ln f + f^2 \frac{d^2}{b^2 N^{2\nu}}. \qquad (3.12)$$

The equilibrium structure corresponds to the minimum of the free energy per rod-coil subunit F/f; i.e., $\partial(F/f)/\partial f = 0$.

The dominating contributions to the free energy are $F^{\text{rods}}_{\text{surface}}$ and $F^{\text{coils}}_{\text{conf}}$. The other two contributions $F^{\text{rods}}_{\text{entropy}}$ and $F^{\text{coils}}_{\text{connect}}$ are much smaller and can be treated as corrections. First $F^{\text{rods}}_{\text{entropy}}$ and $F^{\text{coils}}_{\text{connect}}$ are neglected. The free energy per rod-coil subunit then reads

$$\frac{\beta F_0(f_0)}{f_0} \simeq \beta f_0^{-1/2} \gamma d^2 \frac{L}{d} + f_0^{1/2} \ln \left(\frac{bN^\nu}{d f_0^{\nu/2}} \right). \qquad (3.13)$$

Minimising the above equation and afterwards approximating the logarithmic terms as constant yields the following result for the equilibrium aggregation number of rods

$$f_0 \simeq \beta \gamma d^2 \frac{L}{d}. \qquad (3.14)$$

The same result has been obtained by Halperin for a system of unconnected triblock rod-coil copolymers immersed in selective solvent [25]. If also $F^{\text{rods}}_{\text{entropy}}$ and $F^{\text{coils}}_{\text{connect}}$

are taken into account, a correction term to f_0 can be expected, i.e. $f \approx f_0 + \Delta f$. In the following Δf will be determined to linear order.

Minimising the full Eq.(3.12) and approximating the logarithmic terms as constant yields

$$\begin{aligned} 0 &= -\left(f_0+\Delta f\right)^{1/2} + \left(f_0+\Delta f\right)^{3/2} \frac{d^2}{b^2 N^{2\nu}} + \Delta f \\ &\simeq -f_0^{1/2}\left(1+f_0^{-1}\Delta f\right) + f_0^{3/2}\left(1+f_0^{-1}\Delta f\right)\frac{d^2}{b^2N^{2\nu}} + \Delta f \\ \Leftrightarrow \Delta f &= \frac{f_0^{1/2} - f_0^{3/2} d^2/(b^2N^{2\nu})}{1 - f_0^{-1/2} + f_0^{1/2} d^2/(b^2N^{2\nu})} \\ &\simeq f_0^{1/2} - f_0^{3/2}\frac{d^2}{b^2N^{2\nu}}. \end{aligned} \tag{3.15}$$

In the last step $f_0^{-1/2} + f_0^{1/2} d^2/(b^2N^{2\nu}) < 1$ was used, which always holds in the starlike limit. Inserting Eq.(3.14) in Eq.(3.15) yields the following more accurate result for the equilibrium aggregation number of rods f

$$f \simeq \beta\,\gamma d^2 \frac{L}{d} + \left(\beta\,\gamma d^2\frac{L}{d}\right)^{1/2} - \left(\beta\,\gamma d^2 \frac{L}{d}\right)^{3/2}\frac{d^2}{b^2N^{2\nu}}. \tag{3.16}$$

The result shows that, apart from the rod-solvent surface tension γ, mainly the aspect ratio of the rods L/d and the effective grafting ratio $d^2/(b^2N^{2\nu})$ determines the number of aggregating rods. The first correction term due to the exchange entropy is positive. This is in agreement with the physical intuition, since the formation of a larger micelle increases the number of exchange possibilities for the rods together with the number of possible end-to-end distances for the coils. Such a trend of extending the micelle is counterbalanced by the growing size of the micelle itself because some of the connecting coils become more and more stretched depending on the ratio $d^2/(b^2N^{2\nu})$. Therefore the second correction due to the second term of $F^{\text{coils}}_{\text{connect}}$ (Eq.(3.11)) is negative and reduces f. This last term in Eq.(3.16) becomes less relevant for larger N, since the stretching of the connecting flexible part becomes less important.

3.3. Multimicellar structures in the starlike limit

The equilibrium result for the number of rods forming a micelle f might be smaller than the actual number of rods in the copolymer. If this is the case the copolymer forms several connected micelles. To obtain the equilibrium structure the interaction between micelles has to be considered. There are two contributions to the interaction energy. One is due to the repulsion of the coronas and one is due to the stretching of the connecting chain, see Fig.3.2b. The possibility of the formation of two micelles which are connected by a stretched chain will be estimated within the scaling limit.

Let r be the distance between the micelle cores. The stretching energy - compare Section 2.4 - is then given by

$$\beta F_{\mathrm{stretch}} \sim (r/(bN^{\nu}))^{1/(1-\nu)}. \tag{3.17}$$

Here the des Cloizeaux form (see e.g. [42, 43]) for the distribution of the end-to-end distance $P_{\mathrm{R}}(R, N)$ is used. The distance between the two micelle cores should be comparable to the height of the corona due to the repulsion of the coronas. Therefore the end-to-end distance of the connecting coil R can assumed to be larger than the root mean square value R_{e} for the same coil in isolated conditions. Thus the des Cloizeaux form has to be used.

The repulsive potential $U(r)$ between two coronas can be approximated well by scaling considerations similar to the ones used by Witten and Pincus for two star polymers, compare [44]. For distances larger than twice the height of the corona ($2H$) the coronas can be assumed not to interact at all since they barely touch each other, i.e. $U(r \geq 2H) = 0$. For distances comparable to the radius of the micelle core R_{core} the bulk of the system is similar to a single corona with $2f$ coils. Hence the increase in confinement free energy, which constitutes the interaction energy, is of the same order of magnitude as the confinement energy itself,

$$U(R_{\mathrm{core}}) = \Delta F^{\mathrm{coils}}_{\mathrm{conf}} \approx F^{\mathrm{coils}}_{\mathrm{conf}}. \tag{3.18}$$

The probability distribution of two micelles being a distance r apart is given by

$$P(r)/P(2H) = \exp[-\beta U(r)], \tag{3.19}$$

where $P(2H)$ is the probability for vanishing interaction potential. Assuming $P(r)$ has the scaling form $P(r) = P(2H)g(r/2H)$ and matching it with the two limiting cases discussed above immediately leads to the following expression for the interaction potential

$$\beta U(r) \approx \begin{cases} f^{3/2}\ln(2H/r) & \text{for } r < 2H \\ 0 & \text{for } r \geq 2H \end{cases} \tag{3.20}$$

which holds similarly for Θ- and good solvent.

Minimisation of $U(r) + F_{\mathrm{stretch}}(r)$ with respect to r gives the equilibrium distance of the two micelles. It turns out that the equilibrium distance is $r \approx 2H \simeq f^{(1-\nu/2)}N^{\nu}b$ at which the coronas just touch each other, i.e., $U(f, 2H) = 0$. Thus the total interaction energy is - within the limits of the scaling approach - given by

$$\beta F_{\mathrm{stretch}}(2H) \sim f^{1/2}. \tag{3.21}$$

It scales with f like the relevant part of the surface contribution to the free energy (second term in Eq.(3.2)) does. Therefore including this contribution in the total free energy, Eq.(3.12), simply yields a shift in the surface term,

$$\beta\,\gamma d^2\, L/d \rightarrow \beta\,\gamma d^2\, L/d + 1. \tag{3.22}$$

This shift does not change the general scaling behaviour of the equilibrium micelle size and is therefore neglected in the following considerations.

To test whether a multi micelle configuration is actually stable, the total free energy of a system with fixed number of rod-coil subunits M forming several micelles is considered. Let n be the number of micelles formed by the system. For simplicity, all micelles are assumed to be of the same size. Hence the number of rods forming each micelle is given by M/n. The total free energy can be expressed similar to Eq.(3.12) as

$$\begin{aligned} \beta F(M,n) \;\simeq\; & n \left[\beta \left(\frac{M}{n}\right)^{1/2} \gamma d^2 \frac{L}{d} + \left(\frac{M}{n}\right)^{3/2} \ln\left(\frac{bN^\nu}{d\,(M/n)^{\nu/2}}\right) \right. \\ & - \left. (M/n)\ln(M/n) + \left(\frac{M}{n}\right)^2 \frac{d^2}{b^2 N^{2\nu}} + F_{\text{int}}^{\text{micelles}} \right], \end{aligned} \tag{3.23}$$

where the last term in the square brackets represents the interaction energy of two micelles discussed above. As shown above, it only produces a shift in the surface terms and can be neglected.

To demonstrate the dependence of the free energy of the total system on the number of micelles, Eq.(3.23) is plotted in Fig.3.4. The plot shows that for a given system, one big stable micelle (upper curve) can split into several micelles (lower curve) when the surface tension γ is reduced. Thus for a big enough system size a multi micelle configuration can be indeed stable. Fig.(3.4) also shows that for the case of $n > 1$ the shape of the free energy around the minimum becomes rather flat. This implies that fluctuations become more important and exchange of rods between micelles could be possible.

After having shown that multi micelle configurations can be stable, it would be interesting to calculate an estimate for the number of micelles formed by the system in equilibrium. This can be done by means of Eq.(3.23). The number of identical micelles n for a given system size M is given by the equilibrium condition $\partial F(M,n)/\partial n = 0$. As was done when calculating the equilibrium number of aggregating rods f, the contributions $F_{\text{entropy}}^{\text{rods}}$ and $F_{\text{connect}}^{\text{coils}}$ (the third and fourth term in

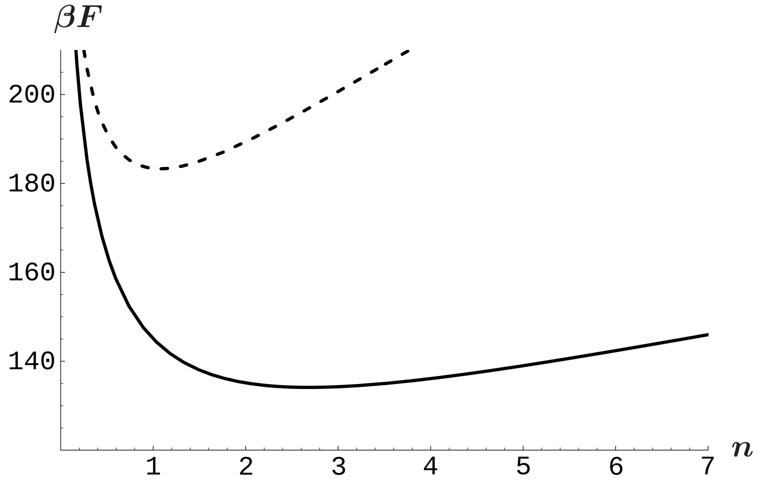

Figure 3.4: This plot shows the dependence of the free energy in units of $k_B T$ on the number of micelles n. The total number of rod-coil units is chosen to be $M = 30$ and the term containing the chain information $bN^\nu/d = 10$. For the upper dashed curve the surface term $\beta\,\gamma d^2\, L/d$ is chosen to be 12 and 5 for the lower curve.

Eq.(3.23)) are neglected in a first approximation.

$$\beta F_0(M, n_0) \simeq n_0 \left[\beta \left(\frac{M}{n_0}\right)^{1/2} \gamma d^2 \frac{L}{d} + \left(\frac{M}{n_0}\right)^{3/2}\right]. \tag{3.24}$$

Minimising the above equation with respect to n_0 yields

$$n_0 \simeq M \left(\beta\ \gamma d^2 \frac{L}{d}\right)^{-1}. \tag{3.25}$$

This result is consistent with the result for the equilibrium number of micelles in the same approximation f_0, compare Eq.(3.14). It is given by $f_0 = M/n_0$.

To proceed, the number of micelles n is approximated by $n \approx n_0 + \Delta n$. The calculation of n to linear order in Δn follows the same scheme as above - see Eq.(3.15) - and is omitted here.

$$n \simeq M \left[\left(\beta\ \gamma d^2 \frac{L}{d}\right)^{-1} + \left(\beta\ \gamma d^2 \frac{L}{d}\right)^{-1/2} \frac{d^2}{b^2 N^{2\nu}} - \left(\beta\ \gamma d^2 \frac{L}{d}\right)^{-3/2}\right]. \tag{3.26}$$

As a consistency check $f = M/n$ is recalculated to linear order using the above result for n.

$$\begin{aligned} f &= M\,(n_0 + \Delta n)^{-1} \simeq \frac{M}{n_0}\left(1 - \frac{\Delta n}{n_0}\right) \\ &= \beta\ \gamma d^2 \frac{L}{d} + \left(\beta\ \gamma d^2 \frac{L}{d}\right)^{1/2} - \left(\beta\ \gamma d^2 \frac{L}{d}\right)^{3/2} \frac{d^2}{b^2 N^{2\nu}}. \end{aligned} \tag{3.27}$$

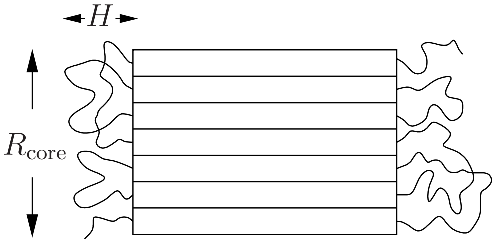

Figure 3.5: This figure shows micelles with brushlike coronas: A micelle is described by H, which denotes the height of the corona and R_{core} which is the radius of the micelle core.

This is indeed the same result for the equilibrium aggregation number of rods as in Eq.(3.16). Hence the results for both n and f are consistent.

3.4. Brushlike limit

Now the limiting case in which the height of the corona H is much smaller than the core radius R_{core} is considered. Thus the corona is assumed to be brushlike as depicted in Fig.(3.5).

The confinement energy for a polymer brush scales linearly with the area to which the brush is grafted (neglecting all edge effects) [45]. For the problem considered here this means $F^{\mathrm{coils}}_{\mathrm{conf}}$ is proportional to f. Hence the confinement energy is extensive in f and therefore does not influence the equilibrium micelle size. For a system of unconnected coil-rod-coil copolymers this would mean that the rods either do not aggregate at all or form arbitrary large lamellar structures [30]. Since the system under consideration consists of one long multiblock copolymer, $F^{\mathrm{coils}}_{\mathrm{connect}}$ limits the equilibrium size of the micelles. In contrast to the starlike corona case this term is not a rather small correction but the only contribution to the free energy that limits the aggregation number of the rods.

For Θ-solvent $F^{\mathrm{coils}}_{\mathrm{connect}}$ is the same as in the starlike corona limit. In the good solvent regime the Gaussian approximation for the end-to-end distance distribution used above is only valid for end-to-end distances which are certainly less than R_{core}. Nevertheless, these short distances give the highest weights to the sum in the first line of Eq.(3.10). Hence using the quasi Gaussian approximation for the entire range of end-to-end distances up to R_{core} should be valid within this scaling picture. Therefore we may use Eq.(3.11) for both solvent regimes.

As already mentioned above, the confinement energy does not influence the equilibrium micelle size and can therefore be neglected in the free energy. It only gives an additive constant to to the free energy per rod-coil subunit. The free energy of one micelle in the brushlike limit is therefore given by

$$\frac{\beta F(f)}{f} \simeq \beta f^{-1/2}\gamma d^2 \frac{L}{d} - \ln f + f\frac{d^2}{b^2 N^{2\nu}}. \tag{3.28}$$

Minimisation with respect to f yields the following equation

$$f^{3/2}\frac{d^2}{b^2 N^{2\nu}} - f^{1/2} - \beta\gamma d^2 \frac{L}{d} = 0. \tag{3.29}$$

The above equation has one real solution for f which is rather long and not very instructive. However, under the condition $\beta\gamma d^2 L/d \gtrsim bN^\nu/d$ the solution for f can be well approximated by

$$f \sim \frac{b^2 N^{2\nu}}{d^2} + \left(\beta\gamma d^2 \frac{L}{d}\,\frac{b^2 N^{2\nu}}{d^2}\right)^{2/3}. \tag{3.30}$$

For parameters which violate the above assumption no short approximation for f can be found.

The scaling behaviour of f is very different from the one in the starlike limit, compare Eq.(3.16). Since now only $F^{\mathrm{coils}}_{\mathrm{connect}}$ limits the equilibrium micelle size, f is a function of the ratio of $R_{\mathrm{e}} \sim bN^\nu$ and the rod diameter d reflecting the stretching of the connecting coils. On the other hand the aggregation number f of course increases with increasing surface energy $\beta\ \gamma d^2\ L/d$ - second term in Eq.(3.30) - as it does in the starlike limit.

3.5. Comparison with proteins

In the introduction it was mentioned that a rod-coil multiblock copolymer can serve as a simple model system to describe certain classes of proteins containing α-helix bundles. The helices are very rigid and can be approximated safely as stiff rods with a finite diameter, which are connected by flexible (unstructured) chain parts. The bundles formed of several helices might be modelled by a cylindrical micelle of these stiff rods. To match the system discussed in this chapter only classes of proteins with no other secondary structure element rather than α-helices can be considered. In addition the α-helices in these proteins have to align in bundles. Other tertiary structure motifs due to very specific interactions cannot be described by this simple model.

In order to compare with proteins, typical standard values (see for instance [2]) have to be used for some of the parameters in the equations for the equilibrium micelle size - Eqs.(3.16, 3.30). The ratio of α-helix diameter to amino acid size is known to be $d/b \sim$ 2-3. For the surface energy of the rods (in units of $k_B T$) $\beta\gamma d^2 \sim 1$ is used.

In the following the bundle sizes of proteins with six different folds are compared with the predictions for f. Depending on the length of the chains connecting the helices, either the result for the starlike limit (Eq.(3.16)) or the one for the brushlike limit (Eq.(3.30)) has to be used. The solvent is assumed to be Θ-like, i.e. $\nu = 1/2$. The secondary structure files are taken from the Protein Data Bank (PDB) [56]. As a classification scheme the SCOP database [57] is used. All six folds are from the basic class 'all alpha proteins'. For these proteins neither the helices nor the connecting chains in one protein are all of the same length. To be able to compare the proteins with the simple rod-coil copolymer model, an estimate for L and N has to be made. For each protein, the rod length L is estimated by calculating the average number of amino acids per helix N_{H} multiplied by the pitch of an α-helix. In units of d this yields

$$\frac{L}{d} \approx \frac{N_{\mathrm{H}}}{4}. \tag{3.31}$$

N is estimated by calculating the average number of amino acids in the connecting chains between the helices.

Knowing how to estimate all parameters used in Eqs.(3.16, 3.30), the predictions for the size of the helix bundles f can now be calculated. The following proteins were analysed:

- Acyl-CoA Binding Protein, PDB identifier: 1aca, brushlike limit
- Apolipoprotein, 1lpe, brushlike limit
- Acyl Carrier Protein, 1acp, brushlike limit
- Apolipophorin III, 1aep, brushlike limit
- Phospholipase A2, 1bp2, starlike limit
- Transcription Elongation Factor S-II, 1enw_A, starlike limit

The Table below summarises the results:

PDB identifier	# amino acids	helices (SCOP)	f
1aca	87	4-helix bundle	3-4
1lpe	144	4-helix bundle	4-5
1acp	77	4-helix bundle	3-4
1aep	161	5-helix bundle	5
1bp2	123	2 helices parallel, 3 irregular	2
1enw_A	114	3-helix bundle, 1 irregular	3

The agreement between the actual size of the helix bundles and the predicted values for f seems to be very good. Especially for the last two folds with additional unaligned helices, the correct number of aligned helices is predicted. However, the scaling results for f - Eqs.(3.16, 3.30) - are only correct up to prefactors. In addition, the number of amino acids and the bundle size are both comparatively small and therefore at the limit of the validity of the scaling theory. Hence the correct numerical agreement might just be coincidence. Nevertheless, the prediction of the right order of magnitude and the right trend - higher values of f for larger bundles - suggest that a rod-coil multiblock might indeed serve as a most simplistic model to study possible configurations of helix bundle proteins.

4. Force-extension behaviour of a rod-coil copolymer

4.1. Introduction and basic assumptions

In the previous chapter the equilibrium size of a micelle was calculated. Now a multiblock copolymer in selective solvent consisting of M rods and $M + 1$ flexible parts that forms one big micelle at equilibrium is considered. The rods are still all of the same length L and diameter d. The chains connecting the rods consist of N monomers each with monomer size b. The rod and chain parameters are assumed to be such that the starlike limit is applicable. It was shown that in this limit the system forms one stable micelle in equilibrium if the number of rods M satisfies (compare Eq.(3.16))

$$M \leq \beta\gamma d^2 \frac{L}{d} + \left(\beta\gamma d^2 \frac{L}{d}\right)^{1/2} - \left(\beta\gamma d^2 \frac{L}{d}\right)^{3/2} \frac{d^2}{b^2 N^{2\nu}}. \tag{4.1}$$

The stretching and unfolding behaviour of such a system under force will be discussed in this chapter. The aim is to calculate a force-extension curve.

A force K is applied at one end of the copolymer whilst the other end is held fixed, see Fig.(4.1). This picture could be for instance related to an atomic force

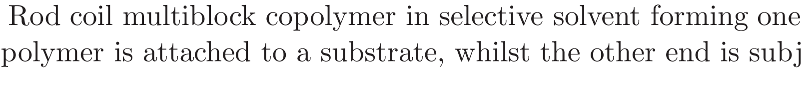

Figure 4.1: Rod coil multiblock copolymer in selective solvent forming one micelle. One end of the copolymer is attached to a substrate, whilst the other end is subject to a force K.

microscopy (AFM) experiment in which one end of the polymer is attached to a substrate and therefore held fixed and the other end is attached to the tip of an AFM-cantilever [17–21]. Another possibility to measure force-extension curves is to attach a small bead to the end of the polymer that is not fixed and hold this bead in an optical trap. The deflection of the trapped bead from the trap centre constitutes a measure of the force [21–24]. Generally, there are two possible scenarios. Either the displacement (i.e. the end-to-end distance of the polymer) is externally controlled and the force is measured - see [17, 22], or the force is imposed and the displacement is measured - see [24].

With increasing force one would first expect stretching of the two flexible end chains whilst the micelle stays undisturbed. At a certain force one of the outer rods from the micelle should start sliding off. When it slides off completely there will be a large drop in the force required to extend the polymer, since now there is a lot of length to gain from the detached rod and the chain connecting it to the micelle at very low force. If the force increases again, the chains become stretched again. Then the next rod will slide off and so on. Hence, if the force is measured at a given extension, the force extension curve should consist of several humps each of which corresponds to one rod being pulled out.

If the extension is measured at given force, the shape of the force-extension curve depends on the value of the force required to pull out each single rod. When there is a maximum force required to pull out the i-th rod, all other rods will be pulled out as well by this force. This results in a plateau in the force-extension curve. It is this scenario which will be considered in an example in Section 4.3, see Fig.(4.3).

For the above scenario to take place it might be necessary to impose a rather strong limitation on the possible structures of the micelle. The rods within the micelle have to be ordered in such a way that it is always possible to pull out rods from the outer shell of the micelle. If this would not be the case, pulling out a rod from within the micelle could result in breaking the micelle apart.

In the succeeding calculations the applied force is supposed to be given and the resulting extension will be calculated. The scaling considerations below are all based on a phenomenological free energy, see Eq.(4.3). This implies the assumption that the system is in equilibrium at each force given and therefore corresponds to a situation where the pulling is sufficiently slow to ensure equilibration of the system. This approach is named quasi static pulling. Using quasi static pulling it might actually be possible to release the constraint on the micelle structure mentioned above. During equilibration the micelle might reorganise after pulling out a rod from within the micelle. However, for this process to take place the micelle has to open up and hence has to expose most of the rod surfaces to the solvent, thereby creating a large surface energy. This constitutes a large energy barrier for the system. To decide whether the simple scaling picture presented below also holds for micelles

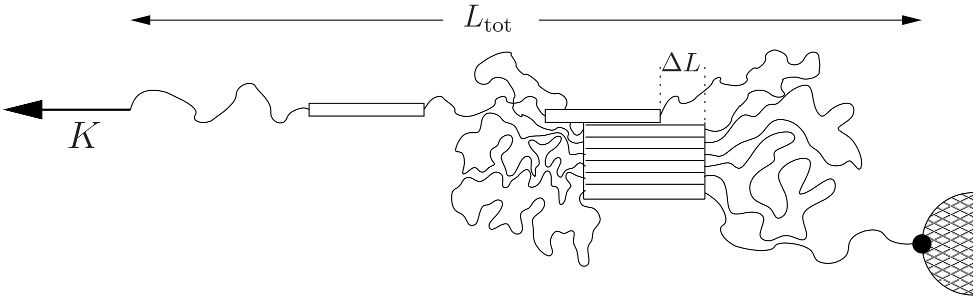

Figure 4.2: The system forms one defect rod and one rod is shifted by ΔL.

of randomly arranged rods, a dynamic description of the pulling process is needed, which cannot be provided by scaling consideration based on an equilibrium free energy. To be on the safe side it is better to stick to the assumption of an ordered micelle.

4.2. Equilibrium calculations

At a certain applied force the polymer is assumed to obtain the following equilibrium configuration. One big micelle containing $M - m$ rods, of which one is shifted by ΔL, is connected to m rods which are already pulled out completely. The total length of the polymer is denoted by L_{tot}, compare Fig.(4.2). The free energy of the polymer under an applied force K consists of the following contributions:

$$\begin{aligned} F(L_{\mathrm{tot}}, \Delta L, m) &= F_{\mathrm{micelle}}(M-m) + F_{\mathrm{defect}}(L_{\mathrm{tot}}, m) + F_{\mathrm{slide}}(\Delta L) \\ &- KL_{\mathrm{tot}}. \end{aligned} \tag{4.2}$$

$F_{\mathrm{micelle}}(M-m)$ is the free energy of the micelle formed by $M-m$ rods. For simplicity only the surface and confinement contributions are taken into account (1^{st} & 2^{nd} term in Eq.(4.3)). The contribution from the distribution of the end-to-end distance of the connecting rods, which - in the star like limit - is small compared to the other two contributions, is neglected. $F_{\mathrm{defect}}(L_{\mathrm{tot}}, m)$ is the free energy of the rods which are already pulled out completely and their connecting flexible chains. It is given by a surface contribution of the rods and a stretching contributions of the chains (3^{rd} & 4^{th} term in Eq.(4.3)). The free energy related to the shift of the rod in the micelle which is connected to the defect rods is named $F_{\mathrm{slide}}(\Delta L)$. It is also given by a surface and a stretching contribution (5^{th} & 6^{th} term in Eq.(4.3)). In explicit form the complete free energy reads

$$\begin{aligned}\beta F(L_{\mathrm{tot}}, \Delta L, m) &= \beta\gamma d L (M-m)^{1/2} + (M-m)^{3/2} \ln\left(\frac{bN^{\nu}}{d\,(M-m)^{\nu/2}}\right) \\ &+ \beta\gamma d L m + (m+2)\left(\frac{L_{\mathrm{tot}} - (m+1)L - \Delta L}{(m+2)bN^{\nu}}\right)^{\frac{1}{1-\nu}} \\ &+ \beta\gamma d \Delta L + \left(\frac{\Delta L}{bN^{\nu}}\right)^{\frac{1}{1-\nu}} - \beta K L_{\mathrm{tot}}. \end{aligned} \tag{4.3}$$

The 4th term in the above equation needs to be explained. There are $m+2$ chains which connect the defect rods to the micelle and the end points. In equilibrium they are all stretched to the same end-to-end distance. The total extension of all these chains is given by $L_{\mathrm{tot}} - (m+1)L - \Delta L$. Each chain has therefore the end-to-end distance $(L_{\mathrm{tot}} - (m+1)L - \Delta L)/(m+2)$. Its mean square end-to-end distance is given by bN^{ν}. With Eq.(2.40) from Section 2.4 it should now be obvious how this term is constructed.

At a given force K and a given number of defect rods m the free energy in Eq.(4.3) has to be minimised with respect to L_{tot} and ΔL in order to calculate the equilibrium extension as a function of K and m. Due to the stretching of the connecting chains there will be a critical value of the force at which it is preferable for the system to form another defect rod to release length. There are three possibilities how this could happen.

One possibility is that at a certain force the rod from the outer shell of the micelle which is connected to the defect rods starts to slide off and that the energy penalty due to stretching of the chains does not become large enough to favour the formation of a new defect rod before the rod is slid off completely. This happens at $\Delta L = L$, i.e. ΔL is limited to values between $0 \leq \Delta L < L$.

Another possibility is that the rod connecting the micelle to the defect rods slides off up to a shift $\Delta L < L$ at which it becomes energetically favourable to split from the micelle and form a new defect rod.

The third possibility is that the energy penalty due to stretching of the connecting chains is so large that it becomes energetically favourable to form another defect rod even before this rod starts to slide. It turns out below that the latter is actually the case for all sets of parameters and for good solvent as well as for Θ-solvent.

Minimisation of Eq.(4.3) with respect to L_{tot} gives

$$L_{\mathrm{tot}} = (m+2)bN^{\nu}\left[(1-\nu)bN^{\nu}\beta K\right]^{\frac{1-\nu}{\nu}} + (m+1)L + \Delta L. \tag{4.4}$$

The first term on the right hand side of Eq.(4.4) represents the length of the $m+2$

stretched chains connecting the defect rods, the micelle and the end points. The second term represents the length of the defect rods (mL) plus the length of the micelle core L. The last term is the shift of the outer rod of the micelle directly connected to the defect rods.

Minimisation of Eq.(4.3) with respect to ΔL gives

$$\beta\gamma d - \frac{1}{(1-\nu)bN^{\nu}}\left(\frac{L_{\text{tot}}-(m+1)L-\Delta L}{(m+2)bN^{\nu}}\right)^{\frac{\nu}{1-\nu}} + \frac{1}{(1-\nu)bN^{\nu}}\left(\frac{\Delta L}{bN^{\nu}}\right)^{\frac{\nu}{1-\nu}} = 0. \tag{4.5}$$

Inserting the result for L_{tot} from Eq.(4.4) into the above equation yields

$$\Delta L = bN^{\nu}\left[(1-\nu)bN^{\nu}(\beta K - \beta\gamma d)\right]^{\frac{1-\nu}{\nu}}. \tag{4.6}$$

The equation for ΔL shows that the force has to exceed a certain value, $K > \gamma d$, before the rod starts to slide off from the micelle. The surface tension per unit area of a rod exposed to the solvent is given by γ. Hence the associated energy penalty for an area $\Delta L d$ of the rod surface exposed the solvent is given by $\gamma d \Delta L$. Therefore the force K must exceed the line tension γd in order to create a finite shift ΔL.

Having calculated L_{tot} and ΔL for given K and m it is now possible to check which of the three scenarios described above is the correct one to describe the detachment of a new defect rod. It is first assumed that there is a force $K > \gamma d$ at which the rod starts to shift but does not detach. There is then a larger force K_{crit} at which the free energy $F(\Delta L, m)$ of the system with m defect rods and shift ΔL is equal to the free energy $F(\Delta L = 0, m+1)$ of the system with $m+1$ defect rods and zero shift. If $\Delta L(K_{\text{crit}}) < L$, the rod detaches before it is slid off completely. On the other hand, if $\Delta L(K_{\text{crit}}) > L$, the rod slides off completely before the force is large enough to rip it apart from the micelle. Consider $F(\Delta L, m) - F(\Delta L = 0, m+1)$:

$$\begin{aligned}\beta F(\Delta L, m) - \beta F(\Delta L = 0, m+1) &= \beta\gamma d L\left((M-m)^{1/2} - (M-m-1)^{1/2} - 1\right)\\ &+ (M-m)^{3/2} - (M-m-1)^{3/2}\\ &- \left[(1-\nu)bN^{\nu}\beta K\right]^{\frac{1}{\nu}} + \beta\gamma d\Delta L + \left(\frac{\Delta L}{bN^{\nu}}\right)^{\frac{1}{1-\nu}}\\ &+ \beta K\left\{bN^{\nu}\left[(1-\nu)bN^{\nu}\beta K\right]^{\frac{1-\nu}{\nu}} + L - \Delta L\right\}\end{aligned} \tag{4.7}$$

The second and third term in Eq.(4.7) are the confinement contributions of the chains in the micelle formed by $M-m$ rods and $M-m-1$ rods respectively.

The logarithmic factor (compare Eq.(4.3)) has been set to unity. The force K has to be larger than γd for a finite shift to appear. It can therefore be written as $K = \gamma d + \Delta K$. The last term in Eq.(4.7) can now be written as

$$\begin{aligned}\beta K \left\{ bN^\nu \left[(1-\nu) bN^\nu \beta K\right]^{\frac{1-\nu}{\nu}} + L - \Delta L \right\} &= \frac{1}{1-\nu}\left[(1-\nu)bN^\nu \beta K\right]^{\frac{1}{\nu}} \\ &+ \beta\gamma d L + \beta \Delta K L - \beta\gamma d \Delta L \\ &- \beta \Delta K \Delta L. \end{aligned} \tag{4.8}$$

Regrouping the terms in Eq.(4.7) yields

$$\begin{aligned}\beta F(\Delta L, m) - \beta F(\Delta L = 0, m+1) &= \beta\gamma d L \left((M-m)^{1/2} - (M-m-1)^{1/2}\right) \\ &+ (M-m)^{3/2} - (M-m-1)^{3/2} \\ &+ \frac{\nu}{1-\nu}\left[(1-\nu)bN^\nu\beta K\right]^{\frac{1}{\nu}} + \left(\frac{\Delta L}{bN^\nu}\right)^{\frac{1}{1-\nu}} \\ &+ \beta \Delta K (L - \Delta L) \\ &> 0 \quad \forall\, m, \Delta L. \end{aligned} \tag{4.9}$$

From Eq.(4.9) can be seen that $\beta F(\Delta L, m) > \beta F(\Delta L = 0, m+1)$ for constant force $K > \beta\gamma d$ and all m, ΔL and $\nu < 1$. This means that, with increasing force, it is energetically favourable to form a new defect rod even before a finite shift ΔL appears, i.e. the rods are ripped rather than slid off slowly. So in order to calculate the real critical force at which another defect rod is pulled out from the micelle, $F(\Delta L = 0, m) = F(\Delta L = 0, m+1)$ has to be considered.

$$\begin{aligned}\beta F(0, m) - \beta F(0, m+1) &= \beta\gamma d L \left((M-m)^{1/2} - (M-m-1)^{1/2} - 1\right) \\ &+ (M-m)^{3/2} - (M-m-1)^{3/2} \\ &- \left[(1-\nu)bN^\nu \beta K_{\text{crit}}\right]^{\frac{1}{\nu}} \\ &+ \beta K_{\text{crit}} \left\{ bN^\nu \left[(1-\nu)bN^\nu\beta K_{\text{crit}}\right]^{\frac{1-\nu}{\nu}} + L \right\} \\ &= 0 \end{aligned} \tag{4.10}$$

In the case of Θ-solvent, i.e. $\nu = 1/2$, the above equation can easily be solved for K_{crit}

$$\begin{aligned}\beta K_{\text{crit}}^{(\Theta)} = 2 \Bigg(\frac{L^2}{b^4 N^2} &+ \frac{\beta\gamma d L \left(1 - (M-m)^{1/2} + (M-m-1)^{1/2}\right)}{b^2 N} \\ &- \frac{(M-m)^{3/2} + (M-m-1)^{3/2}}{b^2 N} \Bigg)^{\frac{1}{2}} - \frac{2L}{b^2 N}. \end{aligned} \tag{4.11}$$

For $\beta\gamma d < L/(b^2 N)$ the above result can be approximated by

$$\begin{aligned}\beta K_{\text{crit}}^{(\Theta)} &\approx \beta\gamma d\left(1-(M-m)^{1/2}+(M-m-1)^{1/2}\right)\\ &- \frac{(M-m)^{3/2}}{L}+\frac{(M-m-1)^{3/2}}{L}.\end{aligned} \tag{4.12}$$

In Eq.(4.9) it was shown that ΔL must always be identical zero. The total length of the system at fixed force K and fixed number of defect rods m is then given by

$$L_{\text{tot}} = (m+2)bN^{\nu}\left[(1-\nu)bN^{\nu}\beta K\right]^{\frac{1-\nu}{\nu}} + (m+1)L, \tag{4.13}$$

4.3. Example of a force-extension curve

It is now possible to calculate a force-extension curve for a typical set of parameters and Θ-solvent using Eqs.(4.13, 4.11). The resultant curve is plotted in Fig.(4.3). In this example K_{crit} - see Eq.(4.11) - has a maximum at $m = 5$. Hence the first four rods are pulled out separately with increasing force. This appears in the force-extension curve in form of the small plateaus, see left plot in Fig.(4.3). The force which is large enough to pull out the fifth rod is then also large enough to pull out all the other remaining rods in the micelle.

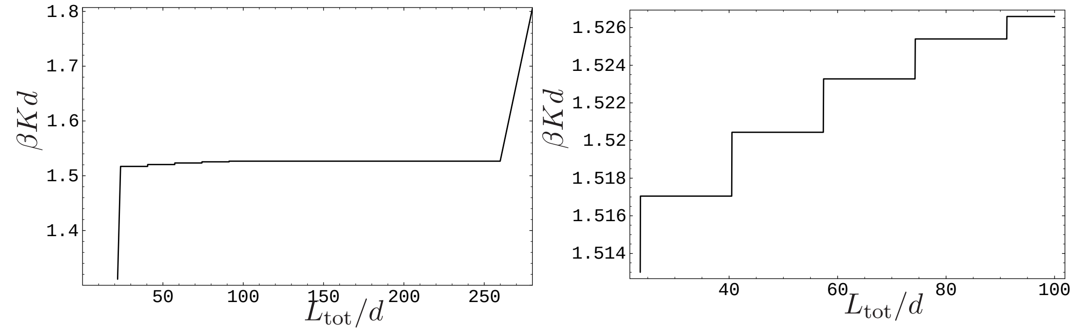

Figure 4.3: Force-extension curve of a multiblock rod-coil copolymer with Gaussian chains. The plot on the right shows a magnification of the region in which four of the rods are pulled out one after the other. Parameters: $M = 15$, $L = 10d$, $b/d = 0.3$, $N = 100$, $\beta\gamma d^2 = 3$

Although the small plateaus corresponding to the detachment of single rods from the micelle appear in the force-extension curves calculated from this scaling theory, in a real experiment one would not be able to see them due to the presence of thermal fluctuations. As can be seen from Fig.(4.3), the increase in force necessary to pull out one more rod from the micelle is roughly $0.003k_BT/d$. The length scale associated with this increase in force is given by the increase of the total length L_{tot} when a new rod is pulled out from the micelle. This is roughly given by $20d$. Hence the associated energy is roughly $0.06k_BT$ which is completely dominated by thermal fluctuations.

The linear increase of the force at the end of the curve after all rods are pulled apart from each other reflects the elastic stretching of the Gaussian chains. When the chains are too strongly stretched, the force extension relation becomes non-linear. The probability distribution of the end-to-end vector for a Gaussian chain, Eq.(2.4), allows for a finite probability of end-to-end distances larger than the contour length of the chain Nb. This is of course unphysical. As long as the end-to-end distance is much smaller than the contour length, the effect of finite extensibility can be neglected. However, for strongly stretched chains it becomes important.

The easiest way to introduce finite extensibility of the flexible chains in the free energy is to ensure by hand that the free energy diverges if the extension of each chain approaches Nb. This can for instance be done by modifying the stretching energy of a Gaussian chain in the following way

$$\left(\frac{R}{N^{1/2}b}\right)^2 \rightarrow \left(\frac{R}{N^{1/2}b}\left[1-\frac{R}{Nb}\right]^{-1}\right)^2 . \tag{4.14}$$

The exponent -1 of the term in square brackets in Eq.(4.14) could also chosen to be smaller or larger yielding a stronger or weaker divergence of the force if the maximum extension $R = Nb$ is approached. The value of the exponent and hence the nature of the divergence of the force depends on the chemical details of the polymer, such as possible bond rotation angles. The considerations here are of a general nature, since there are so far no experiments on the force-extension behaviour of a rod-coil multiblock copolymer to compare with. The exponent is thus chosen to be -1 for simplicity.

With the modification described in Eq.(4.14) the total free energy of a rod-coil multiblock in Θ-solvent at force K is given by

$$\begin{aligned}\beta F(L_{\text{tot}},0,m) &= \beta\gamma dL(M-m)^{1/2} + (M-m)^{3/2}\ln\left(\frac{bN^{1/2}}{d\,(M-m)^{1/4}}\right) + \beta\gamma dLm \\ &+(m+2)\left(\frac{L_{\text{tot}}-(m+1)L-\Delta L}{(m+2)bN^{1/2}}\left[1-\frac{L_{\text{tot}}-(m+1)L-\Delta L}{(m+2)bN}\right]^{-1}\right)^2 \\ &-\beta K L_{\text{tot}}. \end{aligned}\tag{4.15}$$

It is not possible to find a compact analytical expression for L_{tot} or K_{crit} from a minimisation of Eq.(4.15). However, for the set of parameters chosen above, the force-extension curve can be plotted by calculating L_{tot} or K_{crit} numerically, see Fig.(4.4). The unravelling of the micelle is now plotted as a one step process, hence the large plateau without steps. The plateau corresponds to the critical force necessary to pull out the first rod. For large extensions the force-extension relation is clearly non-linear. Note, that the total contour length of the copolymer (including the rods) is $630d$ for the parameters used in the plot.

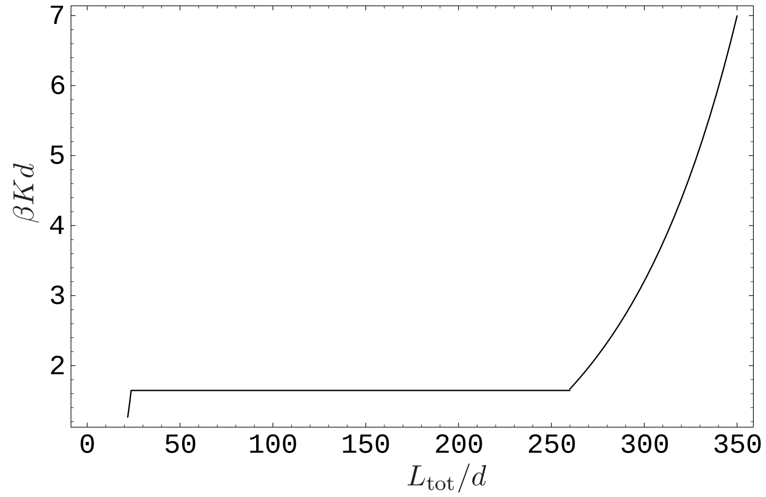

Figure 4.4: Force-extension curve of a multiblock rod-coil copolymer with chains of finite extensibility. Parameters: $M = 15$, $L = 10d$, $b/d = 0.3$, $N = 100$, $\beta\gamma d^2 = 3$

4.4. Analogy to a homopolymer in poor solvent

The response of the rod-coil copolymer in selective solvent to an applied force can be related to the response of a collapsed homopolymer coil in poor solvent [25].

If a force is applied to one end of a homopolymer in a globular state, the globule is first elastically deformed, which can be described by a linear force-extension relation. This stage can be seen as corresponding to the stretching of the end chains of the copolymer without disturbance of the micelle, which - in Θ-solvent - also shows a linear force-extension relation. At a certain force, a stretched string of smaller blobs is pulled out of the globule. The size of these smaller blobs is set by the force, compare [26] or Section 2.4. This scenario occurs at constant force and is characterised by a plateau in the force-extension curve, similar to the plateau in Fig.(4.3), which appears when the rods are pulled out from the micelle. Finally, the globule is completely unravelled to a string of blobs. If the force is further increased this string is stretched elastically, showing again a linear force-extension relation.

Similarly, the rod-coil copolymer also shows a linear force-extension relation after all rods are pulled apart and the connecting chains are elastically stretched.

When the string of blobs is even further stretched a non-linear regime appears as in the case of the rod-coil copolymer due to finite extensibility.

5. Adsorption of rod-coil diblocks at a surface

5.1. Introduction

The previous two chapters dealt with multiblock copolymers of fixed composition immersed in a selective solvent. Their structural behaviour as well as their response to an external force was discussed. This chapter presents a short excursion to rod-coil diblock copolymers. In Section 3.1 it was already mentioned that their phase behaviour is investigated in various papers. However, the structural behaviour of dissolved rod-coil diblocks in the presence of a surface is far less understood. Rod-coil copolymers permanently grafted to a repulsive surface are shown to form 'turnip'- or 'jellyfish'-like micelles on top of the surface [65]. But there seems to exist no study of rod-coil polymers in the presence of an attractive surface.

In this chapter, rod-coil diblocks in selective solvent close to a surface are considered. The surface is assumed to be highly attractive for the rods and neutral to the flexible chains. The solvent is poor for the rods and good for the chains. The rods are assumed to have a certain chemical structure, such that they prefer to be oriented parallel with respect to each rather than antiparallel. The aggregation behaviour of such rod-coil copolymers, showing parallel alignment of the rods only, has been investigated experimentally and computationally, see [3, 62, 63]. The energy penalty for antiparallel alignment of two rods is assumed to be much higher than the energy penalty for these rods being fully exposed to the solvent. In aggregates of these copolymers the flexible parts therefore stick out in one direction only, see Fig.(5.1). If such an aggregate adsorbs with the rods parallel to the surface, the rods shift with respect to each other to allow the chains to gain entropy, see Fig.(5.1).

For simplicity a quasi two-dimensional system is considered. This means that the width of the system in y-direction is equal to the rod diameter d. This system can be viewed as a narrow slice of a system with infinite extension in y-direction. Each of the diblock copolymers under consideration is composed of a stiff rod of length L and diameter d to which a fully flexible chain of N monomers with monomer size b is grafted. The parameters characterising the diblocks are consistent with the one used to describe multiblock copolymers in Chapters 3 and 4. The solvent is

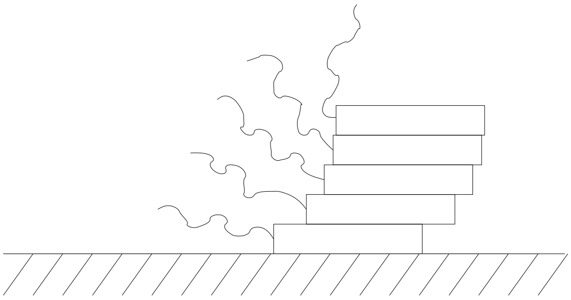

Figure 5.1: Aggregate of rod-coil copolymers adsorbed at a surface. The rods are shifted with respect to each other due to the presence of the surface.

characterised by an energy penalty γ per unit area of a rod exposed to the solvent. The energy gain $-\kappa$ per unit area of a rod in contact with the surface has to be chosen such that an aggregate actually adsorbs to the surface without dissociating into single rod-coil copolymers.

The methods used to describe the adsorbed aggregate are an extension to the scaling methods used in the previous two chapters.

In a first approach in Section 5.2 the shift of the rods is assumed to be constant. A more sophisticated approach allowing the shift to vary with distance from the surface is considered in Section 5.3. The stability of the adsorbed structures and configurations different from the one shown in Fig.(5.1) are discussed in Section 5.4. This section concludes with a 'phase diagram' of the possible rod-coil diblock configurations close to the surface.

5.2. Constant Shift

In a first approach the rods are assumed to shift a constant distance with respect to each other as shown in Fig.(5.2). The characteristic quantity related to this shift is the angle α. This angle can be calculated by calculating the free energy of the entire system as a function of α and minimising it with respect to α.

The free energy consists of two parts. One part is the energy penalty due to the surface of the rods exposed to the solvent. The other one is the free energy of the confined chains. The contributions of the free energy which do not depend on α are of no interest and are therefore neglected. Due to the shift there is additional rod surface exposed to the solvent. This gives rise to an energy penalty, which is given by

$$F_{\mathrm{rod}} = 2\gamma d^2 \tan\alpha. \tag{5.1}$$

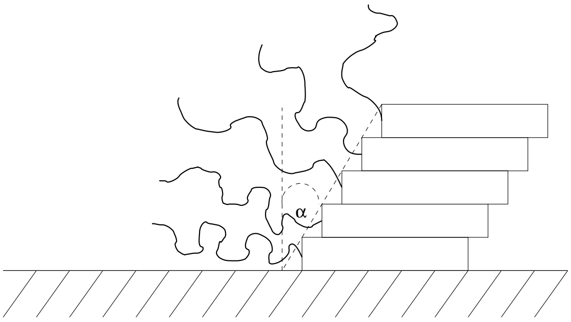

Figure 5.2: The rods are all shifted with respect to each other by the same distance. The shift is characterised by the angle α.

To calculate the free energy of the chains they are treated as if they would form a finite brush grafted to the dashed surface shown in Fig.(5.2). For a finite brush the trajectories of the single polymer chains are not all perpendicular to the grafting surface as for an infinite one. The polymer chains show a splay u. Fig.(5.3) illustrates how this quantity is defined. A chain trajectory starts at the rod at position x and ends at the line $X(x)$. Its splay u is then given by $u(x) = X(x) - x$. The first chain is allowed a splay of $u_0 = h \tan\alpha$ due to the presence of the surface, where h is the brush height. It is given by the equilibrium height of a polymer brush in good solvent, i.e. $h = 4^{-1/3} N \sigma^{1/3} b^{5/3}$ [45, 64]. The last chain can topple over completely and is therefore allowed a splay of $u_L = h$. The grafting density σ of the chains is a function of α as well. It is given by $\sigma(\alpha) = \cos(\alpha)/d^2$.

To calculate the free energy of the finite brush a Flory-type approach is used following the lines of [64] . This means that the free energy is constructed similar to the one used in the Flory argument to calculate the excluded volume exponent ν in Chapter 2, compare Eq.(2.18). Within this approach the free energy consists of an elastic contribution and an excluded volume contribution. The elastic contribution is given by a term proportional to h^2 representing the stretching of the chains away from the rods and a term proportional to $u^2(x)$ representing the stretching of the chains in x direction. The excluded volume contribution is approximated by vN^2/V, where v is the excluded volume parameter or interaction strength and V is the volume available to the polymer. This volume varies from chain to chain and must therefore be calculated for each chain individually. Each chain fills a box of volume $h\sigma^{-1}(1 + u'/2)$, with $u' = \mathrm{d}u/\mathrm{d}x$ [64]. The free energy for the finite brush is then given by

$$\beta F_{\text{brush}} = \frac{d}{Nb^2}\sigma \left(\int_0^D \mathrm{d}x \left[u(x)^2 + h^2 \right] + 4h^2 \int_0^D \mathrm{d}x \left[\frac{1}{2 + u'} \right] \right), \tag{5.2}$$

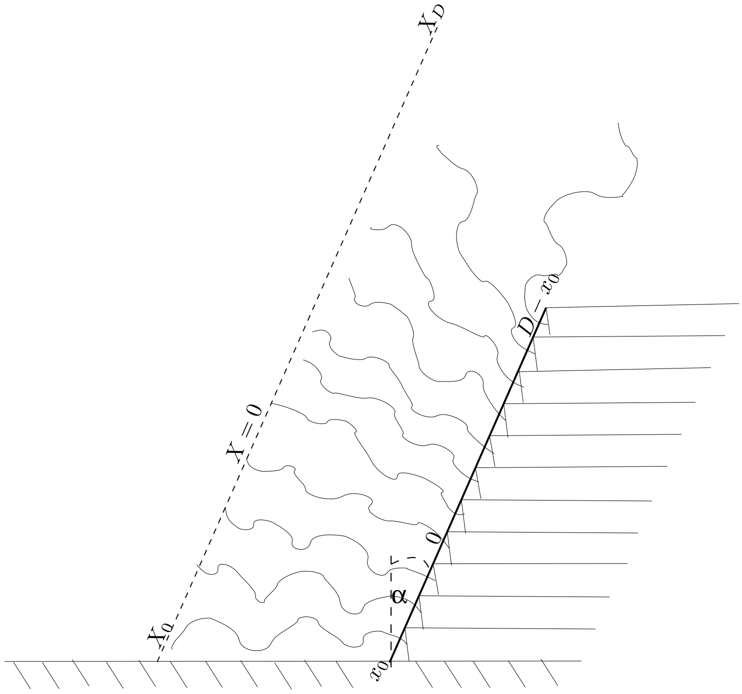

Figure 5.3: This sketch shows how the x-range and the splay are defined. Note: $u(x) = X(x) - x$, i.e. $u_0 = X_0 - x_0$ and $u_D = X_D - (D - x_0)$.

where the first term represents the elastic energy and the second term the excluded volume energy. For simplicity the excluded volume pararmeter is set to $v = b^3$ (compare Section 2.2). D represents the total length of the brush. For the system of aggregates of rod-coil copolymers considered here it is given by $D(\alpha) = f d \cos(\alpha)$. Hence the angle α which characterises the shift enters Eq.(5.2) in form of $\sigma(\alpha)$, $D(\alpha)$ and $u_0(\alpha)$.

In the following an implicit equation for the splay is calculated by functional minimisation of Eq.(5.2) with respect to $u(x)$. The implicit equation is then used to calculate the integrals in Eq.(5.2).

The first integral of the Euler-Lagrange equation for the splay $u(x)$ obtained from Eq.(5.2) is given by

$$u^2 + 8h^2 \frac{1+u'}{(2+u')^2} = C. \tag{5.3}$$

Eq.(5.2) does not distinguish between positive and negative splay. Hence the system has to be separated into two finite brushes which meet at the chain with zero splay, see Fig.(5.3). The position of this chain is determined by the total length of the brush D and the splay at both ends (u_0 and u_D).

It is convenient to introduce dimensionless variables $\tilde{u} = u/(\sqrt{8}h), \tilde{x} = x/(\sqrt{8}h)$ and $\tilde{C} = C/(8h^2)$. Eq.(5.3) can be integrated for arbitrary $\tilde{C}$ which leads to

$$\begin{aligned} \mathrm{I} \qquad & 2\tilde{u} - 2\tilde{u}_D - \ln\left[2\tilde{u} + (1 - 4\tilde{C} + 4\tilde{u}^2)^{1/2}\right] \\ & + \ln\left[2\tilde{u}_D + (1 - 4\tilde{C} + 4\tilde{u}_D^2)^{1/2}\right] = 4(\tilde{D} - \tilde{x}_0 - \tilde{x}). \end{aligned} \tag{5.4}$$

The integration constant can now be calculated by using the condition

$$2\mathrm{I}(\tilde{u} = 0) - \mathrm{I}(\tilde{u} = \tilde{u}_0) = 4\tilde{D}. \tag{5.5}$$

This gives

$$\tilde{C} = \frac{1}{4}\left(1 - (\tilde{u}_0 + \tilde{u}_D)^2 \sinh[2\tilde{D} + \tilde{u}_0 + \tilde{u}_D]^{-2} + (\tilde{u}_0 - \tilde{u}_D)^2 \cosh[2\tilde{D} + \tilde{u}_0 + \tilde{u}_D]^{-2}\right). \tag{5.6}$$

Unfortunately it is not possible to integrate the free energy in Eq.(5.2) directly using the implicit solution for the splay $\tilde{u}$, Eq.(5.4). Therefore an appropriate approximation has to be found. It can be shown that $1 - 4\tilde{C} \approx 0$ holds for all u_0 if $D \geq h$. Hence Eq.(5.4) can be very well approximated as

$$2\tilde{u} - 2\tilde{u}_D - \ln\left[\frac{\tilde{u}}{\tilde{u}_D}\right]\tilde{u} = 4(\tilde{D} - \tilde{x}_0 - \tilde{x}) \quad \text{for} \quad \tilde{u} \geq \tilde{u}_c = \frac{1}{2}(1 - 4\tilde{C})^{1/2}. \tag{5.7}$$

To calculate the free energy the following integration has to be performed:

$$\int \mathrm{d}\tilde{x}\left[\tilde{u}^2 + \frac{1}{2(2 + \tilde{u}')}\right]. \tag{5.8}$$

The regime $0 \leq \tilde{u} \leq \tilde{u}_c$ is considered first:

$$\tilde{u}'(\tilde{x} \leq \tilde{x}_c) \ll 2 \Rightarrow \frac{1}{2(2 + \tilde{u}')} \approx \frac{1}{4}, \qquad \tilde{u}_c^2 \ll \frac{1}{4} \tag{5.9}$$

The integral in Eq.(5.8) in the interval $[0, \tilde{x}_c]$ can therefore safely be approximated by

$$\int_0^{\tilde{x}_c} \mathrm{d}\tilde{x}\left[\tilde{u}^2 + \frac{1}{2(2 + \tilde{u}')}\right] = \frac{1}{4}\tilde{x}_c. \tag{5.10}$$

In the intervall $[\tilde{x}_c, \tilde{D} - \tilde{x}_0]$ the approximation for the splay given by Eq.(5.7) is valid. The integral in eq.(5.8) can then be rewritten in the following form

$$\begin{aligned} \int_{\tilde{x}_c}^{\tilde{D}-\tilde{x}_o} \mathrm{d}\tilde{x}\left[\tilde{u}^2 + \frac{1}{2(2 + \tilde{u}')}\right] &= \frac{1}{2}\int_{\tilde{x}_c}^{\tilde{D}-\tilde{x}_o} \mathrm{d}\tilde{x}\left[\tilde{u}\tilde{u}' - \tilde{u}^2\tilde{u}' - \frac{\tilde{u}'}{4} + \frac{1}{2}\right] \\ &= \left[\frac{\tilde{x}}{4} - \frac{\tilde{u}}{8} + \frac{\tilde{u}^2}{4} - \frac{\tilde{u}^3}{6}\right]_{\tilde{x}_c}^{\tilde{D}-\tilde{x}_o}. \end{aligned} \tag{5.11}$$

By construction $\tilde{u}(\tilde{x}_c) = \tilde{u}_c \ll 1$, see Eq.(5.7). Therefore the integral in Eq.(5.8) in the limits $[0, \tilde{D} - \tilde{x}_0]$ can be very well approximated by

$$\int_0^{\tilde{D}-\tilde{x}_o} \mathrm{d}\tilde{x} \left[\tilde{u}^2 + \frac{1}{2(2+\tilde{u}')}\right] = \frac{\tilde{D} - \tilde{x}_0}{4} - \frac{\tilde{u}_D}{8} + \frac{\tilde{u}_D^2}{4} - \frac{\tilde{u}_D^3}{6}. \tag{5.12}$$

So far only one part of the brush was calculated. The one from the ‘zero splay chain’ to the open end. In Fig.(5.3) this is the part on the right from 0 to $D - x_0$. The left part from 0 to x_0 or rather from the ‘zero splay chain’ to the surface can be calculated completely analogously by replacing $\tilde{D} - \tilde{x}_0$ with $\tilde{x}_0$ and $\tilde{u}_D$ with $\tilde{u}_0$. After adding up the results for both parts in both intervals, accounting for the prefactors in Eq.(5.2) and converting back to variables carrying dimensions the final result for the free energy of the chains forming the finite brush reads

$$\beta F_{\text{brush}} = \frac{d}{Nb^2}\sigma \left[3Dh^2 - h^2(u_0 + u_D) + \frac{h}{\sqrt{2}}(u_0^2 + u_D^2) - \frac{1}{6}(u_0^3 + u_D^3)\right]. \tag{5.13}$$

Plugging in the α-dependent expressions for σ, D, u_0 and u_D and adding the free energy of the rods from Eq.(5.1), the α-dependent part of the total free energy is given by

$$\begin{aligned} \beta F(\alpha) &= 2f\beta\gamma d^2 \tan(\alpha) + \frac{3}{4^{2/3}} f N \left(\frac{b}{d}\right)^{4/3} \cos(\alpha)^{2/3} \\ &+ \frac{N^2}{4}\left(\frac{b}{d}\right)^3 \cos^2(\alpha) \left[\frac{1}{\sqrt{2}} - \frac{7}{6} - \tan(\alpha) + \frac{\tan^2(\alpha)}{\sqrt{2}} - \frac{\tan^3(\alpha)}{6}\right] \end{aligned} \tag{5.14}$$

This equation is only valid for $0 \leq \alpha \leq \pi/4$, because for $\alpha = \pi/4$ the splay at the surface reaches the maximum possible value, i.e. $u_0(\pi/4) = h = u_D$. In the interval $\pi/4 < \alpha < \pi/2$ the splay at the surface remains constant at its maximum value $u_0 = h$. Eq.(5.14) then simplifies to

$$\beta F(\alpha) = 2f\beta\gamma d^2 \tan(\alpha) + \frac{3}{4^{2/3}} f N \left(\frac{b}{d}\right)^{4/3} \cos(\alpha)^{2/3} + \frac{N^2}{2}\left(\frac{b}{d}\right)^3 \cos^2(\alpha) \left[\frac{1}{\sqrt{2}} - \frac{7}{6}\right]. \tag{5.15}$$

There are two regimes in each of which the above free energy, Eqs.(5.14, 5.15), shows a different behaviour. If the chains are rather short the system shows a discontinuous transition. With decreasing γ there is a jump from a stable phase with no shift ($\alpha = 0$) to a stable phase with a large shift ($\alpha \gg 0$). The other regime in which the chains are rather long shows a continuous transition from a stable phase with $\alpha = 0$ to a phase with finite α.

These two regimes can be distinguished by looking at the second derivative of the free energy at $\alpha = 0$. If it is negative the transition can only be discontinuous and if it is positive only continuous. The chain length N_t which separated these two regimes is given by

$$N_\mathrm{t} \approx 1.4 f \left(\frac{d}{b}\right)^{5/3} . \tag{5.16}$$

For $N < N_\mathrm{t}$ the transition is discontinuous and continuous for $N > N_\mathrm{t}$. Physically, this condition can be interpreted such that for $N < N_\mathrm{t}$ the second term in the free energy (Eq.(5.14)) dominates the third term. The second term solely represents the effect of decreasing grafting density, whereas the third term also represents the effect of increasing splay of the chains close to surface. Therefore if the grafting density effect is dominant, the transition is similar to the tilting transition observed in lamellar structures of rod-coil copolymers, see e.g. [29]. Since then the minimum in the free energy is essentially given by the balance of $\tan\alpha$ (first term in Eq.(5.14)) and $\cos\alpha$ (second term) a continuous transition with a minimum at small values of α is not possible. The free energy as a function of α is plotted for different values of γ in Fig.(5.4). The location of the free energy minimum F_0 and the equilibrium shift angle α_0 as functions of γ are plotted in Fig.(5.5).

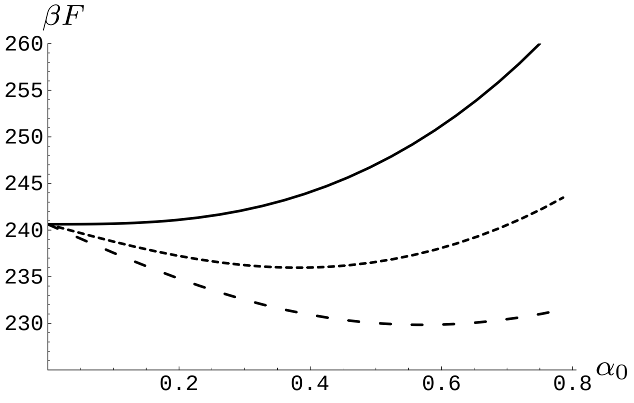

Figure 5.4: This plot shows the dependence of the free energy in units of $k_\mathrm{B}T$ on α for different values of γ in the regime $N < N_\mathrm{t}$. Parameters: $f = 10, b/d = 0.2, N = 50, \beta\gamma d^2 = 1$ (upper curve), 0.25, 0.15 (lower curve). In this regime the effect of decreasing grafting density with increasing α dominates the effect of the splay of the chains close to the surface.

For $N \geq N_\mathrm{t}$ the third term in the free energy, Eq.(5.14), gets equal to or bigger than the second term. This means that the increase in splay of the chains close to the surface becomes important. Since u_0 scales with $\tan\alpha$ like the contribution of the rods (F_rod) does, a continuous transition is now possible. The dependence of the free energy on α for different values of γ is shown in Fig.(5.6).

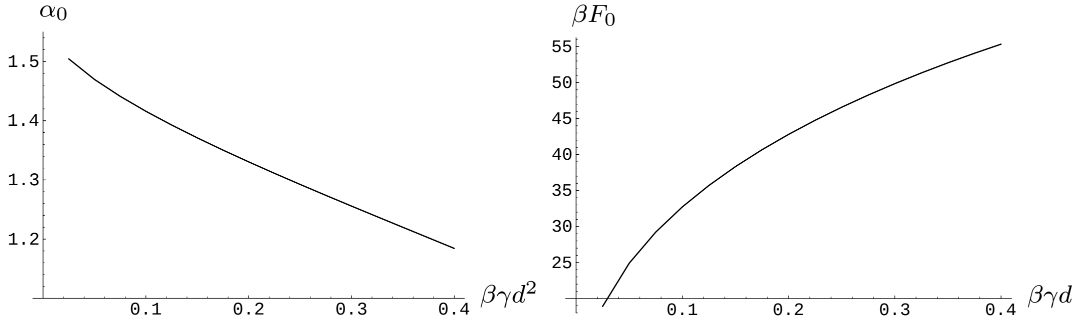

Figure 5.5: The left plot shows the dependence of the angle α_0 that minimises the free energy on γ in the regime $N < N_t$. The right plot shows the dependence of the corresponding free energy minimum in units of $k_B T$ on γ. The other parameters are chosen as in Fig.(5.4): $f = 10, b/d = 0.2, N = 50$. The minimisation of the free energy was done numerically.

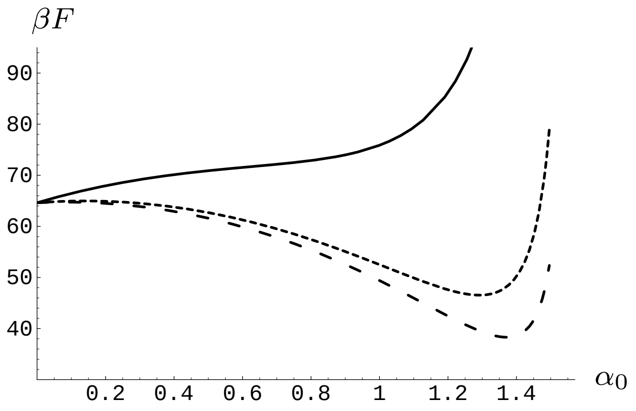

Figure 5.6: This plot shows the dependence of the free energy in units of $k_B T$ on α for different values of γ in the regime $N > N_t$. Parameters: $f = 10, b/d = 0.2, N = 200, \beta\gamma d^2 = 4$ (upper curve), 3, 2.5 (lower curve). In this regime the effect of increasing splay of the chains close to the surface determines the behaviour of the free energy.

In this regime a condition for the appearance of a shift can be found easily. If the first derivative of the free energy at $\alpha = 0$ is positive, no shift is possible. As soon as it becomes negative non-zero shift is possible. The corresponding critical rod-solvent energy is given by

$$\beta\gamma_c d^2 = \frac{N^2}{8f}\left(\frac{b}{d}\right)^3 . \tag{5.17}$$

For $\gamma > \gamma_c$ no shift is possible. If γ becomes smaller than γ_c a non-zero shift continously develops from $\alpha = 0$ on. Fig.(5.7) shows the dependence of the equilibrium shift angle α_0 and the minimum of the free energy F_0 on γ.

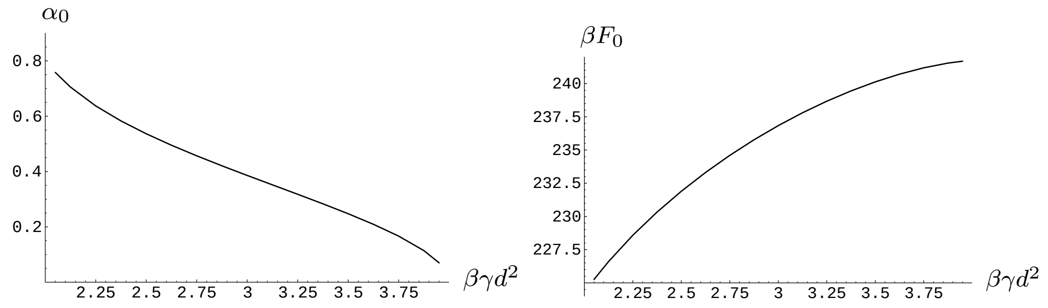

Figure 5.7: The left plot shows the dependence of the angle α_0 that minimises the free energy on γ in the regime $N > N_{\mathrm{t}}$. The right plot shows the dependence of the corresponding free energy minimum in units of $k_{\mathrm{B}}T$ on γ. The other parameters are chosen as in Fig.(5.6): $f = 10, b/d = 0.2, N = 200$. The minimisation of the free energy was done numerically.

The crossover from one regime ($N \geq N_{\mathrm{t}}$) in which a shift develops continuously to a regime ($N < N_{\mathrm{t}}$) in which the system shows a jump from zero shift to large shift would be very interesting result. However, it is most likely to be an artefact of the constant shift assumption. If the shift is allowed to vary with distance from the surface, the regime which shows a jump should disappear. Only in the limit of a very large number of copolymers f forming one lamellar like aggregate the constant shift assumption might be reasonable. However, in this limit the effect of the surface becomes negligible and the system always shows a tilting transition - compare [29] - even if not in contact with the surface.

To gain further insight the shift is allowed to vary with increasing distance from the surface in the next section.

5.3. Variable Shift

In this section a more realistic approach in which the rods are allowed to shift a variable distant with respect to each other is considered. The rods close to the surface are expected to shift more than the rods further away from the surface, since for the corresponding chains close to the surface there is more entropy to gain than for the ones further away. Therefore the equilibrium conformation should be similar to the one shown in Fig.(5.8). The dashed line in Fig.(5.8) can be interpreted as the profile of the shift l as a function of the distance x from the surface. The chains are described by a local Flory-type model similar to the one used in the previous section. In this model the free energy of the system is again given by the sum of an elastic term and an excluded volume term for the chains plus a term which quantifies the energy penalty for the additional rod surface exposed to the solvent due to the shift.

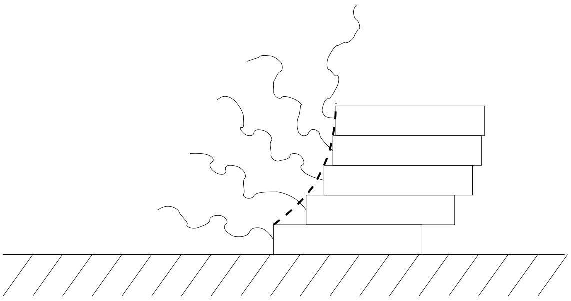

Figure 5.8: The shift of the rods with respect to each other decays with increasing distance from the surface.

The free energy is constructed such that it is a functional of the splay of the chains $u(x)$ and the shift of the rods $l(x)$. At all positions x the shift $l(x)$ is assumed to be small compared to the height h of the brush-like structure formed by the chains. Hence h can assumed to be constant for all x.

Fig.(5.9) helps to explain how the excluded volume term of the free energy is constructed. A chain starts at the rod and ends at the line $X(x)$ shown in Fig.(5.9). It is assumed to fill the volume of the box given by the dashed lines around the chains. This assumption is not valid for the chains far away from the surface, but for these chains the contribution of the excluded volume term is certainly very small. Hence the assumption does not affect the total free energy in a significant way. The splay $u(x)$ is given by $X(x) - x$.

To explain how to calculate the volume available to each chain, Fig.(5.10) shows a larger sketch of one of the dotted boxes surrounding each chain in Fig.(5.9). For the quasi two-dimensional system under consideration the volume is given by the grey area in Fig.(5.10) times the diameter of the rods d. The area $A_i^{(0)}$ shaded in light grey is given by

$$A_i^{(0)} = h\left(d + \Delta u_i/2\right), \tag{5.18}$$

where $\Delta u_i = u_i - u_{i-1}$. It is the area $A_i^{(l)}$ shaded in dark grey where the shift of the rods $l(x)$ comes into play. It is given by

$$A_i^{(l)} = hq_i - \frac{1}{2}l_i q_i. \tag{5.19}$$

As can be seen from Fig.(5.10) the length q_i is given by

$$\begin{aligned} q_i &= l_i\frac{u_{i-1}}{h} = l_i\frac{u_i - \Delta u_i}{h} && (5.20)\\ \Rightarrow A_i^{(l)} &= l_i\left(u_i - \Delta u_i\right)\cdot\left[1 - \frac{l_i}{2h}\right] \approx l_i\left(u_i - \Delta u_i\right). && (5.21)\end{aligned}$$

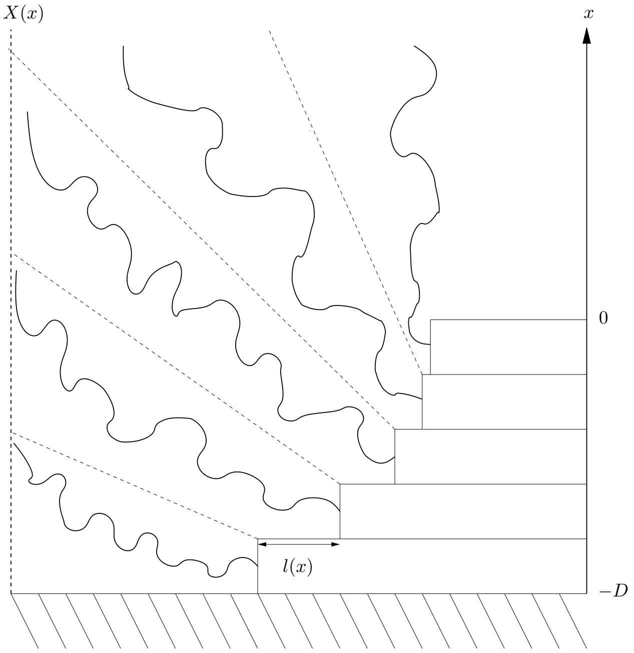

Figure 5.9: This sketch shows the spatial segments or boxes filled by each chain. They get larger with increasing distance from the surface. The shift at each position x is denoted by $l(x)$. x ranges from $-D$ at the surface to 0 at the last rod. The splay of the chains is given by $u(x) = X(x) - x$.

Since l_i is assumed to be small compared to h, the term in the square brackets in Eq.(5.21) can be approximated by 1. In Fig.(5.10) this corresponds to double counting the area of the small triangle with the catheti q_i and l_i. It is convenient to take the continuum limit: $l_i \to l(x)$, $u_i \to u(x)$, $\Delta u_i \to du'(x)$. The total volume $V(x)$ available to a chain at position x is then given by

$$V(x) = d\left(A^{(0)}(x) + A^{(l)}(x)\right). \tag{5.22}$$

Using Eqs.(5.18, 5.21) yields

$$V(x) = d^2h\,(1 + u'(x)/2) + dl(x)(u(x) - du'(x)). \tag{5.23}$$

The elastic term of the free energy is the same as in the previous section.

The energy penalty for the additional area of a rod at position i exposed to the solvent as a function of the shift l_i is simply given by $2\gamma l_i d$. The complete free

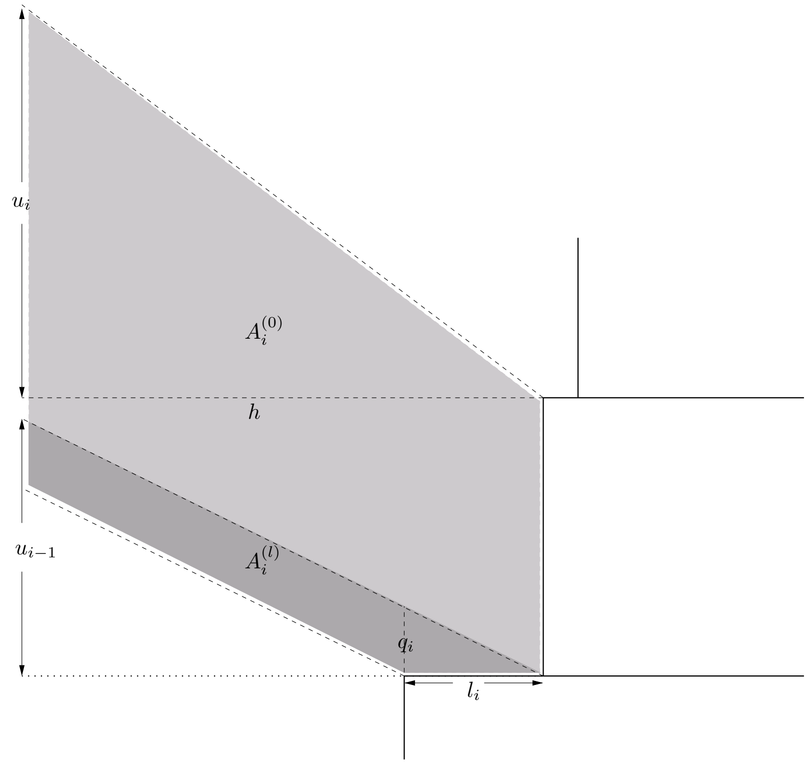

Figure 5.10: This figure shows how the volume occupied by each chain is calculated as a function of splay u and shift l.

energy functional can now be constructed.

$$\begin{aligned}\beta F &= 2\int_{-D}^{0} \mathrm{d}x \beta\gamma l(x) + \frac{1}{Nb^2 d}\int_{-D}^{0} \mathrm{d}x \left[u(x)^2 + h^2\right] \\ &+ \frac{N^2 b^3}{2d}\int_{-D}^{0} \mathrm{d}x \left[\frac{1}{hd^2(1+u'(x)/2) + dl(x)(u(x) - du'(x))}\right] \end{aligned} \quad (5.24)$$

For simplicity all terms which do not depend on either l or u are dropped because they are of no interest for the following considerations and the excluded volume parameter v is set to $v = b^3$ (compare Section 2.2). The excluded volume term in Eq.(5.24) was constructed assuming constant density of monomers for each chain within the box of volume V given by Eq.(5.23). The monomer density close to the rods is larger than the one further away from the rods and therefore this assumption tends to underestimate the excluded volume energy. However, it is the standard approximation used in Flory-type models and has been proven to be sufficient to describe the behaviour of a finite polymer brush, see [64].

Fig.(5.9) shows that the rod at the surface has zero shift since it has no other rod to the left with respect to which it could shift. So for the rod-coil copolymer at the surface the integrand in Eq.(5.24) reduces to the one in Eq.(5.2) from the previous section. This of course also means that the equation for the shift (Eq.(5.27) below) is only valid from the second rod on (as counted from the surface).

To calculate the equilibrium shift $l(x)$ it is necessary to compute the Euler-Lagrange equations from a functional minimisation of Eq.(5.24) with respect to $u(x)$ and $l(x)$. The Euler-Lagrange equation for the splay $\tilde{u}$ has the the first integral

$$\begin{aligned} & 2\beta\gamma l(x) + \frac{u(x)^2 + h^2}{Nb^2 d} \\ & + \frac{N^2 b^3}{d}\left[\frac{1}{hd^2(2+u'(x)) + 2dl(x)(u(x) - du'(x))}\right. \\ & + \left.\frac{(h - 2l(x))\, u'(x)}{\left(hd(2+u'(x)) + 2l(x)(u(x) - du'(x))\right)^2}\right] = C_1. \end{aligned} \tag{5.25}$$

Variation of Eq.(5.24) with respect to $l(x)$ yields

$$2\beta\gamma + \frac{2N^2 b^3}{d^2}\left[\frac{u(x) - du'(x)}{\left(hd(2+u'(x)) + 2l(x)(u(x) - du'(x))\right)^2}\right] = 0. \tag{5.26}$$

The quadratic Eq.(5.26) can be solved for the shift $l(x)$.

$$l(x) = \frac{\left(\frac{b^3 N^2}{d^2 \beta\gamma}(u(x) - du'(x))\right)^{\frac{1}{2}} - hd(2 + u'(x))}{2(u - du'(x))} \tag{5.27}$$

Inserting the expression for the shift - i.e. Eq.(5.27) - into Eq.(5.25) results in a very complicated, highly nonlinear differential equation which cannot be solved exactly. However, the overall effect of the shift on the free energy is certainly smaller than the overall effect of the splay. Thus it is a reasonable approximation to calculate the solution for the splay at zero shift and to use this as an approximation for the splay u in Eq.(5.27). This approximation breaks down when the splay becomes very small close to the surface. But for zero splay the shift should be constant. The shape of the profile of the shift away from the surface at finite splay can therefore be calculated within this approximation.

In the following an approximate solution of the splay u for zero l is calculated. Setting the shift $l(x)$ identical zero in Eq.(5.25) the differential equation reduces to

$$\frac{u(x)^2 + h^2}{Nb^2 d} + \frac{2N^2 b^3}{hd^3}\left[\frac{1 + u'(x)}{(2 + u'(x))^2}\right] = C_1 \tag{5.28}$$

$$\Rightarrow u^2 + 8h^2 \frac{1 + u'}{(2 + u')^2} = C_2 \tag{5.29}$$

which is Eq.(5.3) from the previous section.

At this point it is again convenient to introduce dimensionless variables marked by a tilde. They are defined as in the previous section, e.g. $\tilde{u} = u/(\sqrt{8}h)$. Eq.(5.29) can be integrated for arbitrary $\tilde{C}_2$ which leads to an implicit equation for the splay $\tilde{u}(\tilde{x})$ similar to Eq.(5.4)

$$2\tilde{u}_0 - 2\tilde{u} + \ln\left[2\tilde{u} + (1 - 4\tilde{C}_2 + 4\tilde{u}^2)^{1/2}\right] - \ln\left[2\tilde{u}_0 + (1 - 4\tilde{C}_2 + 4\tilde{u}_0^2)^{1/2}\right] = 4\tilde{x}. \quad (5.30)$$

Note that $-\tilde{D} \leq \tilde{x} \leq 0$. The integration constant $\tilde{C}_2$ can be determined by using the boundary condition $\tilde{u}(-\tilde{D}) = 0$ - i.e. zero splay at the surface, see Fig.(5.9).

$$\tilde{C}_2 = \frac{1}{4}\left(1 - \tilde{u}_0^2 \sinh\left[2\tilde{D} + \tilde{u}_0\right]^{-2} + \tilde{u}_0^2 \cosh\left[2\tilde{D} + \tilde{u}_0\right]^{-2}\right) \quad (5.31)$$

The chain furthest away from the surface at $x = 0$ can topple over completely and is therefore allowed a splay $u_0 = h$ or $\tilde{u}_0 = 1/\sqrt{8}$. Therewith Eqs.(5.30, 5.31) reduce to

$$\begin{aligned} 1/\sqrt{2} - 2\tilde{u} + \ln\left[2\tilde{u} + (1 - 4\tilde{C}_2 + 4\tilde{u}^2)^{1/2}\right] & \\ - \ln\left[1/\sqrt{2} + (3/2 - 4\tilde{C}_2)^{1/2}\right] &= 4\tilde{x} \quad (5.32) \\ \tilde{C}_2 = \frac{1}{8}\left(2 - \sinh\left[4\tilde{D} + 1/\sqrt{2}\right]^{-2}\right). & \quad (5.33) \end{aligned}$$

It is not possible to resolve Eq.(5.32) with respect to the splay u. However, x is known as a function of u, u' as a function of u (see Eq.(5.29)) and l as function of u and u'. Hence, for a certain set of parameters, the shift l can be plotted as a function of x by either numerically resolving Eq.(5.32) or by showing a parameter plot of l versus x, using u as a parameter. This is done for a characteristic set of parameters in Fig.(5.11). The plot demonstrates that the assumption for the profile of the splay in Fig.(5.8) was quite reasonable.

Now an approximate explicit expression for small values of the splay $\tilde{u}$ is calculated. For $\tilde{u} \ll 1$ the logarithmic term dominates the linear term in Eq.(5.32). Neglecting the linear term $2\tilde{u}$, Eq.(5.32) can be converted to

$$\frac{2\tilde{u} + (1 - 4\tilde{C}_2 + 4\tilde{u}^2)^{1/2}}{1/\sqrt{2} + (3/2 - 4\tilde{C}_2)^{1/2}} = e^{4\tilde{x} - 1/\sqrt{2}} \quad (5.34)$$

$$\Rightarrow \tilde{u} = \frac{\sinh\left[4(\tilde{D} + \tilde{x})\right]}{\sqrt{8}\sinh\left[4\tilde{D} + 1/\sqrt{2}\right]}. \quad (5.35)$$

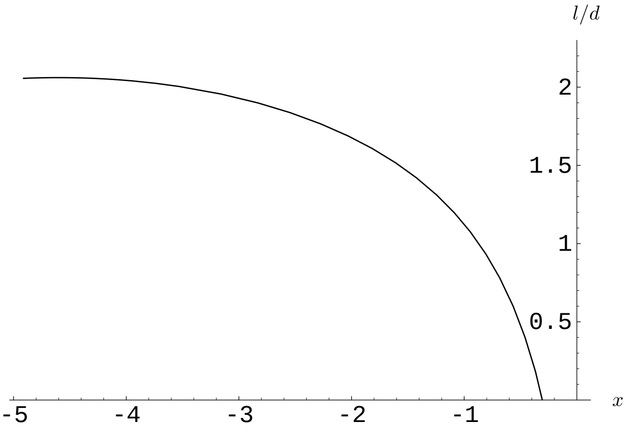

Figure 5.11: The shift l is plotted as a function of negative distance from the outmost rod towards the surface. The outmost rod (the one furthest away from the surface) is located at $x = 0$, compare Fig.(5.9). Parameters: $N = 700, b/d = 0.1, \beta\gamma d^2 = 1$

Transforming back to variables carrying dimensions yields

$$u = h\frac{\sinh\left[\sqrt{2}(D+x)/h\right]}{\sinh\left[(\sqrt{2}D/h + 1/\sqrt{2}\right]}, \tag{5.36}$$

$$u' = \sqrt{2}\frac{\cosh\left[\sqrt{2}(D+x)/h\right]}{\sinh\left[(\sqrt{2}D/h + 1/\sqrt{2}\right]}. \tag{5.37}$$

The splay decays rather fast from the open end inwards. Numerical estimates show that Eqs.(5.36, 5.37) are actually a rather good approximation for the splay from D up to $D/2$. Eqs.(5.36, 5.37) and Eq.(5.27) would form an explicit analytic expression for the shift l as a function of x close to the surface. But for most parameter combinations this corresponds to a regime in which the effect of the splay is smaller than the effect of the shift. Therefore the splay can no longer be calculated independent from the shift and the above result for the splay is no longer a good approximation in the presence of the shift.

For large splay, the implicit solution for the splay u, Eq.(5.30), can be expanded in a power series around the maximum splay u_0. Unfortunately, an expansion up to quadratic order gives only a reasonable numerical agreement for values of u very close to u_0. If higher order terms are taken into account, the solution for u gets to complicated to be of any instructive use.

It is nevertheless possible to estimate the threshold value of γ above which the energy penalty for additional rod-solvent exposure becomes to large for a shift to occur. The shift is identically zero if the right hand side of Eq.(5.27) is less or equal to zero for all x.

$$\frac{\left(\frac{b^3N^2}{d^2\beta\gamma}(u(x)-du'(x))\right)^{\frac{1}{2}}-hd(2+u'(x))}{2(u-du'(x))}\leq 0$$
$$\Rightarrow \beta\gamma \geq \frac{b^3N^2(u(x)-du'(x))}{h^2d^4(2+u'(x))^2}. \tag{5.38}$$

To find an upper limit for the threshold value γ_c note that the maximum value of the shift is $u_0 = h$. An upper estimate for $(u(x)-du'(x))/(2+u'(x))^2$ is therefore given by $4h$. The upper limit for γ_c is thus given by

$$\beta\gamma_c \approx \frac{b^3N^2}{4hd^4} \approx 0.4\frac{N}{d^2}\left(\frac{b}{d}\right)^{\frac{4}{3}}. \tag{5.39}$$

For the set of parameters chosen in Fig.(5.11) this yields $\beta\gamma_c d^2 \approx 13$.

In this section an attempt was made to describe a variable shift $l(x)$. For values of the splay $u(x)$ which are big enough to dominate the effect of the shift a set of equations (5.27, 5.32, 5.33) was found which determines l as a function of u and u as a function of x. Although it is not possible to resolve Eq.(5.32) with respect to u, the profile of the shift can be plotted for a certain set of parameters, see Fig.(5.11). In this section and in the previous one it was always assumed that the adsorbed aggregate is stable and does not disintegrate. The next section discusses under which conditions this is case and which other configurations are possible.

5.4. Stability and other possible configurations

In the previous section it was assumed that a configuration of f rod-coil copolymers at a surface as it is pictured in Fig.(5.8) is actually stable. There are three other possible configurations

In the quasi two-dimensional system considered here only one rod is in contact with the surface. Therefore a possible configuration is the one shown in Fig.(5.12), where one single copolymer is adsorbed at the surface and the others form a detached sheet. Such a situation is called detached configuration in the following. The energy of the rod-surface contact in this configuration is the same as for the attached one considered in the previous section.

A configuration with different contact energy is the mushroom-like one as depicted in Fig.(5.13). This configuration is always preferable to a complete detachment of the aggregate since in the latter case the system would gain no contact energy.

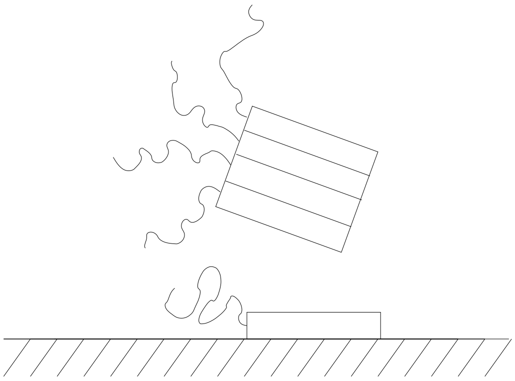

Figure 5.12: For long chains a detachment of the aggregate from the rod adsorbed to the surface might be preferable.

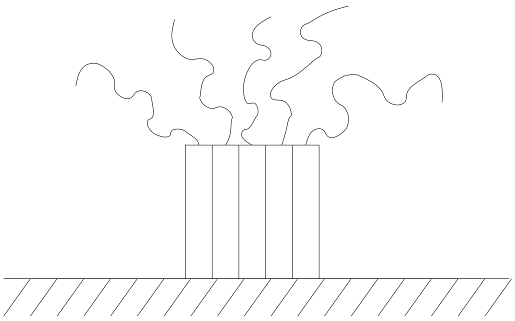

Figure 5.13: Another possible configuration: The aggregated rods adsorb perpendicular to the surface. This configuration is preferable for large aggregates.

The last possible configuration is a complete dissociation of the aggregate into single copolymers due to the presence of the attractive surface. These single copolymers then adsorb individually at the surface, see Fig.(5.14). This configuration yields the highest gain of contact energy. However, it is also the configuration with the highest energy penalty for exposure of rod surface to the solvent. For very high contact energy, i.e. $\kappa \gg \gamma$, the system always dissociates. On the other hand, if κ is to small the system might prefer the mushroom configuration even for long rods, since it allows the chains to gain entropy without much increase in exposure of the rods to the solvent.

By estimating the free energies of these configurations and comparing them with the one of the attached configuration, it is possible to find the range of κ in which the attached configuration is stable. To achieve this at least approximatively the free energy of the attached configuration with zero shift is calculated. It gives a slight overestimation of the free energy of the configuration considered in Section

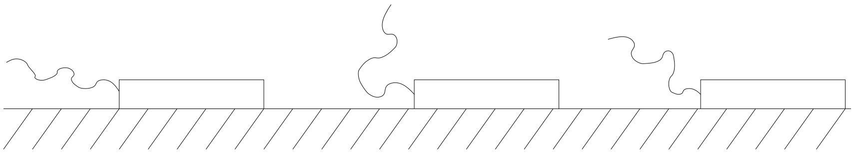

Figure 5.14: The aggregate dissociates and the individual rods adsorb at the surface. This configuration is preferred for large κ.

3. However, it still provides a rough estimate for the parameter range in which the attached configuration is stable. At zero shift the chains form a finite brush. Its free energy is calculated in Section 2 and given by Eq.(5.13). One side of the brush is free and therefore allowed a splay of $u_0 = h$, the other side is confined by the surface, i.e. $u_D = 0$. The length D is given by fd. The free energy of the attached configuration then reads

$$\beta F_{\text{attach}} = \frac{1}{Nb^2 d}\left[3fdh^2 - \left(\frac{7}{6} - \frac{1}{\sqrt{2}}\right)h^3\right]. \tag{5.40}$$

βF_{attach} is used as a reference energy and energy gains and penalties due to rod-surface contact or rod-solvent exposure are added to the free energies of the other configurations.

Compared to the attached configuration, the contact energy of the mushroom differs by $\kappa(Ld - fd^2)$. The chains can also be modelled as a finite brush. Here both ends are free and are therefore allowed a splay of $u_0 = u_D = h$. The free energy of the mushroom configuration is hence given by

$$\begin{aligned}\beta F_{\text{mushroom}} &= \kappa\left(dL - fd^2\right)\\ &+ \frac{1}{Nb^2 d}\left[3fdh^2 - \left(\frac{7}{3} - \sqrt{2}\right)h^3\right].\end{aligned} \tag{5.41}$$

The attached configuration is preferred to the mushroom configuration if $F_{\text{attach}} < F_{\text{mushroom}}$. This yields the following condition for κ

$$\beta\kappa > \frac{0.12N^2}{Ld - fd^2}\left(\frac{b}{d}\right)^3. \tag{5.42}$$

This is the lower bound for κ. To get the upper bound the free energy of the dissociated copolymers - see Fig.(5.14) - has to be estimated.

Compared to the attached configuration, the dissociated one yields a contact energy gain of $-(f-1)\kappa Ld$. But on the other hand it also gives rise to an additional energy penalty of $2(f-1)\gamma Ld$. Within this Flory-type theory the flexible chains of the individual copolymers at the surface can be treated as free ones and their free energy can be neglected. Comparison of F_{attach} and $2(f-1)\gamma Ld - (f-1)\kappa Ld$ yields the upper limit of κ above which the system dissociates:

$$\beta\kappa < 2\beta\gamma - \frac{1}{(f-1)Ld^2}\left[1.2fdN\left(\frac{b}{d}\right)^{\frac{4}{3}} - 0.12N^2b\left(\frac{b}{d}\right)^2\right]. \tag{5.43}$$

Within this range of values for κ the attached configuration can actually be stable. For the parameters chosen in Fig.(5.11), $N = 700, b/d = 0.1, \beta\gamma d^2 = 1$ and $L/d = 80$, $f = 30$, the range of stability is given by $1.18 < \beta\kappa d^2 < 1.52$.

It is also of interest to keep κ and γ fixed and to investigate which configuration is preferred for different combinations of molecular properties. The most characteristic properties are rod length L (or aspect ratio L/d) and number of chain monomers N. Therefore the critical rod lengths which separate each of two of the possible configurations from each other are calculated as functions of N and of the other parameters. They are then used to calculate a phase diagram of the configurations in L-N space.

Eq.(5.42) can be rearranged such that it gives the critical rod length below which the system changes from the attached to the mushroom configuration.

$$L^{\text{attach}}_{\text{mushroom}} \approx fd + 0.12\frac{N^2b}{\beta\kappa d^2}\left(\frac{b}{d}\right)^2 \tag{5.44}$$

Comparison of F_{mushroom} with the energy of the dissociated configuration yields the rod length $L^{\text{mushroom}}_{\text{dissociate}}$ which separates the mushroom from the dissociated configuration.

$$L^{\text{mushroom}}_{\text{dissociate}} \approx \frac{1.2fdN\left(\frac{b}{d}\right)^{4/3} - 0.24N^2b\left(\frac{b}{d}\right)^2 - fd\beta\kappa d^2}{2(f-1)\beta\gamma d^2 - f\beta\kappa d^2} \tag{5.45}$$

In case of rather large κ (close to the upper limit) there might exist a rod length which directly separates the attached configuration from the dissociated configuration. It is found to be

$$L^{\text{attach}}_{\text{dissociate}} \approx \frac{1.2fdN\left(\frac{b}{d}\right)^{4/3} - 0.12N^2b\left(\frac{b}{d}\right)^2}{(f-1)\beta d^2(2\gamma-\kappa)}. \tag{5.46}$$

Now the detached configuration as depicted in Fig.(5.12) is considered. Compared to the attached configuration its free energy has a contribution from two additional rod surfaces being exposed to the solvent, which is given by $2Ld\gamma$. The free energy of the chains of the detached sheet is similar to the one of the mushroom configuration with $D = f-1$. The free energy of the chain of the single copolymer can be neglected as in the case of dissociation. F_{detach} is hence given by

$$\beta F_{\text{detach}} = 2Ld\beta\gamma + \frac{1}{Nb^2d}\left[3(f-1)dh^2 - \left(\frac{7}{3} - \sqrt{2}\right)h^3\right]. \tag{5.47}$$

The rod length $L_{\text{attach}}^{\text{detach}}$ which separates the detached and the attached configuration can now be estimated.

$$L_{\text{attach}}^{\text{detach}} \approx 0.6\frac{N}{d\beta\gamma}\left(\frac{b}{d}\right)^{\frac{4}{3}} + 0.06\frac{N^2}{d\beta\gamma}\left(\frac{b}{d}\right)^3 \tag{5.48}$$

However, in a wide range of parameters the detached configuration sits in between the mushroom and the dissociated configuration. Therefore equating Eq.(5.41) and Eq.(5.47) gives the rod length which separates mushroom and detached configuration.

$$L_{\text{detach}}^{\text{mushroom}} \approx \left(fd - 1.2\frac{Nd}{\beta\kappa d^2}\left(\frac{b}{d}\right)^{\frac{4}{3}}\right)\cdot\left(1-\frac{\gamma}{\kappa}\right)^{-1} \tag{5.49}$$

The length $L_{\text{dissociate}}^{\text{detach}}$ which separates the detached from the dissociated configuration is found to be

$$L_{\text{dissociate}}^{\text{detach}} \approx \frac{1.2(f-1)dN\left(\frac{b}{d}\right)^{4/3} - 0.24N^2b\left(\frac{b}{d}\right)^2}{2(f-2)\beta\gamma d^2 - (f-1)\beta\kappa d^2)}. \tag{5.50}$$

As already mentioned above, these critical rod lengths can be used to calculate a phase diagram of the configurations in L-N space, which - for a typical set of parameters - is shown in Fig.(5.15). Note, that the phase diagram shown in Fig.(5.15) is only one example. For different parameter combinations some of the configurations might not be accessible for the system. The contact energy per unit area κ is chosen such that there exists a region in L-N space in which the entropy loss of the confined chains is compensated by the energy gain due to rod-surface contact. But it is also chosen to be not much larger than the rod-rod contact energy γ, since otherwise the aggregate would dissociate. However, for very long chains the aggregate always dissociates into single copolymers which then individually adsorb. Nevertheless, Fig.(5.15) shows that there is indeed a broad region in L-N space in which the attached configuration is stable and the rods shift with respect to each other as discussed in Section 3.

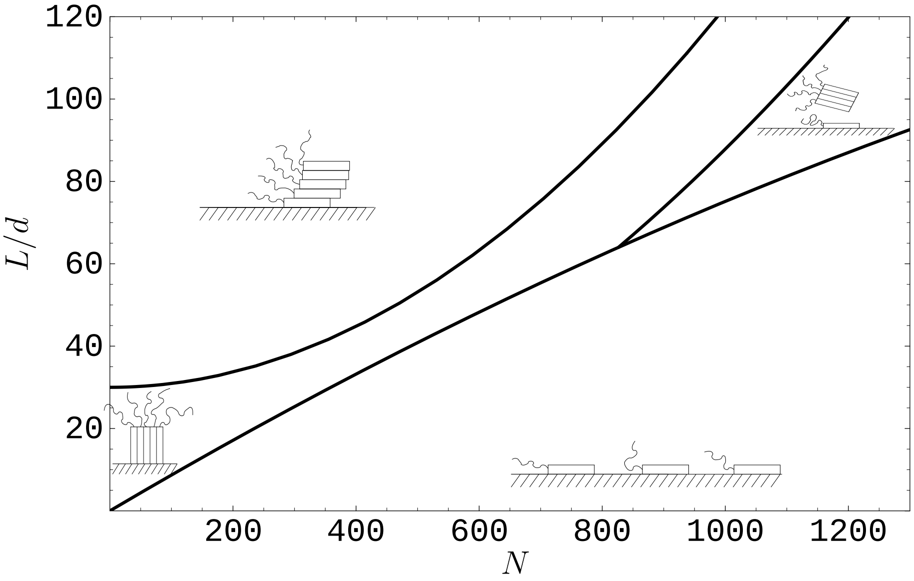

Figure 5.15: Configurations of the rod-coil copolymers at the surface. Parameters: $b/d = 0.1, f = 30, \beta\gamma d^2 = 1, \beta\kappa d^2 = 1.3$

6. Rod-coil copolymer with variable composition

6.1. Variable composition and the helix-coil transition

In Chapters 3 and 4 a multiblock copolymer with fixed composition of stiff and flexible parts was discussed. The restriction of fixed composition will now be released. Each segment is now allowed to undergo a microscopic transition from flexible to stiff and vice versa. The equilibrium composition of stiff and flexible segments is determined by the specific structure of the entire copolymer. The specific structure is also influenced by the composition of stiff and flexible segments. Helix-forming polymers are polymers with a variable composition of stiff and flexible segments. The most common examples are polypeptides (i.e. chains of amino acids, for instance proteins) and chains of nucleic acids (RNA and DNA) [2]. In addition, there are also synthetic polymers that can form helical structures in solution, for instance polyisocyanide [70] or polybenzylglutamate [55, 71].

Significant work has been done to investigate the helix-coil transition theoretically [52] and computationally [68, 69]. One of the first and most well-known approaches is the Zimm-Bragg theory [8, 55]. It considers a one-dimensional Ising type model in which each segment can be in one of the two states: helical state (stiff) or coil state (flexible). All interactions between different segments along the chain are neglected. The helix is stabilised by hydrogen bonds which generates an energy gain of $-\epsilon$ for each segment in the helical state. This energy gain is partly balanced by an entropy loss $-\Delta S$. The free energy difference between the helical state and the coil state is therefore given by $\Delta f = -\epsilon + T\Delta S$ for each segment.

In an α-helix hydrogen bonds can only form between the i^{th} and the $(i+3)^{\mathrm{th}}$ peptide group. The formation of a hydrogen bond between the first and the third peptide group requires fixing the conformation of three groups. The next bond between the second and the fourth group furnishes the same energy gain but requires fixing only one new group and thus leads to a much smaller entropy loss. The formation of an α-helix is therefore a cooperative process and the formation of a junction between helix and coil is energetically unfavourable. This can be modelled by an energy penalty μ_{J} for each junction between a stretch of helical segments and a stretch of flexible segments. Similar arguments hold for all kind of helices. Helix formation is always a cooperative process.

It is convenient to define the following fugacities

$$s \equiv e^{-\beta\Delta f}, \quad \sigma \equiv e^{-2\beta\mu_{\mathrm{J}}}, \tag{6.1}$$

where s gives the statistical weight of a helical segment compared to a coil segment. The cooperativity parameter σ and gives the statistical weight of a junction point. $\sigma = 1$ corresponds to $\mu_{\mathrm{J}} = 0$ and therefore to a non-cooperative system. $\sigma \to 0$ corresponds to $\mu_{\mathrm{J}} \to \infty$ and therefore to a totally cooperative system, i.e. either the entire chain forms one big helix or no helix is formed at all. In most helix forming biopolymers σ is roughly $10^{-3} - 10^{-4}$ [8].

Using a transfer matrix method [8] the one dimensional model can be solved exactly. For the fraction of stiff helical segment $\Theta_{\mathrm{R}} = N_{\mathrm{R}}/N$ as a function of s and σ one obtains

$$\Theta_{\mathrm{R}} = \frac{1}{2} + \frac{s-1}{2\left[(s-1)^2 + 4s\sigma\right]^{1/2}}. \tag{6.2}$$

Fig.(6.1) shows $\Theta_{\mathrm{R}}(s)$ for three different values of σ. With increasing cooperativity the transition from almost zero fraction of stiff segments to almost zero fraction of flexible segments becomes sharper and sharper. Note, that at $s = 1$ energy gain and entropy loss are exactly balanced, which leads to $\Theta_{\mathrm{R}} = 1/2$. For $s < 1$ the entropy loss is larger than the energy gain, for $s > 1$ it is smaller. This rather sharp crossover transition due to the cooperativity effect is also observed experimentally, for instance in polybenzylglutamate [55] or single- and double-stranded DNA [72].

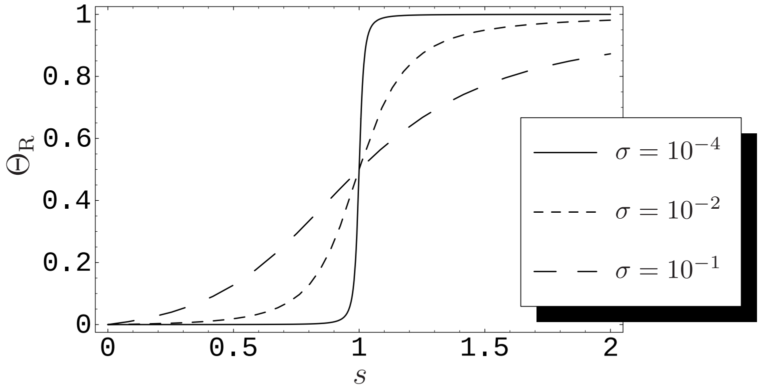

Figure 6.1: Helix-coil transition in the Zimm-Bragg model. The fraction of stiff segments Θ_{R} is plotted as a function of s for three different cooperativities.

Several extensions have been made to this one-dimensional Ising type model. It has been shown [73] that the transitions becomes less cooperative, if the hydrogen-bonding ability of the solvent is taken into account. The helix-coil transition in grafted chains was studied [74] as well as the effect of an external applied force on the transition [75]. The latter study showed that in the limit of very high cooperativity $\sigma \to 0$ the force extension curve of a homopolypeptide shows a plateau corresponding to the sharp transition from coil to helix. In this case the force extension curve looks similar to the one observed in Section 4.3, albeit the physical phenomenon behind the plateau is different.

Of special interest is the application of the one-dimensional models to proteins, see for instance [76, 77]. A study of the helix-coil transition including long-range electrostatic interactions [78] can, to some extent, explain the amount and location of helical segments in globular proteins. However, to understand how α-helices (or generally secondary structure elements) are formed in the folding process of a protein and how this influences the compaction and formation of tertiary structure (and vice versa), it is necessary to combine the one-dimensional physics of the helix-coil transition with three-dimensional interactions of segments along the chain. This enables a description of the interplay between the microscopic transition for each segment and the mesoscopic structure formation of the entire copolymer mentioned in the first paragraph.

In proteins the stiff helical parts are often hydrophobic, such that this hydrophobicity drives the protein into a compact globular phase. Hydrophobic means that the solvent, in this case physiological saline, is poor for the stiff parts, similar to the considerations in Chapter 3. Statistical analysis of the data from 41 globular proteins in native and partially folded conformational states [79] showed a strong correlation between the amount of secondary structure elements and compactness of the proteins. This indicates that the formation of secondary structure (for instance α-helices) and the hydrophobic collapse into a compact globule occur simultaneously. This problem has been partially discussed within computer simulations of globular proteins [53, 54, 80]. The interplay of compaction and secondary structure formation leads to the formation of the specific three-dimensional tertiary structure. Computational and experimental studies of this mechanism can for instance be found in [81, 82]. A general review on physical approaches to the problem of protein folding is given by [83].

To study the interplay of helix-coil (or stiff-flexible) transition and collapse transition of the polymer into a compact globule, an approach is developed which combines variable composition with three-dimensional excluded volume interactions using self-consistent field theory.

In this section the microscopic helix-coil transition and its application to proteins was discussed. In the following sections the field theory for the rod-coil (or helix-coil) multiblock with variable composition is introduced. Below the term rod-coil multiblock copolymer rather than helix-coil is mainly used. The model is not limited to the description of proteins, but is rather meant to provide a general theory to study rod-coil copolymers with variable composition. First, the canonical partition function for the rod-coil multiblock is derived. To allow for a variable composition, a grand canonical description of the system is needed. The grand canonical partition function is represented in terms of a field theory. This is a rather formal and technical procedure and therefore placed in Appendix A. In a self-consistent field treatment, the saddle point grand potential is then minimised with respect to the fields which leads to a set of differential equations for the self-consistent fields.

6.2. Microscopic model and canonical partition function

This section introduces the microscopic model and its canonical partition function. The grand canonical partition function which allows for a variable composition, is derived in the following section and in Appendix A.

The Edwards Hamiltonian for a flexible polymer chain with two-body excluded volume interactions was introduced in Section 2.2. It is given by

$$\beta H_{\mathrm{E}} = \frac{3}{2b^2}\int_0^N \mathrm{d}s \left(\frac{\partial \mathbf{r}}{\partial s}\right)^2 + \frac{v}{2}\int_0^N \mathrm{d}s \int_0^N \mathrm{d}s'\, \delta(\mathbf{r}(s) - \mathbf{r}(s')). \tag{6.3}$$

The two-body interaction constant (or excluded volume parameter) v will later chosen to be negative to describe attractive interaction. To prevent the polymer from collapsing to a point it is therefore necessary to introduce a repulsive three-body interaction with positive interaction parameter w. The complete Edwards Hamiltonian for one flexible part of the copolymer then reads

$$\begin{aligned}\beta H_{\mathrm{coil}} &= \frac{3}{2b^2}\int_0^N \mathrm{d}s \left(\frac{\partial \mathbf{r}}{\partial s}\right)^2 + \frac{v}{2}\int_0^N \mathrm{d}s \int_0^N \mathrm{d}s'\, \delta(\mathbf{r}(s) - \mathbf{r}(s')) \\ &+ \frac{w}{3!}\int_0^N \mathrm{d}s \int_0^N \mathrm{d}s' \int_0^N \mathrm{d}s''\, \delta(\mathbf{r}(s) - \mathbf{r}(s'))\delta(\mathbf{r}(s') - \mathbf{r}(s'')). \end{aligned} \tag{6.4}$$

To construct the Hamiltonian of the entire copolymer it is convenient to introduce microscopic segment densities. Before this can be done, it is necessary to find a suitable parameterisation for the copolymer. The multiblock copolymer may be composed of K rod-coil blocks. In Fig.(6.2) two successive ($n-1$, n) blocks and their parameterisation are shown. The conformation of the rod-coil block number

n is given by the vector-function $\mathbf{r}_n(s)$ describing the contour of the coil, the vector $\mathbf{R}_n$ gives the position of the junction point between rod and coil and the unit vector $\mathbf{u}_n$ describes the orientation of the rod. The length of the n^{th} rod-coil block in units of the segment length b is given by N_n. The fraction of the flexible segments (coil) is given by f_n and the fraction of stiff segments (rod) thus by $1 - f_n$. The microscopic flexible segment density $\hat{\rho}_{\mathrm{C}}(\mathbf{r})$ and stiff segment density $\hat{\rho}_{\mathrm{R}}(\mathbf{r})$ can now be defined as follows

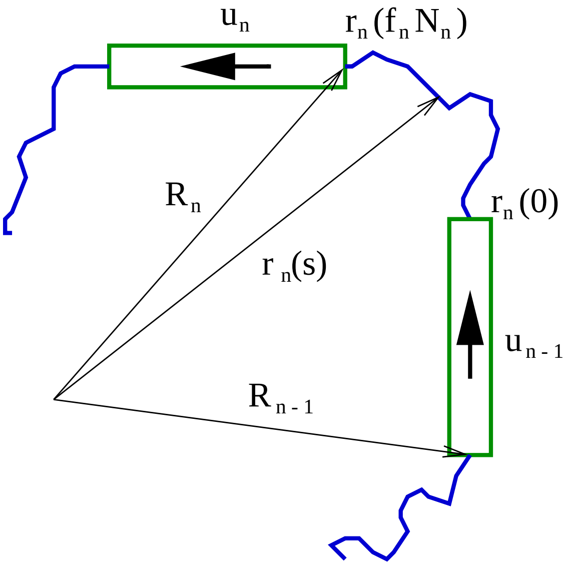

Figure 6.2: Rod-coil multiblock copolymer parameterisation. Two successive rod-coil blocks with numbers $n-1$ and n are shown. The flexible chain coordinates use the vector set $\mathbf{r}(s)$. The orientation of the n^{th} rod is denoted $\mathbf{u}_n$ and the junction point between rod and coil is given by $\mathbf{R}_n$.

$$\hat{\rho}_{\mathrm{C}}(\mathbf{r}) = \sum_{n=0}^{K} \int_{0}^{f_n N_n} \mathrm{d}s\, \delta(\mathbf{r} - \mathbf{r}_n(s)), \tag{6.5}$$

$$\hat{\rho}_{\mathrm{R}}(\mathbf{r}) = \sum_{n=0}^{K} \int_{0}^{(1-f_n)N_n} \mathrm{d}s\, \delta(\mathbf{r} - \mathbf{R}_n - \mathbf{u}_n s b). \tag{6.6}$$

The interaction part of the hamiltonian should allow for two- and three-body excluded volume point interactions between flexible and stiff segments, including cross-terms. The interaction constants v and w control their strength. To model selective solvent conditions an additional two-body interaction between the stiff segments only is introduced. Its strength is controlled by the interaction constant χ. Making use of the microscopic segment densities defined in Eqs.(6.5, 6.6), $H_{\text{int}}^{\text{iso}}$ can be written as

$$\begin{aligned}\beta H_{\text{int}}^{\text{iso}}\left[\hat{\rho}_{\text{C}},\hat{\rho}_{\text{R}}\right] &= \chi\int \mathrm{d}^3r\,\hat{\rho}_R(\mathbf{r})\hat{\rho}_R(\mathbf{r}) + \frac{v}{2}\int \mathrm{d}^3r\,\left[\hat{\rho}_C(\mathbf{r})+\hat{\rho}_R(\mathbf{r})\right]^2 \\ &+ \frac{w}{3!}\int \mathrm{d}^3r\,\left[\hat{\rho}_C(\mathbf{r})+\hat{\rho}_R(\mathbf{r})\right]^3. \end{aligned} \tag{6.7}$$

The superscript 'iso' denotes isotropic (not orientation dependent) interactions. In Chapter 9 it will be shown that this set of isotropic point interactions is enough to drive the system into a liquid-crystalline globular phase showing nematic order of the rods. It is nevertheless of interest to include an explicit alignment interaction between the rods to study its influence on the transition between an isotropic (disordered) globular phase and a liquid-crystalline globular phase. In order to construct such an interaction, the microscopic orientation density $\hat{S}^{ij}(\mathbf{r})$ is introduced [51].

$$\hat{S}^{ij}(\mathbf{r}) = \sum_{n=0}^{K}\int_0^{(1-f_n)N_n} \mathrm{d}s\,\delta(\mathbf{r}-\mathbf{R}_n-\mathbf{u}_n sb)\left[u^i u^j - \frac{1}{3}\delta^{ij}\right]. \tag{6.8}$$

The microscopic orientation density is sensitive to the collective orientation of the rods [66]. For the interaction sensitive term in the microscopic orientation density the standard second Legendre polynomial approximation is used. The rod-rod alignment interaction is chosen to be of the Maier-Saupe form [66, 67].

$$\begin{aligned} g\int \mathrm{d}^3r\,\mathrm{Tr}\left[\hat{S}^{ij}(\mathbf{r})\hat{S}^{ij}(\mathbf{r})\right] &= g\frac{2}{3}\sum_{n,m}\int \mathrm{d}s\mathrm{d}s'\,\delta\left(\mathbf{R}_n+\mathbf{u}_n sb-\mathbf{R}_m-\mathbf{u}_m s'b\right) \\ &\times P_2(\cos\hat{\theta}_{nm}), \end{aligned} \tag{6.9}$$

where $P_2(\cos\hat{\theta}_{nm}) = (3\cos^2\hat{\theta}_{nm}-1)/2$ is the second Legendre polynomial and $\hat{\theta}_{nm}$ stands for the angle between rod n and rod m. The interaction constant g controls the strength of the alignment interaction. The total interaction Hamiltonian is thus given by

$$\beta H_{\text{int}} = \beta H_{\text{int}}^{\text{iso}} + g\int \mathrm{d}^3r\,\mathrm{Tr}\left[\hat{S}^{ij}(\mathbf{r})\hat{S}^{ij}(\mathbf{r})\right]. \tag{6.10}$$

The canonical partition function of the entire system can now be constructed.

$$
\begin{aligned}
Z(\{N_n\},K) &= \int \prod_{n=1}^{K} \mathcal{D}\mathbf{r}_n(s)\mathrm{d}^3R_n\mathrm{d}^2u_n\,\delta(|\mathbf{u}_n|-1)\delta(\mathbf{r}_n(f_nN_n)-\mathbf{R}_n) \\
&\times \exp\left\{-\frac{3}{2b^2}\int\limits_0^{f_nN_n}\mathrm{d}s\left(\frac{\partial\mathbf{r}_n}{\partial s}\right)^2-\beta H_{\mathrm{int}}\right\}, \qquad (6.11)
\end{aligned}
$$

where for each rod-coil block the integration is over all continuous curves $\mathbf{r}_n(s)$, all rod-coil junction points $\mathbf{R}_n$ and all orientations of the rod $\mathbf{u}_n$. The first term in the exponential is responsible for the connectivity of each flexible chain, compare Chapter 2. The first delta function takes care of the constraint for the tangent vector of the rods to be a unit vector and the second delta function ensures that the junction between each rod and flexible chain is located at the end point of the chain. Hence Eq.(6.11) describes a multiblock rod-coil copolymer composed of K rod-coil units with interactions as described above. The n^{th} coil has the contour length f_nN_nb and the n^{th} rod the length $(1-f_n)N_nb$. However, to allow for a variable composition of stiff and flexible segments, this fixed sequence of rods and coils of specific length has to be released. This can be done by switching from the canonical description to a grand canonical description.

6.3. Grand canonical description and field theoretical representation

The composition of the system is assumed to be equilibrated with respect to the total number of stiff segments N_{R} and flexible segments N_{C}. Therefore the description of the composition can be reduced to

$$
\{N_n\},K \rightarrow N_{\mathrm{R}},N_{\mathrm{C}},N_{\mathrm{J}}, \qquad (6.12)
$$

where N_{J} is the number of junction points between rod and coil given by $N_{\mathrm{J}}=2K$. To switch to a grand canonical description, it is necessary to introduce chemical potentials: μ_{C} conjugated to the number of flexible segments N_{C}, μ_{R} conjugated to the number of stiff segments N_{R} and μ_{J} conjugated to the number of junctions N_{J}. An energy gain ϵ per stiff segments compared to a flexible one is introduced. In the case of a polypeptide, where the stiff segments are formed by a coil-helix transition, it corresponds to the energy gain due to the formation of hydrogen bonds. The chemical potential μ_{R} can thus be written as

$$
\mu_{\mathrm{R}}=\mu-\epsilon, \qquad (6.13)
$$

where $\mu \equiv \mu_\mathrm{C}$. Instead of the chemical potential μ_J it is convenient to use the fugacity σ defined by

$$\sigma = e^{-2\beta\mu_\mathrm{J}}. \tag{6.14}$$

The parameters ϵ and σ are equivalent to the ones used by Zimm and Bragg [55], see also section 6.1. Note, that it is not necessary to introduce an entropy loss ΔS associated with the formation of a stiff segment by hand as in the Zimm-Bragg model, since in the three dimensional description the difference of coil- and rod-entropy is explicitely incorporated.

Formally, the grand canonical partition function is then given by

$$Z(\mu,\epsilon,\sigma) = \sum_{N_\mathrm{C},N_\mathrm{R},N_\mathrm{J}=0}^{\infty} Z(N_\mathrm{R},N_\mathrm{C},N_\mathrm{J})e^{-\beta\mu N_\mathrm{C}}e^{-\beta(\mu-\epsilon)N_\mathrm{R}}\sigma^{N_\mathrm{J}/2}. \tag{6.15}$$

The grand canonical partition function can be represented in terms of an n-component field theory in the limit $n \to 0$ [12, 47, 48]. A detailed derivation of the field theoretical representation is given in Appendix A. Here only the result for the partition function is given Two n-component vector fields are needed for the field theoretic representation of the system. The vector field $\varphi_\alpha(\mathbf{r})$ is associated with the flexible segments and $\psi_\alpha(\mathbf{r},\mathbf{u})$ is associated with the stiff segments. The grand canonical partition function in the field theoretic representation reads

$$\begin{aligned}
Z(\mu,\epsilon,\sigma) &= \lim_{n\to 0}\prod_{\alpha=1}^{n}\int \mathcal{D}\psi_\alpha\mathcal{D}\varphi_\alpha \left[\int \mathrm{d}^3r\,\mathrm{d}^2u\,\psi_1(\mathbf{r},\mathbf{u})\right]\left[\int \mathrm{d}^3r'\,\varphi_1(\mathbf{r}')\right] \\
&\times \exp\left\{-\frac{1}{2}\sum_{\alpha=1}^{n}\int \mathrm{d}^3r\,\mathrm{d}^2u\,\psi_\alpha(\mathbf{r},\mathbf{u})\left[\beta(\mu-\epsilon) - \frac{b^2\left(\mathbf{u}\cdot\nabla_r\right)^2}{\beta(\mu-\epsilon)}\right]\psi_\alpha(\mathbf{r},\mathbf{u})\right. \\
&- \frac{1}{2}\sum_{\alpha=1}^{n}\int \mathrm{d}^3r\varphi_\alpha(\mathbf{r})\left[\beta\mu - \frac{b^2}{6}\nabla_r^2\right]\varphi_\alpha(\mathbf{r}) \\
&- \frac{\chi}{4}\int \mathrm{d}^3r\left[\sum_{\alpha=1}^{n}\int \mathrm{d}^2u\,\psi_\alpha^2(\mathbf{r},\mathbf{u})\right]^2 \\
&- \frac{v}{8}\int \mathrm{d}^3r\left[\sum_{\alpha=1}^{n}\int \mathrm{d}^2u\,\psi_\alpha^2(\mathbf{r},\mathbf{u}) + \sum_{\alpha'=1}^{n}\varphi_{\alpha'}^2(\mathbf{r})\right]^2
\end{aligned} \tag{6.16}$$

$$
\begin{aligned}
&- \frac{w}{48}\int \mathrm{d}^3r \left[\sum_{\alpha=1}^{n}\int \mathrm{d}^2u\, \psi_\alpha^2(\mathbf{r},\mathbf{u}) + \sum_{\alpha'=1}^{n}\varphi_{\alpha'}^2(\mathbf{r})\right]^3 \\
&+ \sigma^{1/2}\sum_{\alpha=1}^{n}\int \mathrm{d}^3r\,\mathrm{d}^2u\,\psi_\alpha(\mathbf{r},\mathbf{u})\varphi_\alpha(\mathbf{r}) \\
&- \frac{g}{4}\sum_{\alpha=1}^{n}\sum_{\alpha'=1}^{n}\int \mathrm{d}^3r\,\mathrm{d}^2u\,\mathrm{d}^2u'\,P_2(\mathbf{u}\cdot\mathbf{u}')\,\psi_\alpha^2(\mathbf{r},\mathbf{u})\,\psi_{\alpha'}^2(\mathbf{r},\mathbf{u}')\Bigg\}, \qquad (6.16)
\end{aligned}
$$

where the second Legendre polynomial is given by

$$
P_2(\mathbf{u}\cdot\mathbf{u}') = \frac{1}{2}\left(3\cos^2\theta - 1\right) \qquad (6.17)
$$

and θ denotes the angle between the two unit vectors $\mathbf{u}$ and $\mathbf{u}'$.

This partition cannot be evaluated easily and thus an appropriate approximation is needed. The method chosen here is the self-consistent field approximation [8]. In the self-consistent field approximation fluctuations are neglected and the functional integral over the fields in Eq.(6.16) is integrated by steepest descent. This leads to an effective saddle point grand potential which has to be minimised with respect to the fields. A short remark regarding the validity of this approximation is necessary. In a rather dense system, like a polymer globule in poor solvent, fluctuations are not important and can therefore safely be neglected. On the hand, in a very open system of low density, like a swollen polymer chain in good solvent, fluctuations play a major role and cannot be neglected. The self-consistent field method works good to describe a polymer from the dense globular state up to the transition point between globule and coil. The coil state of low density cannot be described properly by this method.

The saddle point solutions for $\varphi_\alpha(\mathbf{r})$ and $\psi_\alpha(\mathbf{r},\mathbf{u})$ are chosen such that the effective grand potential keeps the full symmetry of the hamiltonian in replica space, i.e. it is invariant under rotations in replica space. This is the case for

$$
\begin{aligned}
\psi_\alpha(\mathbf{r},\mathbf{u}) &= n_\alpha\psi(\mathbf{r},\mathbf{u}) \\
\varphi_\alpha(\mathbf{r}) &= n_\alpha\varphi(\mathbf{r}), \qquad (6.18)
\end{aligned}
$$

where $\mathbf{n}$ is a unit vector such that $\sum_{\alpha=1}^{n} n_\alpha^2 = 1$. After the saddle point integration of the partition function the effective grand potential then reads

$$
\begin{aligned}
\beta\Omega(\mu,\epsilon,\sigma) &= \frac{1}{2}\int \mathrm{d}^3r\,\mathrm{d}^2u\,\left[\beta(\mu-\epsilon)\psi^2(\mathbf{r},\mathbf{u})+\frac{b^2[\mathbf{u}\cdot\nabla_r\psi(\mathbf{r},\mathbf{u})]^2}{\beta(\mu-\epsilon)}\right]\\
&+ \frac{1}{2}\int \mathrm{d}^3r\,\left[\beta\mu\varphi^2(\mathbf{r})+\frac{b^2}{6}[\nabla_r\varphi(\mathbf{r})]^2\right]\\
&+ \frac{\chi}{4}\int \mathrm{d}^3r\left[\int \mathrm{d}^2u\,\psi^2(\mathbf{r},\mathbf{u})\right]^2\\
&+ \frac{v}{8}\int \mathrm{d}^3r\left[\int \mathrm{d}^2u\,\psi^2(\mathbf{r},\mathbf{u})+\varphi^2(\mathbf{r})\right]^2\\
&+ \frac{w}{48}\int \mathrm{d}^3r\left[\int \mathrm{d}^2u\,\psi^2(\mathbf{r},\mathbf{u})+\varphi^2(\mathbf{r})\right]^3\\
&- \sigma^{1/2}\int \mathrm{d}^3r\,\mathrm{d}^2u\,\psi(\mathbf{r},\mathbf{u})\varphi(\mathbf{r})\\
&+ \frac{g}{4}\int \mathrm{d}^3r\,\mathrm{d}^2u\,\mathrm{d}^2u'\,P_2(\mathbf{u}\cdot\mathbf{u}')\,\psi^2(\mathbf{r},\mathbf{u})\,\psi^2(\mathbf{r},\mathbf{u}'). \qquad (6.19)
\end{aligned}
$$

The rod and coil densities as well as the orientation density are given by the following relations

$$
\begin{aligned}
\rho_\mathrm{C}(\mathbf{r}) &= \frac{1}{2}\varphi^2(\mathbf{r})\\
\rho_\mathrm{R}(\mathbf{r}) &= \frac{1}{2}\int \mathrm{d}^2u\,\psi^2(\mathbf{r},\mathbf{u})\\
S^{ij}(\mathbf{r}) &= \frac{1}{2}\int \mathrm{d}^2u\,\left(u^iu^j-\frac{1}{3}\delta^{ij}\right)\psi^2(\mathbf{r},\mathbf{u}). \qquad (6.20)
\end{aligned}
$$

The equilibrium number of stiff and of flexible segments is then given by

$$
N_\mathrm{rod} = \frac{1}{2}\int \mathrm{d}^3r\mathrm{d}^2u\,\psi^2(\mathbf{r},\mathbf{u}) \qquad (6.21)
$$

and

$$
N_\mathrm{coil} = \frac{1}{2}\int \mathrm{d}^3r\,\varphi^2(\mathbf{r}), \qquad (6.22)
$$

respectively.

The effective grand potential in Eq.(6.19) has to be minimised with respect to the fields to obtain the set of equations which determines the self-consistent fields. This functional minimisation leads to a set of highly nonlinear integro-differential equations which are difficult to deal with, even numerically.

$$\begin{aligned}
&\left[\beta(\mu-\epsilon)-\frac{b^2(\mathbf{u}\cdot\nabla_r)^2}{\beta(\mu-\epsilon)}\right]\psi(\mathbf{r},\mathbf{u})-\sigma^{1/2}\varphi(\mathbf{r})\\
&\quad+\chi\psi(\mathbf{r},\mathbf{u})\int \mathrm{d}^2u'\,\psi^2(\mathbf{r},\mathbf{u}')+\frac{v}{2}\,\psi(\mathbf{r},\mathbf{u})\left[\int \mathrm{d}^2u'\,\psi^2(\mathbf{r},\mathbf{u}')+\varphi^2(\mathbf{r})\right]\\
&\quad+\frac{w}{8}\,\psi(\mathbf{r},\mathbf{u})\left[\int \mathrm{d}^2u'\,\psi^2(\mathbf{r},\mathbf{u}')+\varphi^2(\mathbf{r})\right]^2\\
&\quad+g\,\psi(\mathbf{r},\mathbf{u})\int \mathrm{d}^2u'\,P_2(\mathbf{u}\cdot\mathbf{u}')\,\psi^2(\mathbf{r},\mathbf{u}')=0
\end{aligned}\tag{6.23}$$

and

$$\begin{aligned}
&\left[\beta\mu-\frac{b^2}{6}\nabla_r^2\right]\varphi(\mathbf{r})-\sigma^{1/2}\int \mathrm{d}^2u'\,\psi(\mathbf{r},\mathbf{u}')\\
&\quad+\frac{v}{2}\,\varphi(\mathbf{r})\left[\int \mathrm{d}^2u'\,\psi^2(\mathbf{r},\mathbf{u}')+\varphi^2(\mathbf{r})\right]\\
&\quad+\frac{w}{8}\,\varphi(\mathbf{r})\left[\int \mathrm{d}^2u'\,\psi^2(\mathbf{r},\mathbf{u}')+\varphi^2(\mathbf{r})\right]^2=0.
\end{aligned}\tag{6.24}$$

The main difficulties arise from the remaining integrals over the orientation $\mathbf{u}'$. To avoid this integration the following approximation is used. The field $\psi(\mathbf{r},\mathbf{u})$ can be expanded in terms of spherical harmonics. As can be seen from the $\psi(\mathbf{u}\cdot\nabla_r)^2\psi$-term (first term in the exponential) in Eq.(6.16), the rods do not have a chirality, see also Appendix A. The solutions for $\varphi(\mathbf{r})$ and $\psi(\mathbf{r},\mathbf{u})$ must therefore respect uniaxial and cylindrical symmetry and the expansion of $\psi(\mathbf{r},\mathbf{u})$ reduces to Legendre polynomials. This expansion and the calculation of the corresponding effective grand potential and the set of equations for the self-consistent fields are presented in the following section.

6.4. Expansion in terms of Legendre polynomials

In order to simplify the effective grand potential given by Eq.(6.19), $\psi(\mathbf{r},\mathbf{u})$ is expanded in spherical harmonics. This expansion has the form [50]

$$\psi(\mathbf{r},\mathbf{u})=\sum_{l,m}\psi_{lm}(\mathbf{r})Y_{lm}(\mathbf{u}).\tag{6.25}$$

Since the solution for $\psi(\mathbf{r},\mathbf{u})$ must respect uniaxial and cylindrical symmetry, the expansion reduces to Legendre polynomials, i.e. $m \equiv 0$.

$$\psi(\mathbf{r},\mathbf{u}) = \sum_{l} \psi_l(\mathbf{r}) P_l(\mathbf{u}\cdot\mathbf{n}), \tag{6.26}$$

where $\mathbf{n}$ is the main direction along which the rods in the core of the globule are aligned, if the system forms an anisotropic globule with aligned rods. If they are not aligned and the system forms an disordered globule, only the first term in the expansion ($l = 0$) differs from zero.

The main direction of alignment $\mathbf{n}$ can be chosen arbitrarily without loss of generality, since a change in alignment direction only corresponds to a rotation of the complete globule in the laboratory coordinate frame. Here the z-axis of the (x, y, z) laboratory frame is chosen, i.e. $\mathbf{n} = \mathbf{n}_z$.

As a further simplification, the expansion in Eq.(6.26) is truncated at lowest non-trivial order

$$\psi(\mathbf{r},\mathbf{u}) \approx \left(\frac{1}{4\pi}\right)^{1/2} \psi_0(\mathbf{r}) + \left(\frac{5}{4\pi}\right)^{1/2} \psi_2(\mathbf{r}) P_2(\mathbf{u}\cdot\mathbf{n}_z). \tag{6.27}$$

This is a rather severe approximation, but it makes it possible to tackle the problem numerically, since the set of two integro-differential equations in $\mathbf{r}$ and $\mathbf{u}$ given by Eqs.(6.23, 6.24) reduces to three partial differential equations in $\mathbf{r}$, see Eqs.(6.35, 6.36, 6.37) below. Furthermore, the truncation is not expected to change the results qualitatively. For future considerations it would nevertheless be of interest to try to develop a numerical routine which can solve the full integro-differential equations.

From Eq.(6.20) and Eq.(6.27) the rod density can be calculated in terms of $\psi_0(\mathbf{r})$ and $\psi_2(\mathbf{r})$. It is given by

$$\rho_{\mathrm{R}}(\mathbf{r}) \approx \frac{1}{2}\left[\psi_0^2(\mathbf{r}) + \psi_2^2(\mathbf{r})\right]. \tag{6.28}$$

After choosing $\mathbf{n}_z$ as the alignment direction, the orientation density $S^{ij}(\mathbf{r})$ - see Eq.(6.20) reduces to

$$\begin{aligned} S(\mathbf{r}) \equiv S^{zz}(\mathbf{r}) &= \frac{1}{3}\int \mathrm{d}^2u\, P_2(\cos\theta)\psi^2(\mathbf{r},\mathbf{u}) \\ &\approx \frac{2}{\sqrt{5}}\,\psi_2(\mathbf{r})\left[\psi_0(\mathbf{r}) + \sqrt{5}\psi_2(\mathbf{r})\right]. \end{aligned} \tag{6.29}$$

To measure the orientational order of the entire system a nematic order parameter S is defined as follows

$$S = \frac{1}{N}\int \mathrm{d}^3r\, S(\mathbf{r}). \tag{6.30}$$

Substitution of Eq.(6.27) in Eq.(6.19) makes it possible to perform the **u**-integrations. To perform the **u**- and **u**′-integrations in the alignment interaction term in Eq.(6.19) the following addition theorem is used [50]

$$P_2(\mathbf{u}\cdot\mathbf{u}') = P_2(\cos\gamma) = \left(\frac{4\pi}{5}\right)\sum_{m=-2}^{2} Y^*_{2m}(\mathbf{u})Y_{2m}(\mathbf{u}'). \tag{6.31}$$

$\psi(\mathbf{r},\mathbf{u})$ and $\psi(\mathbf{r},\mathbf{u}')$ do not depend on the azimuthal angles ϕ and ϕ' respectively. Therefore the only term which survives after integrations over ϕ and ϕ' corresponds to $m = 0$ and leads to the factorisation of the alignment interaction term in Eq.(6.19).

The straightforward **u**-integrations in the other terms in Eq.(6.19) yields the following expression for the effective grand potential in terms of $\psi_0(\mathbf{r})$, $\psi_2(\mathbf{r})$ and $\varphi(\mathbf{r})$

$$\begin{aligned}
\beta\Omega(\mu,\epsilon,\sigma) &= \frac{\beta(\mu-\epsilon)}{2}\int \mathrm{d}^3r\,\left[\psi_0^2(\mathbf{r})+\psi_2^2(\mathbf{r})\right] \\
&- \frac{b^2}{210\,\beta\,(\mu-\epsilon)}\int \mathrm{d}^3r\Big\{35\,\psi_0(\mathbf{r})\nabla_r^2\psi_0(\mathbf{r}) \\
&+ 14\sqrt{5}\,\psi_0(\mathbf{r})\Big[2\,\partial_z^2-\partial_x^2-\partial_y^2\Big]\psi_2(\mathbf{r}) \\
&+ \psi_2(\mathbf{r})\Big[25\,\partial_x^2+25\,\partial_y^2+55\,\partial_z^2\Big]\psi_2(\mathbf{r})\Big\} \\
&+ \frac{1}{2}\int \mathrm{d}^3r\,\varphi(\mathbf{r})\Big[\beta\mu-\frac{b^2}{6}\nabla_r^2\Big]\varphi(\mathbf{r}) \\
&+ \frac{\chi}{4}\int \mathrm{d}^3r\,\left[\psi_0^2(\mathbf{r})+\psi_2^2(\mathbf{r})\right]^2 \\
&+ \frac{v}{8}\int \mathrm{d}^3r\,\left[\varphi^2(\mathbf{r})+\psi_0^2(\mathbf{r})+\psi_2^2(\mathbf{r})\right]^2 \\
&+ \frac{w}{48}\int \mathrm{d}^3r\,\left[\varphi^2(\mathbf{r})+\psi_0^2(\mathbf{r})+\psi_2^2(\mathbf{r})\right]^3 \\
&- 2\sqrt{\pi\sigma}\int \mathrm{d}^3r\,\varphi(\mathbf{r})\,\psi_0(\mathbf{r}) \\
&+ \frac{g}{245}\int \mathrm{d}^3r\,\Big\{\,\psi_2(\mathbf{r})\,\Big[7\,\psi_0(\mathbf{r})+\sqrt{5}\,\psi_2(\mathbf{r})\Big]\Big\}^2 .
\end{aligned} \tag{6.32}$$

The above equation should now be minimised with respect to $\psi_0(\mathbf{r})$, $\psi_2(\mathbf{r})$ and $\varphi(\mathbf{r})$ to obtain the set of differential equations for the three fields.

As already mentioned the fields $\varphi(\mathbf{r}), \psi_0(\mathbf{r})$ and $\psi_2(\mathbf{r})$ are symmetric with respect to rotations within the xy-plane. Hence it is convenient to switch to cylindrical coordinates

$$\{x,y,z\}\rightarrow\{\varrho,z\}, \tag{6.33}$$

where $\varrho = (x^2 + y^2 + z^2)^{1/2}$.

The grand potential $\Omega(\mu, \epsilon, \sigma)$ then reads

$$\begin{aligned}
\beta\Omega(\mu,\epsilon,\sigma) &= \frac{\beta\,(\mu-\epsilon)}{2}\,2\pi\int_0^\infty \mathrm{d}\varrho\,\varrho\int_{-\infty}^{\infty}\mathrm{d}z\ \left[\psi_0^2(\varrho,z)+\psi_2^2(\varrho,z)\right] \\
&- \frac{b^2}{210\,\beta\,(\mu-\epsilon)}\,2\pi\int_0^\infty \mathrm{d}\varrho\,\varrho\int_{-\infty}^{\infty}\mathrm{d}z\,\Big\{35\,\psi_0(\varrho,z)\nabla_r^2\psi_0(\varrho,z) \\
&+ 14\sqrt{5}\,\psi_0(\varrho,z)\Big[3\,\partial_z^2-\nabla_r^2\Big]\psi_2(\varrho,z) \\
&+ \psi_2(\varrho,z)\Big[25\,\nabla_r^2+30\,\partial_z^2\Big]\psi_2(\varrho,z)\Big\} \\
&+ \frac{1}{2}\,2\pi\int_0^\infty \mathrm{d}\varrho\,\varrho\int_{-\infty}^{\infty}\mathrm{d}z\ \varphi(\varrho,z)\Big[\beta\mu-\frac{b^2}{6}\nabla_r^2\Big]\varphi(\varrho,z) \\
&+ \frac{\chi}{4}\,2\pi\int_0^\infty \mathrm{d}\varrho\,\varrho\int_{-\infty}^{\infty}\mathrm{d}z\ \left[\psi_0^2(\varrho,z)+\psi_2^2(\varrho,z)\right]^2 \\
&+ \frac{v}{8}\,2\pi\int_0^\infty \mathrm{d}\varrho\,\varrho\int_{-\infty}^{\infty}\mathrm{d}z\ \left[\varphi^2(\varrho,z)+\psi_0^2(\varrho,z)+\psi_2^2(\varrho,z)\right]^2 \\
&+ \frac{w}{48}\,2\pi\int_0^\infty \mathrm{d}\varrho\,\varrho\int_{-\infty}^{\infty}\mathrm{d}z\ \left[\varphi^2(\varrho,z)+\psi_0^2(\varrho,z)+\psi_2^2(\varrho,z)\right]^3 \\
&- \sqrt{4\pi\sigma}\,2\pi\int_0^\infty \mathrm{d}\varrho\,\varrho\int_{-\infty}^{\infty}\mathrm{d}z\ \varphi(\varrho,z)\,\psi_0(\varrho,z) \\
&+ \frac{g}{245}\,2\pi\int_0^\infty \mathrm{d}\varrho\,\varrho\int_{-\infty}^{\infty}\mathrm{d}z\ \Big\{\psi_2(\varrho,z)\ \Big[7\,\psi_0(\varrho,z)+\sqrt{5}\,\psi_2(\varrho,z)\Big]\Big\}^2,
\end{aligned} \tag{6.34}$$

where the Laplace operator in cylindrical coordinates is given by $\nabla_r^2 = \partial_\varrho^2 + \frac{1}{\varrho}\partial_\varrho + \partial_z^2$. Functional minimisation of Eq.(6.34) with respect to $\varphi(\varrho,z), \psi_0(\varrho,z)$ and $\psi_2(\varrho,z)$ gives the following set of equations

$$\begin{aligned}
&-\frac{b^2}{6}\nabla_r^2\varphi(\varrho,z)+\beta\mu\varphi(\varrho,z)-\sqrt{4\pi\sigma}\psi_0(\varrho,z) \\
&\quad+\frac{v}{2}\varphi(\varrho,z)\left[\varphi^2(\varrho,z)+\psi_0^2(\varrho,z)+\psi_2^2(\varrho,z)\right] \\
&\quad+\frac{w}{8}\varphi(\varrho,z)\left[\varphi^2(\varrho,z)+\psi_0^2(\varrho,z)+\psi_2^2(\varrho,z)\right]^2=0,
\end{aligned} \tag{6.35}$$

$$\begin{aligned}
&\frac{b^2}{\beta(\mu-\epsilon)}\left\{-\frac{1}{3}\nabla_r^2\psi_0(\varrho,z)-\frac{\sqrt{5}}{15}\left[3\,\partial_z^2\psi_2(\varrho,z)-\nabla_r^2\psi_2(\varrho,z)\right]\right\}\\
&\quad+\beta(\mu-\epsilon)\psi_0(\varrho,z)-\sqrt{4\pi\sigma}\varphi(\varrho,z)\\
&\quad+\chi\psi_0(\varrho,z)\left[\psi_0^2(\varrho,z)+\psi_2^2(\varrho,z)\right]\\
&\quad+\frac{v}{2}\psi_0(\varrho,z)\left[\varphi^2(\varrho,z)+\psi_0^2(\varrho,z)+\psi_2^2(\varrho,z)\right]\\
&\quad+\frac{w}{8}\psi_0(\varrho,z)\left[\varphi^2(\varrho,z)+\psi_0^2(\varrho,z)+\psi_2^2(\varrho,z)\right]^2\\
&\quad+\frac{14g}{245}\left[7\psi_0(\varrho,z)+\sqrt{5}\psi_2(\varrho,z)\right]\psi_2^2(\varrho,z)=0
\end{aligned}\tag{6.36}$$

and

$$\begin{aligned}
&\frac{b^2}{\beta\,(\mu-\epsilon)}\left\{-\frac{5}{21}\nabla_r^2\psi_2(\varrho,z)-\frac{6}{21}\partial_z^2\psi_2(\varrho,z)-\frac{\sqrt{5}}{15}\left[3\,\partial_z^2\psi_0(\varrho,z)-\nabla_r^2\psi_0(\varrho,z)\right]\right\}\\
&\quad+\beta(\mu-\epsilon)\psi_2(\varrho,z)+\chi\psi_2(\varrho,z)\left[\psi_0^2(\varrho,z)+\psi_2^2(\varrho,z)\right]\\
&\quad+\frac{v}{2}\psi_2(\varrho,z)\left[\varphi^2(\varrho,z)+\psi_0^2(\varrho,z)+\psi_2^2(\varrho,z)\right]\\
&\quad+\frac{w}{8}\psi_2(\varrho,z)\left[\varphi^2(\varrho,z)+\psi_0^2(\varrho,z)+\psi_2^2(\varrho,z)\right]^2\\
&\quad+\frac{2g}{245}\psi_2(\varrho,z)\left[7\psi_0(\varrho,z)+\sqrt{5}\psi_2(\varrho,z)\right]\left[7\psi_0(\varrho,z)+2\sqrt{5}\psi_2(\varrho,z)\right]=0
\end{aligned}\tag{6.37}$$

This is now a set of three differential equations for the three self-consistent fields $\varphi(\mathbf{r})$, $\psi_0(\mathbf{r})$ and $\psi_2(\mathbf{r})$ instead of the two integro-differential equations for $\psi(\mathbf{r}$ and $\varphi(\mathbf{r},\mathbf{u})$ given by Eqs.(6.23, 6.24). The three differential equations must be supplemented by the following boundary conditions

$$\begin{array}{rcl}
\varphi(\varrho\to\infty) &=& \psi_0(\varrho\to\infty)=\psi_2(\varrho\to\infty)=0,\\
\varphi(\varrho\to\infty) &=& \psi_0(z\to\infty)=\psi_2(z\to\infty)=0,\\
\left.\frac{\partial}{\partial\varrho}\varphi(\varrho,)\right|_\infty &=& \left.\frac{\partial}{\partial\varrho}\psi_0(\varrho)\right|_\infty=\left.\frac{\partial}{\partial\varrho}\psi_2(\varrho)\right|_\infty=0,\\
\left.\frac{\partial}{\partial z}\varphi(z)\right|_\infty &=& \left.\frac{\partial}{\partial z}\psi_0(z)\right|_\infty=\left.\frac{\partial}{\partial z}\psi_2(z)\right|_\infty=0.
\end{array}\tag{6.38}$$

The total number of flexible and stiff segments (compare Eq.(6.22)) is now given by

$$N_{\text{coil}} = \pi\int_0^\infty \mathrm{d}\varrho\,\varrho\int_{-\infty}^\infty dz\,\varphi^2(\varrho,z)\tag{6.39}$$

and

$$N_{\mathrm{rod}} \;=\; \pi \int_0^\infty \mathrm{d}\varrho\, \varrho \int_{-\infty}^{\infty} dz\, \left[\psi_0^2(\varrho,z) + \psi_2^2(\varrho,z)\right], \tag{6.40}$$

respectively.

The three coupled partial differential equations given by Eqs.(6.35, 6.36, 6.37) can be solved numerically. This is done with the finite element tool kit Gascoigne [58]. A brief description of the numerical methods is given in Appendix B. In the following chapter some results for the coil-globule transition of a homopolymer are reestablished by setting ψ_0 and ψ_2 identically to zero.

In Chapter 8 the numerical solutions of the full set of equations are presented and discussed in detail.

7. Homopolymer globule

7.1. Differential equation for the self-consistent field

In this chapter the coil-globule transition of a fully flexible homopolymer is investigated as a test for the numerical routines.

After setting ψ equal to zero, Eq.(6.19) reduces to the effective free energy of a flexible homopolymer.

$$\begin{aligned}\beta F(\mu) &= \frac{1}{2}\int \mathrm{d}^3 r\, \varphi(\mathbf{r}) \left[\beta\mu - \frac{b^2}{6}\varphi(\mathbf{r})\nabla_r^2\right]\varphi(\mathbf{r}) \\ &+ \frac{v}{8}\int \mathrm{d}^3 r \varphi^4(\mathbf{r}) + \frac{w}{48}\int \mathrm{d}^3 r \varphi^6(\mathbf{r}).\end{aligned} \tag{7.1}$$

The saddle point free energy given by Eq.(7.1) is sufficient to describe a polymer from the dense globular state up to the transition point between globule and coil, see also Section 6.3.

Minimisation with respect to $\varphi(\mathbf{r})$ yields the differential equation which determines the self-consistent field

$$\left[\beta\mu - \frac{b^2}{6}\nabla_r^2\right]\varphi(\mathbf{r}) + \frac{v}{2}\,\varphi^3(\mathbf{r}) + \frac{w}{8}\varphi^5(\mathbf{r}) = 0. \tag{7.2}$$

Due to spherical symmetry, Eq.(7.2) can be simplified to

$$\left[\beta\mu - \frac{b^2}{6}\left(\partial_\varrho^2 + \frac{1}{\varrho}\partial_\varrho\right)\right]\varphi(\varrho) + \frac{v}{2}\,\varphi^3(\varrho) + \frac{w}{8}\varphi^5(\varrho) = 0. \tag{7.3}$$

The above differential equation has to be supplemented by the boundary conditions

$$\begin{aligned}\varphi(\varrho \to \infty) &= 0, \\ \frac{\partial}{\partial\varrho}\varphi(\varrho)\bigg|_\infty &= 0.\end{aligned} \tag{7.4}$$

The total number of segments N is given by

$$N = 2\pi \int_0^\infty \mathrm{d}\varrho\, \varrho^2 \varphi^2(\varrho). \tag{7.5}$$

In the following, the segment length b is chosen as the unit length scale of the system and therefore set to $b = 1$ for convenience. Thus, in the following, all lengths are given in units of b. The two-body interaction parameter v is given by $v = b^3\tau$, compare Eq.(2.16) in Section 2.2. For $b = 1$ it reduces to the reduced temperature τ. Since here the polymer is described in the dense globular state or up to the transition point between globule and coil, τ is always negative, i.e. the two-body interactions are always attractive.

7.2. Coil-globule transition

A polymer immersed in poor solvent adopts a dense globular state characterised by $R \sim N^{1/3}$, where R is the radius of the globule. In the limit of $N \to \infty$ the globule shows a phase transition to an ideal coil at the Θ temperature. The Θ temperature is characterised by a vanishing two-body interaction parameter. In reality, polymers are finite objects. The transition from globule to coil is therefore a finite-width crossover transition. This crossover transition occurs at finite $\tau = \tau_\mathrm{c}$ rather than $\tau = 0$. The critical reduced temperature τ_c is proportional to $N^{-1/2}$. This can be seen from a simple scaling consideration. Similar to Section 2.2 the free energy of the globule can approximately be written as

$$\beta F \simeq \frac{R^2}{N} + \tau \frac{N^2}{R^3} + w \frac{N^3}{R^6}. \tag{7.6}$$

The first and second term are the same as in Eq.(2.18). The last term is given by $w\bar{c}^3 R^3$. Note, that b is set to one and R is therefore given in units of b. Minimisation of the above equation with respect to R yields

$$\frac{R}{N} - \tau \frac{N^2}{R^4} - w \frac{N^3}{R^7} = 0, \tag{7.7}$$

where numerical prefactors have been omitted. At $\tau = \tau_\mathrm{c}$ the polymer chain is almost Gaussian, i.e. $R \sim N^{1/2}$. Substituting $N^{1/2}$ for R in Eq.(7.6) immediately yields

$$\tau_\mathrm{c} \sim w N^{-1/2}. \tag{7.8}$$

A similar scaling relation can be found for the density profile $\rho(\varrho)$. A homopolymer globule always adapts a spherically symmetric configuration. The set of coordinates therefore reduces to the radius ϱ of the globule, compare Eq.(7.3). The centre is located at $\varrho = 0$. At $\tau = \tau_\mathrm{c}$ the density profile has the following scaling form

$$\rho_\mathrm{c}(\varrho) \simeq N^\alpha g\left(\frac{\varrho}{R_c}\right), \tag{7.9}$$

where $R_c \sim N^{1/2}$. The integral over the density gives the total number of segments.

$$\begin{aligned} N = 4\pi \int_0^\infty \mathrm{d}\varrho\, \varrho^2 \rho_\mathrm{c}(\varrho) \simeq N^\alpha \int_0^\infty \mathrm{d}\varrho\, \varrho^2 g\left(\frac{\varrho}{R_c}\right) &= N^\alpha \int_0^\infty \mathrm{d}x\, x^2 R_c^3 g(x) \\ &\simeq N^{\alpha+3/2} \int_0^\infty \mathrm{d}x\, x^2 g(x), \end{aligned} \tag{7.10}$$

where $x = \varrho/R_c$. From Eq.(7.10) follows immediately $\alpha = -1/2$ and hence

$$\rho_\mathrm{c}(\varrho) \sim N^{-1/2}. \tag{7.11}$$

It should be possible to recover the above scaling relations over a wide range of chain lengths N from the numerical results.

7.3. Numerical results

In a grand canonical description the total size of the system - here the number of segments N - depends on the chemical potential μ and on all the interaction constants. Its mean value is determined by equilibrium conditions. The following plot shows the μ-dependence of N for the homopolymer as a result of the numerical solution of Eq.(7.3). The equilibrium value of N is calculated by performing the integration in Eq.(7.5). Fig.(7.1) shows that N diverges for $\mu \to 0$. This corresponds to the $N \sim \mu^{-1}$ behaviour of a quasi ideal chain in the Θ-regime [84]. The divergence of N at a specific value of μ on the right hand side of the minimum corresponds to a fully collapsed infinite globule [48]. The left branch of the $N(\mu)$-curve describes the quasi ideal chain (or open coil) behaviour and the right branch the behaviour of a globule. This suggests to identify the minimum of the $N(\mu)$-curve with the transition point between coil and globule. To test whether it is reasonable to define the minimum of $N(\mu)$ as the transition point, the minimum of N for different values of τ is calculated. Provided that the minimum corresponds to the transition point this should yield the critical τ for given N. If the definition is reasonable it should be possible to recover the scaling relation $\tau_\mathrm{c} \sim N^{-1/2}$. Fig. (7.2) shows indeed the correct scaling relation $\tau_\mathrm{c} \sim N^{-1/2}$ for the critical reduced temperature.

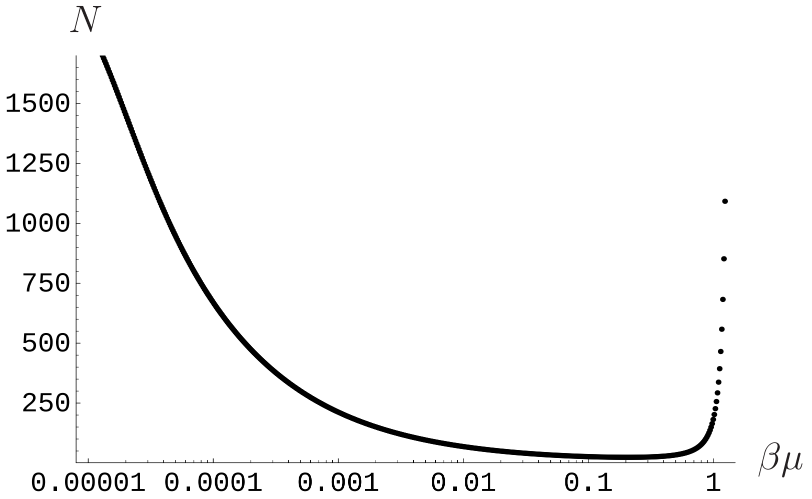

Figure 7.1: Dependence of the length of the polymer chain N on the chemical potential μ. The chosen parameters are: $v = \tau = 2$, $w = 1$. Note, that the μ-scale is logarithmic.

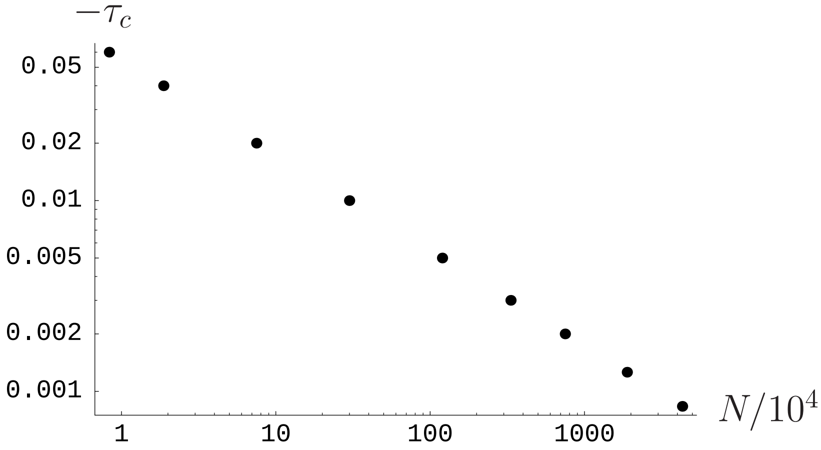

Figure 7.2: Log-log plot of the dependence of the critical reduced temperature τ_c on the chain length N. The three-body interaction parameter w is chosen to be 0.1 for all points. The slope is calculated by linear regression to be -0.500007.

The density profiles at $\tau = \tau_\mathrm{c}$ for different chain lengths are shown in Fig.(7.3). In all plots below w is chosen to be 0.1. Fig.(7.3) shows that the critical density profile becomes more and more peaked around its maximum value ρ_0 at the centre ($r = 0$) for shorter chains. This change in the shape of the density profile with increasing N can be explained by two other scaling relations from Section 2.2. At the transition point τ_c the size of the globule, described by its radius, should scale like a gaussian chain, i.e. $R_c \sim N^{1/2}$. The density of the globule $\rho(\varrho)$ on the other hand should

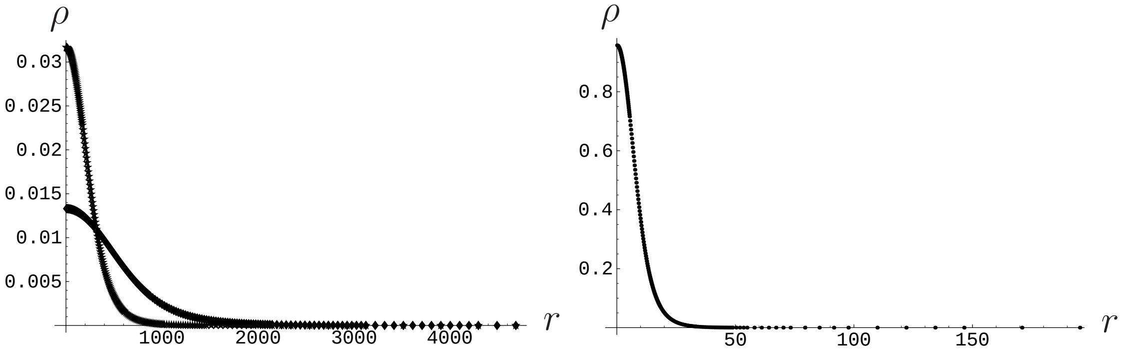

Figure 7.3: The left plot shows the radial density $\rho(\varrho)$ for $\tau_c = 2 \cdot 10^{-3}$, $N = 7.5 \cdot 10^6$ (upper curve) and $\tau_c = 8.3 \cdot 10^{-4}$, $N = 4.3 \cdot 10^7$ (lower curve). The right plot shows $\rho(\varrho)$ for $\tau_c = 0.06$ and $N = 832$.

scale as $\rho(\varrho) \sim \tau \sim N^{-1/2}$.

To test the scaling relation for R_c a reasonable definition for the critical radius from the numerical data has to be found. The point in the critical density profile at which the density decreased to $10^{-3}\,\rho_0$ is chosen as R_c. In Fig.(7.4) the critical globule radius is plotted as a function of chain length N. It shows the correct scaling relation $R_\mathrm{c} \sim N$.

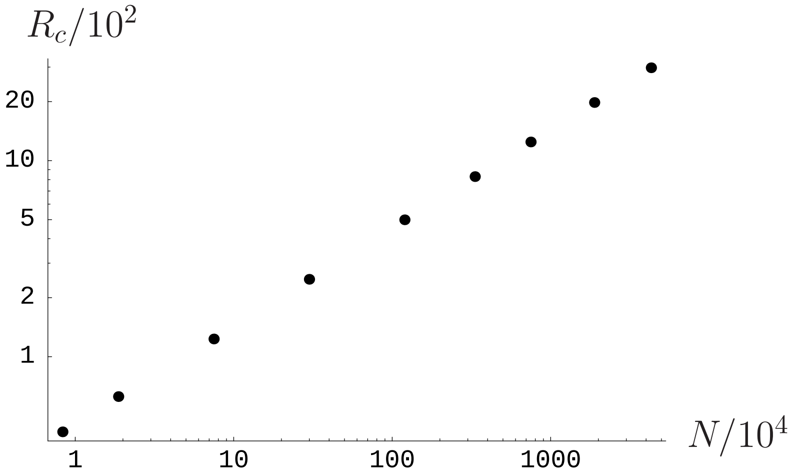

Figure 7.4: Log-log plot of critical globule radius R_c versus chain length N. The slope is calculated by linear regression to be 0.500188.

As a last test, in Fig.(7.5) the density maximium at the centre of the critical globule is plotted as a function of N. Since $\rho(\varrho) \sim N^{-1/2}$, the density maximum $\rho_0 = \rho(0)$ also scales as $N^{-1/2}$, which is in accordance with the numerical results shown in Fig.(7.5).

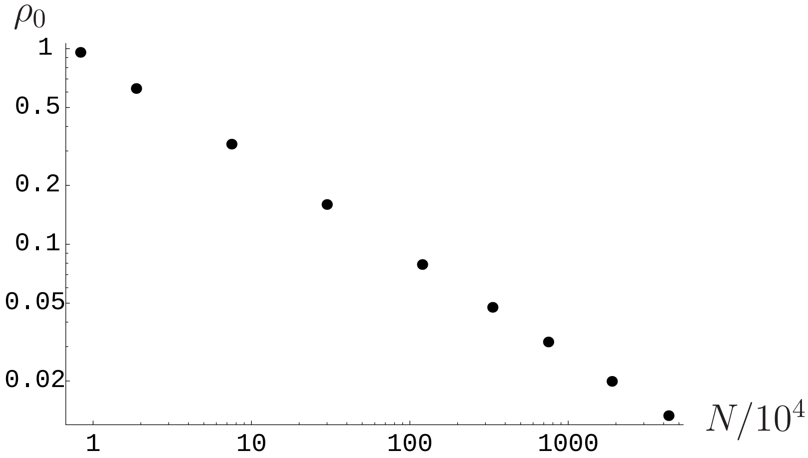

Figure 7.5: Log-log plot of the density maximum ρ_0 versus chain length N. The slope is calculated by linear regression to be -0.50044.

The plots in Figs.(7.2, 7.4, 7.5) show a very good agreement of the numerical results with the scaling relations predicted in Section 2.2 over almost four orders of magnitude for the chain length. It can therefore be assumed that the finite element toolkit Gascoigne is well suited to tackle the boundary value problem given by the differential equations for the self-consistent fields, Eqs.(6.35 - 6.37), and the corresponding boundary conditions, Eq.(6.38). In addition, they show that it is reasonable to define the minimum of the $N(\mu)$-curve as the transition point between coil and globule.

8. Results for the copolymer with variable composition

8.1. Introductory remarks

In this chapter the numerical results for the full set of equations describing a rod-coil multiblock copolymer with a variable composition of stiff and flexible segments are presented. The results are obtained by solving Eqs.(6.35-6.37) with the boundary conditions given by Eq.(6.38). The segment length is set to $b = 1$ as in the previous chapter. In addition, all energies such as ϵ, μ and also the saddle point free energy F are given in units of $k_{\mathrm{B}}T$. In this chapter this will not be indicated by multiplication with β in order to avoid complicated notation.

Eqs.(6.35-6.37) describe the copolymer in a grand-canonical representation. In the grand-canonical ensemble the total number of segments of the polymer N is not fixed but its mean value is determined by equilibrium conditions, see Section 7.3. A real polymer has a fixed length. In order to ensure this fixed length N, the chemical potential μ is - for each set of physical parameters $(v, w, \chi, g, \epsilon, \sigma)$ - tuned such that the equilibrium value of N is equal to the desired one. The total number of segments $N = N_{\mathrm{coil}} + N_{\mathrm{rod}}$ is calculated by performing the integrations in Eqs.(6.39, 6.40). For a given set of parameters, $N(\mu)$ can be computed and a typical example of this curve is shown in Fig.(8.1) - similar to the case of a homopolymer shown in Fig.(7.1). The two branches of each of the $N(\mu)$ curves in Fig.(8.1) correspond to the $N \sim \mu^{-1}$ behaviour of a Θ-solvent chain (left branch: $\mu \to 0$) and a fully collapsed infinite globule (right branch) as discussed for a homopolymer in Section 7.3. Since N is always fixed by tuning μ, it is possible to distinguish from a plot like the one shown in Fig.(8.1) whether the system is left of the coil-globule transition point (i.e. in the open chain regime) or right of the transition point (i.e. in the globular regime). However, for fixed N, it is necessary to choose one of the two branches. Since this work focuses on the study of globular structures, the numerical calculations are always restricted to the right branch including the minimum. The self-consistent field theory is only expected to give good result for this branch since fluctuations are neglected.

The three-body interaction parameter w is chosen to be $w = 1$ throughout the entire

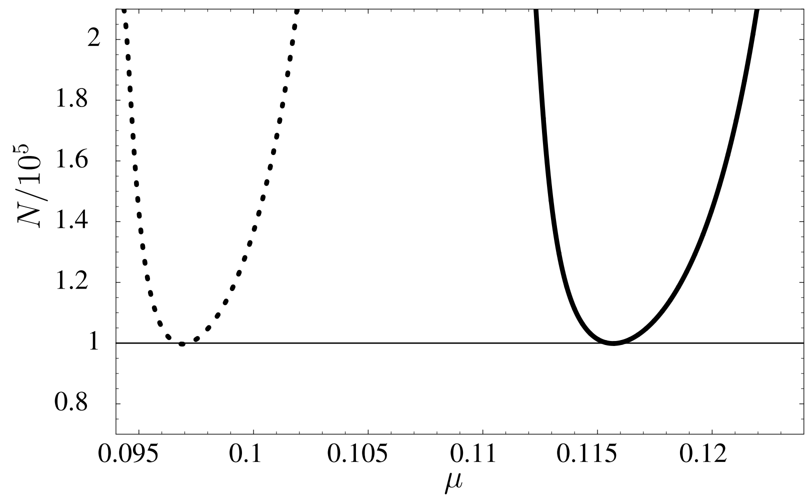

Figure 8.1: N as a function of μ for $w = 1$, $= 0.2$ and $\sigma = 10^{-4}$. The dotted curve corresponds to $\epsilon = 0.08$ and $\chi = 0$. The continuous curve corresponds to $\epsilon = 0.1$ and $\chi = 0.0138$.

chapter and the two-body interaction constant v is always negative to ensure that the system stays in the globular regime (up to the transition point).

A short remark on the terminology that will be used below is necessary at this point. The terms phase and transition will be used frequently although the system is a polymer of finite length. All transitions are therefore crossover transitions of finite width with continuous order parameters. It is nevertheless common within the soft matter community to use the the term ‘phase’ to distinguish the different structural states of a polymer and to refer to the crossover between these states as a ‘transition’.

In the following section the coil-globule transition of the copolymer is discussed. The transition is triggered by the non-selective two-body interaction parameter v and is therefore very similar to the one of the homopolymer. In Section 8.3 the energy gain per stiff segment ϵ is varied which leads to an increase in the fraction of stiff segments similar to the one-dimensional helix-coil transition described in Section 6.1. A transition to a nematic liquid-crystalline globule can be triggered by increasing the selective two-body interaction ($|\chi|$) even without an explicit alignment interaction between the rods ($g = 0$). This is discussed in detail in Section 8.4. The N-dependence of this transition is studied in Subsection 8.4.1, the influence of the cooperativity (σ) on the transition in 8.4.2 and its g-dependence in 8.4.3. In Subsection 8.4.4 the explicit alignment interactions is switched on ($g \neq 0$) to study how it influences the formation of the liquid-crystalline globule. The behaviour of the free energy in the transition region is discussed in Subsection 8.4.4 and Section

8.5 finishes this chapter with references to existing literature and a brief discussion on the relevance of the results to proteins.

8.2. Coil-globule transition

The rod-coil multiblock copolymer shows a coil-globule transition similar to the homopolymer globule discussed in the previous chapter. To demonstrate this, the interactions which are specific for the stiff segments are set to zero, that is $\chi = g = 0$. In addition, the energy gain per stiff segment is set to zero ($\epsilon = 0$) and it is assumed that there is no cooperativity in the formation of stiff segments ($\sigma = 1$). The two-body interaction constant v is varied. The transition point between coil and globule is defined as in Chapter 7 to be the minimum of the $N(\mu)$-curve. The length of the polymer is fixed at $N = 550$. Fig.(8.2) shows the profile of the total density $\rho(\mathbf{r})$ of the copolymer as a function of radial distance from the centre. The total density $\rho(\mathbf{r})$ at each point is given by

$$\rho(\mathbf{r}) = \rho_{\mathrm{C}}(\mathbf{r}) + \rho_{\mathrm{R}}(\mathbf{r}) = \frac{1}{2}\varphi^2(\mathbf{r}) + \frac{1}{2}\psi_0^2(\mathbf{r}) + \frac{1}{2}\psi_2^2(\mathbf{r}). \tag{8.1}$$

As can be seen from Fig.(8.2), the density profile becomes broader with decreasing

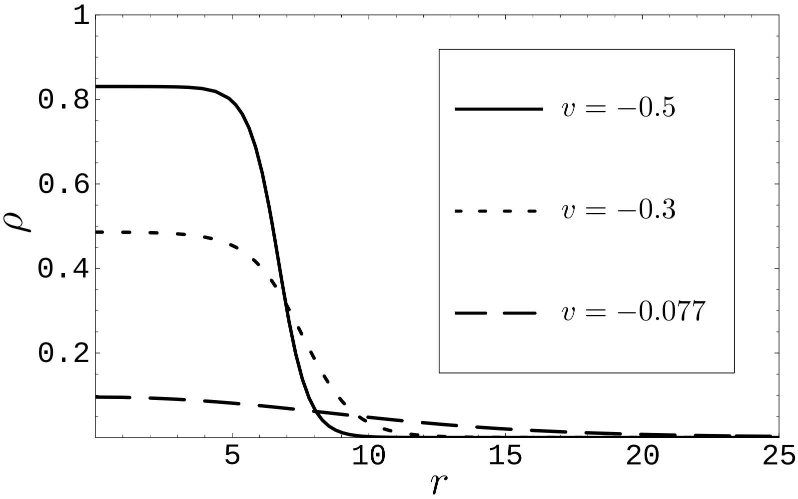

Figure 8.2: This plot shows the radial density profile of the entire copolymer in radial direction for different values of v. The dashed curve for $v = -0.077$ corresponds to the coil-globule transition point.

$|v|$. At $v = -0.5$ the copolymer is deep in the globular state with a big plateau of almost constant density and a rather small surface layer of decreasing density.

At the transition point $v = -0.077$ the plateau basically vanished and the surface layer becomes very broad. To further illustrate the structural change, Fig.(8.3) shows a colour-coded plot of the local density in ϱ-z space, where ϱ denotes the radial direction and z the axial direction in cylindrical coordinates as introduced in Chapter 6. The centre of the globule is located at the bottom left corner of each picture. The pictures on the left show the local density of flexible segments and the pictures on the right the local density of stiff segments. Red indicates high density and dark blue zero density. In the upper two plots the copolymer is at the transition point ($v = -0.077$). In the lower two plots it is deep in the globular state ($v = -0.5$).

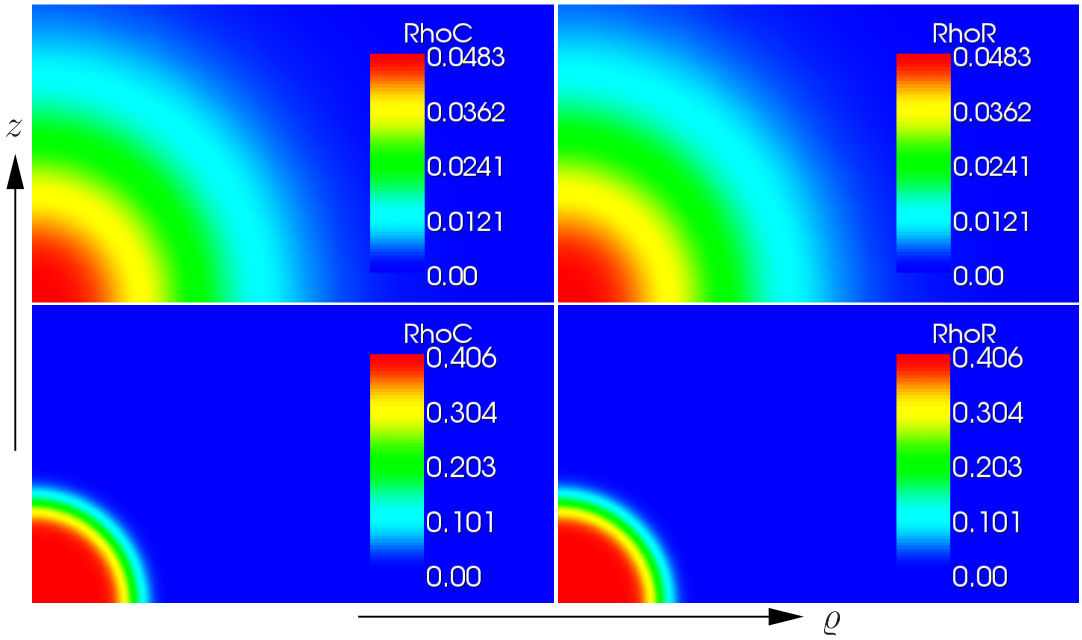

Figure 8.3: The density of flexible segments is shown on the left and the density of stiff segments on the right. $v = -0.077$ for the upper plots and $v = -0.5$ for the lower plots.

The structural change shown in Figs.(8.2, 8.3) gives only a vague indication of a crossover transition from coil to globule. A better indication would be a drop or a strong decrease of the average total density $\bar{\rho}$ of the globule at the transition point. To calculate the average density $\bar{\rho} = N/\left(\frac{4\pi}{3}R^3\right)$, a reasonable definition of the radius R of the globule is needed. As in Section 7.3, the point R in radial direction at which the density $\rho(R)$ has decreased to $\rho(R) = 10^{-3}\rho_0$ is chosen, where ρ_0 is the maximum density at the centre. In Fig.(8.4) the average density $\bar{\rho}$ is plotted as a function of v. It can be seen that around the transition point there is a small drop in the average density. A much clearer indication that $v = -0.077$ corresponds to a transition point can be seen from Fig.(8.5), where the globule radius itself is plotted versus v.

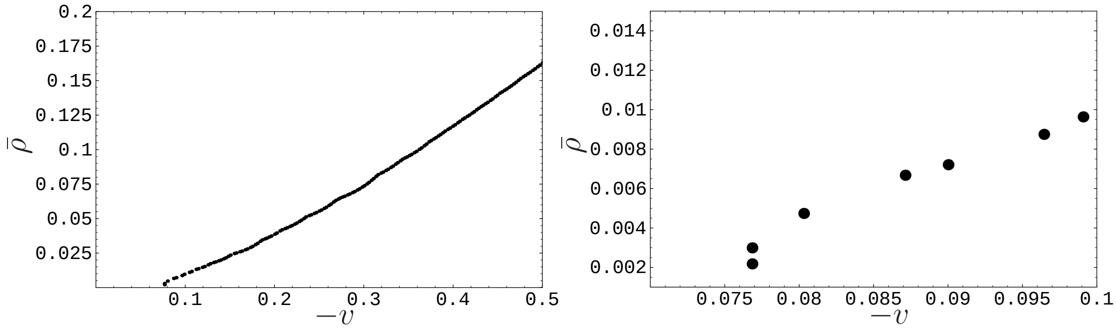

Figure 8.4: The average density $\bar{\rho}$ is plotted as a function of v. The plot on the right shows a magnification of the first data points for very small $|v|$.

The radius R shows a rapid increase when $v = -0.077$ is approached. Note, that the copolymer is finite (here: N=550) and therefore all transitions are crossover transitions as discussed in Chapter 7. Hence the order parameters show a strong increase in the crossover region rather than an abrupt jump.

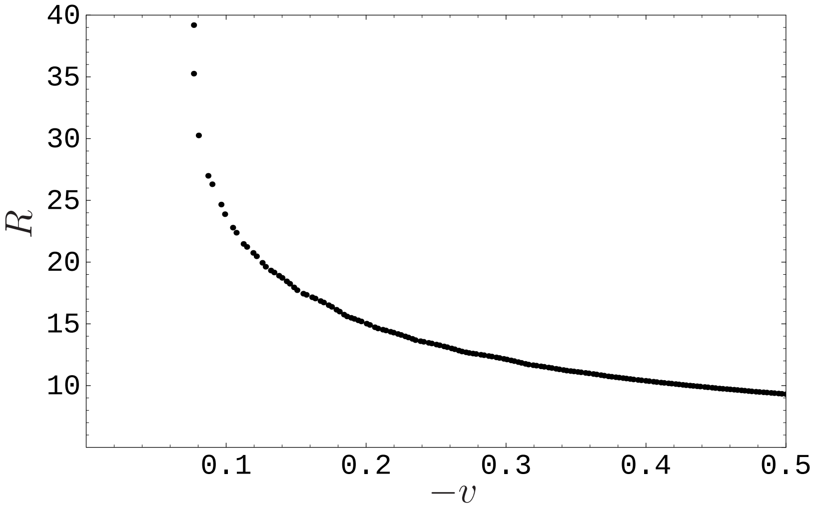

Figure 8.5: The globule radius R is plotted as a function of v.

It is also of interest to investigate whether the fraction of stiff segments changes during the crossover from open coil to dense globule. There is no cooperativity ($\sigma = 1$) and thus no energy penalty for forming single stiff segments. The fraction of stiff segments at the transition point ($v = 0.077$) is therefore roughly 1/2. Fig.(8.6) shows that it stays almost constant with increasing $|v|$. In Section 8.4, it will be demonstrated that this behaviour changes drastically when an additional attractive interaction between the stiff segments is introduced to trigger the crossover towards a globular state.

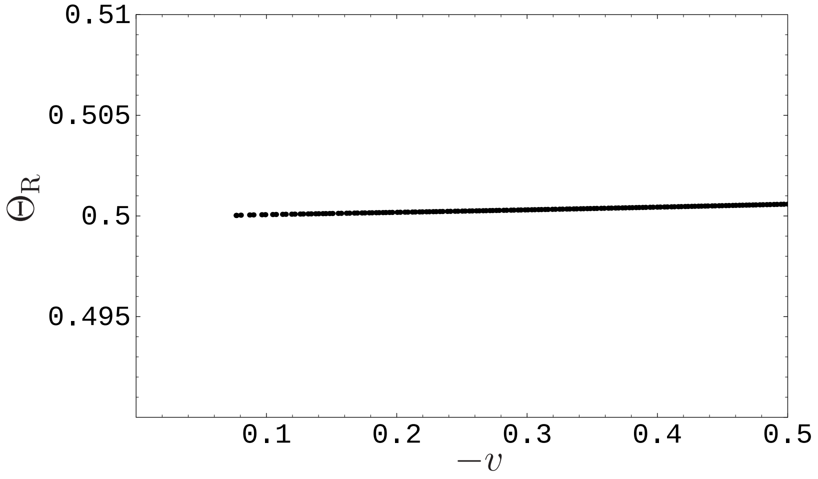

Figure 8.6: The fraction of stiff segments Θ_{R} is plotted versus v.

8.3. Fraction of stiff segments

In this section the fraction of stiff segments in investigated as a function of the energy gain per stiff segment ϵ. This is similar to the helix-coil transition described in Section 6.1. A major difference is the fact that the model used here is a three-dimensional model of the polymer including interactions, whereas the Zimm-Bragg model (and its extensions) discussed in Section 6.1 are one-dimensional models with no interactions and no explicit entropy term. On the other hand, the Zimm-Bragg model can be solved exactly, whilst the self-consistent field treatment of the three-dimensional model is a mean-field approach and neglects fluctuations.

Two different regimes will be discussed in the following: a low cooperativity regime with σ in the range $0.05 - 1$ and a high cooperativity regime with σ in the range $7 \cdot 10^{-3} - 10^{-4}$. Remember, that $\sigma = 1$ means no cooperativity and $\sigma = 0$ means total cooperativity.

Throughout this section χ and g are set to zero. There are therefore no specific interactions between the stiff segments. The only interactions are attractive two-body interactions and repulsive three-body interactions between all segments. Fig.(8.7) shows how the fraction of stiff segments Θ_{R} depends on ϵ for different values of σ in the range $0.05 - 1$. Even for small cooperativity, the slope clearly depends on σ and gets larger with increasing cooperativity (decreasing σ).

The high cooperativity regime is shown in Fig.(8.8). The slope of the $\Theta_{\mathrm{R}}(\epsilon)$-curves

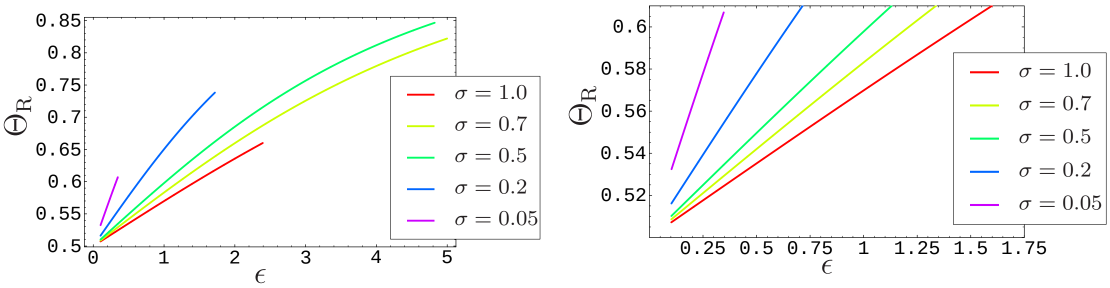

Figure 8.7: The fraction of stiff segments Θ_R is plotted as a function of energy gain ϵ per stiff segments for small (and zero) cooperativity. $v = -0.025$ and $N = 2.5 \cdot 10^4$. The plot on the left hand side is a magnification of the lower left corner to distinguish the different slopes.

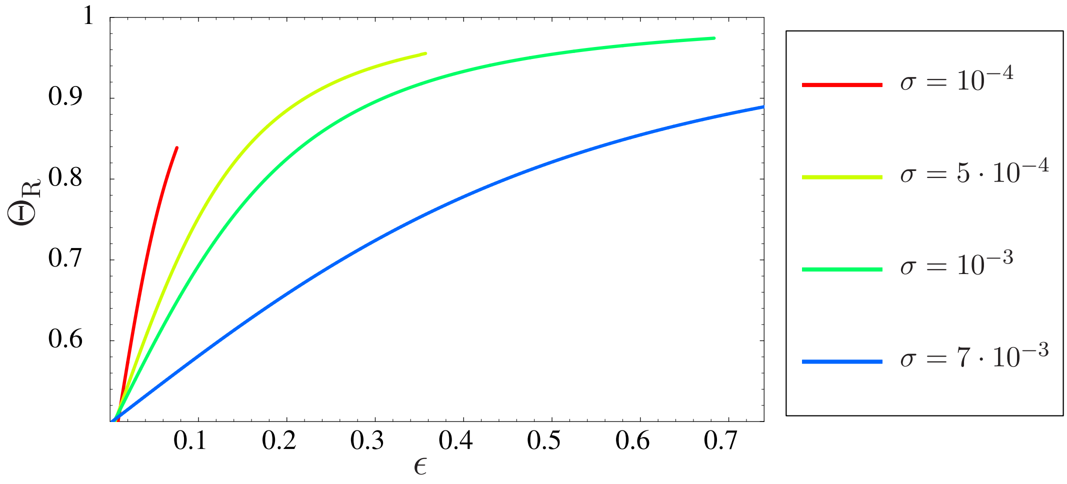

Figure 8.8: The fraction of stiff segments Θ_R is plotted as a function of ϵ for high cooperativity. $v = -0.2$ and $N = 10^5$.

increases with decreasing σ as expected. Especially for $\sigma = 10^{-3}$ (green curve) it can be seen that the curve is asymptotically approaching $\Theta_R = 1$. The curves for $\sigma = 10^{-4}$, $5 \cdot 10^{-4}$ and 10^{-3} end at a certain value of ϵ. The endpoints correspond to the coil-globule transition point. This can be explained as follows. If there is no additional selective interaction energy which favours a compactification of the stiff segments (i.e. $\chi = g = 0$), the stiffening of parts of the chain due to an increase of Θ_R with increasing ϵ pushes the chain segments further apart from each other and therefore leads to a more open structure. From a certain value of ϵ on, the system is thus pushed into the open chain regime. For higher cooperativity this effect is stronger, since the system forms less junctions points and hence on average longer rods. For smaller σ the coil-globule transition point is therefore reached at smaller values of Θ_{R} and ϵ.

To illustrate this stiffening, in Fig.(8.9) the average rod length L_{R} is plotted as a function of ϵ for $\sigma = 10^{-4}$. In units of b the average rod length L_{R} is given by the total number of stiff segments divided by half the total number of junction points between stiff rod and flexible chain. In the self-consistent field theory approach L_{R} is given by

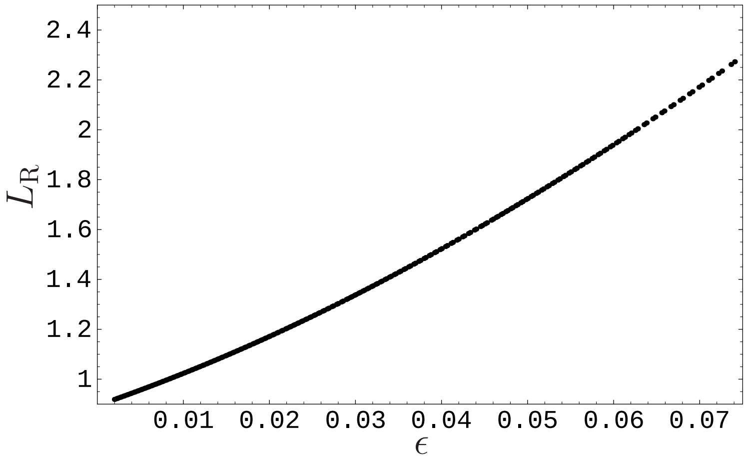

Figure 8.9: The average rod length L_{R} is plotted as a function of ϵ for $\sigma = 10^{-4}$, $v = -0.2$ and $N = 10^5$.

$$\frac{L_{\mathrm{R}}}{b} = \frac{\int_0^\infty d\varrho\, \varrho \int_{-\infty}^{\infty} dz\; [\psi_0^2(\varrho, z) + \psi_2^2(\varrho, z)]}{\int_0^\infty d\varrho\, \varrho \int_{-\infty}^{\infty} dz\; \varphi(\varrho, z)\, \psi_0(\varrho, z)}. \tag{8.2}$$

Fig.(8.9) shows that for $\epsilon = 0$ the average rod length is roughly equal to 1. For $\epsilon > 0$ the cooperativity effect sets in and the average rod length increases up to $L_{\mathrm{R}} \approx 2.3$. At this value the stiffening of parts of the chain is strong enough to drive the polymer in the open chain regime.

It is of interest to compare the results of this three-dimensional model with interactions with the exact one-dimensional Zimm-Bragg model discussed in Section 6.1. This is done in Fig.(8.10) for $\sigma = 10^{-3}$. Note, that in the Zimm-Bragg language the ϵ used here corresponds to $-\Delta f = \ln s$.

In the Zimm-Bragg model the increase of Θ_{R} is steeper. This can be explained by the fact that in the three-dimensional model the entropy of the flexible and the stiff segments is explicitly taken into account, which hinders the generation of stiff segments. On the other hand, the mean-field character of the three-dimensional model might also weaken the cooperativity effect.

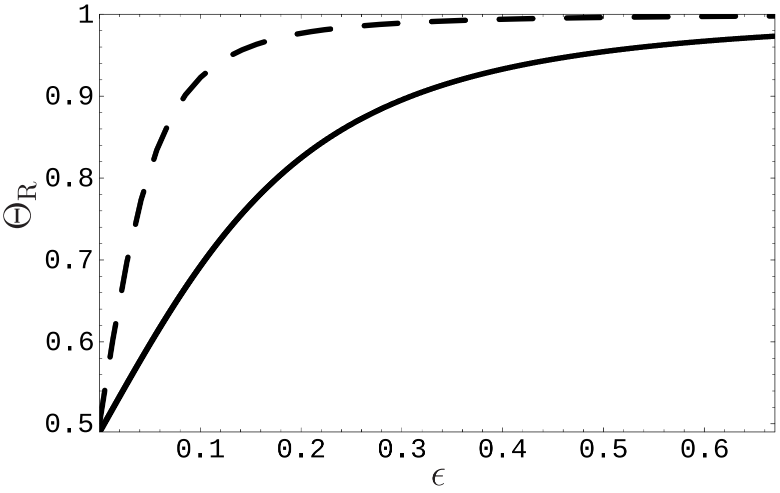

Figure 8.10: Θ_{R} is plotted as a function of ϵ for $\sigma = 10^{-3}$. The continuous curve shows the numerical result for $v = -0.2$ and $N = 10^5$. The dashed curve shows the result of the one-dimensional Zimm-Bragg theory.

8.4. Transition from amorphous to liquid-crystalline globule

The model also shows a crossover transition from a disordered amorphous globule with a low or moderate fraction of stiff segments to an ordered liquid-crystalline globule with a very high fraction of stiff segments. In Fig.(8.11), on the left, the fraction of stiff segments Θ_{R} is plotted as a function of the selective two-body interaction parameter χ, which controls the strength of the additional interaction between stiff segments and therefore models selective solvent conditions. On the right the nematic order parameter S (as defined by Eqs.(6.29, 6.30)) is plotted as a function of χ. Throughout the entire section, the non-selective two-body interaction parameter is set to $v = -0.2$. The two plots in Fig.(8.11) demonstrate that the the onset of nematic order and the increase in the fraction of stiff segments occur simultaneously.

This transition occurs without an explicit angle-dependent alignment interaction, that is $g = 0$. The transition is triggered by a subtle interplay of the entropy contribution (surface energy), represented by the derivative terms in Eq.(6.34), and bulk interaction energy, represented by the χ-term. This surface energy has an entropic nature since the conformational set of surface segments is constrained [38]. In a simple homopolymer globule (as discussed in Chapter 7) it is isotropic. For the rod-coil copolymer the surface energy is anisotropic and the surface tension in ϱ-direction is smaller than the one in z-direction. That is why the system tries

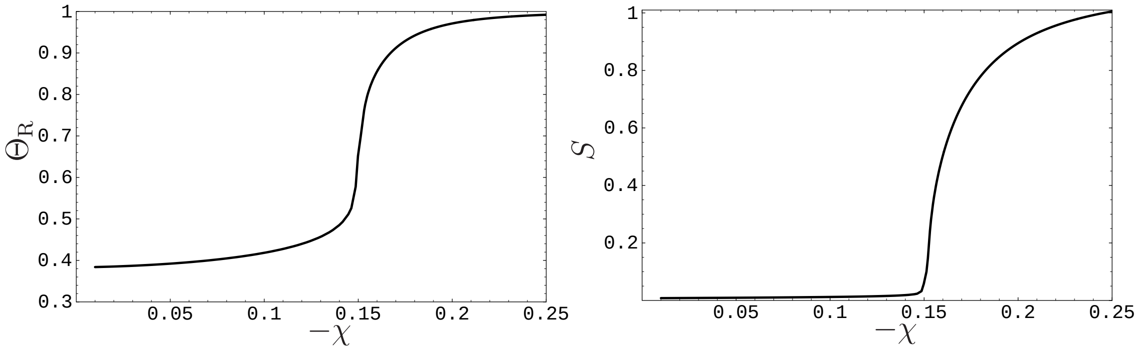

Figure 8.11: The fraction of stiff segments Θ_R (left) and the nematic order parameter S (right) are plotted as functions of χ for $\sigma = 10^{-4}$, $N = 9.5 \cdot 10^3$ and $\epsilon = g = 0$.

to maximise its lateral surface in ϱ-direction and minimise it in z-direction, i.e. a nematic, cigar shaped, liquid-crystalline globule is formed.

To demonstrate how the shape of the globule changes during the transition, Fig.(8.12) shows a colour-coded plot of the local density in ϱ-z space. The centre of the globule is in the bottom left corner of each picture. ϱ is increasing from left to right and z is increasing from bottom to top. Red indicates high density and dark blue zero density. In Fig.(8.12) a different set of parameters is chosen: $\sigma = 10^{-4}$, $N = 10^5$ and $\epsilon = 0.1$. Below, it will be discussed in detail how the nature of the crossover transition changes with σ, ϵ and N. The values of χ in Fig.(8.12) are chosen such that the top two pictures ($\chi = -0.0138$) show the system at the transition point between coil and globule, the middle two pictures ($\chi = -0.0812$) show the system at the transition point between amorphous and liquid-crystalline globule (as defined below) and the bottom two pictures ($\chi = -0.18$) show the system deep in the liquid-crystalline globule phase. The transition from amorphous to nematic liquid-crystalline globule is a crossover transition of finite width. If one wants to characterise the χ-interval of the crossover region by a single transition point, a reasonable definition of this point must be found. It is a rather obvious choice, to define the transition point as the inflection point of the $S(\chi)$-curve in Fig.(8.11).

At the transition point between coil and globule the system is spherical and has a very broad surface layer of decaying density. Although the density of the helical segments shown on the right is higher than the density of the flexible segments shown on the left, their distribution and the shape of the profile is very similar. At the transition point between amorphous and liquid-crystalline globule the system adopts a slightly cylindrical shape indicating the onset of nematic order. It can also be seen that the density maximum of the flexible segments is not in the centre of the globule denoting a repulsion of flexible segments from the centre to the surface layer. The surface layer is now much narrower. Deep in the liquid-crystalline phase the globule

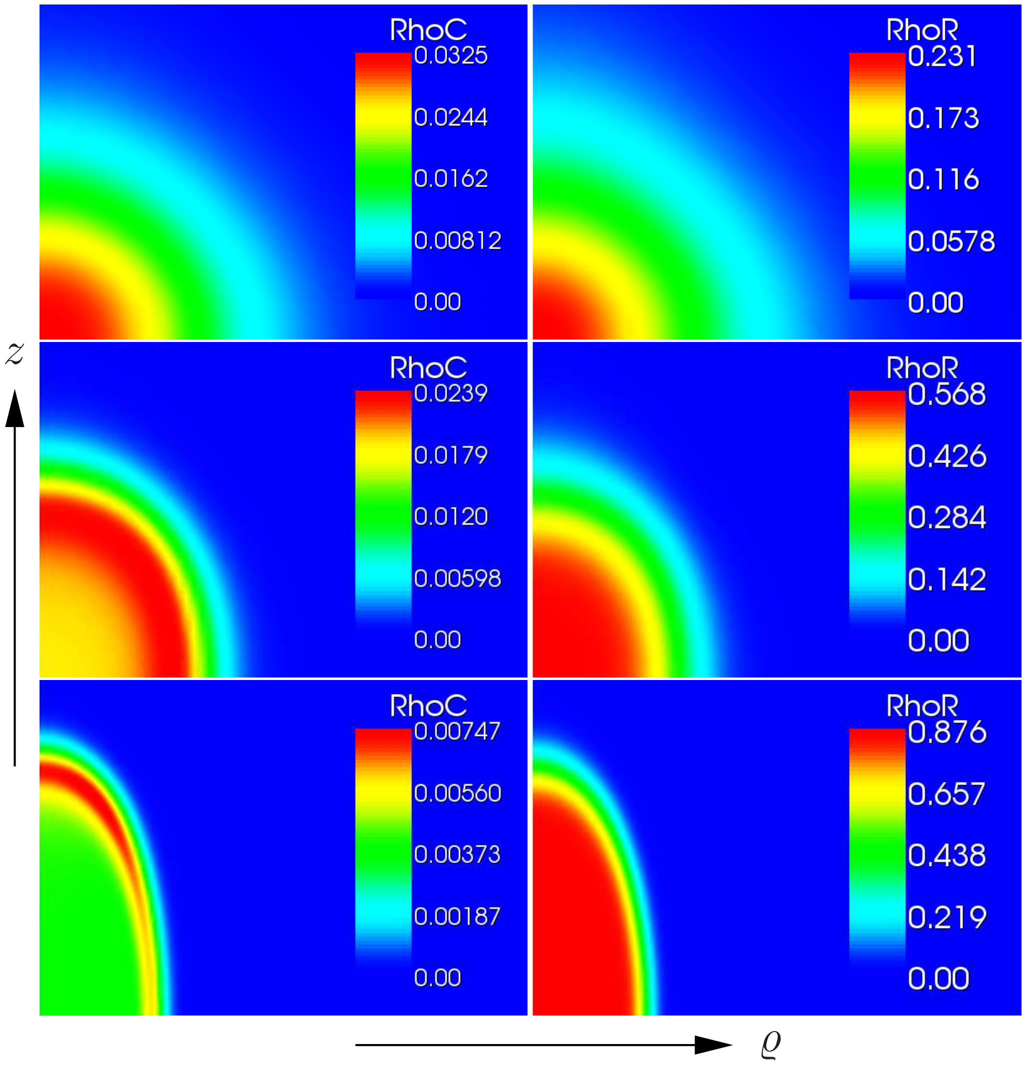

Figure 8.12: The density of the flexible segments is shown on the left and the density of the stiff segments on the right. $\sigma = 10^{-4}$, $\epsilon = 0.1$ and $N = 10^5$ for all plots. $\chi = -0.0138$ in the top line, $\chi = -0.0812$ in the middle line and $\chi = -0.18$ in the bottom line.

has developed a strongly asymmetric cylindrical shape indicating strong nematic order. The repulsion of flexible segments from the centre towards the surface layer can be seen clearly and the surface layer is now very narrow.

8.4.1. N-dependence

In this subsection it is investigated how the total chain length N influences the transition from amorphous to liquid-crystalline globule. Fig.(8.13) shows the fraction of stiff segments as a function of χ for four different chain lengths. The crossover transition from an amorphous globule with moderate number of stiff segments to a liquid-crystalline globule with very high number of a stiff segments becomes sharper with decreasing chain length, which, at first sight, is a rather unusual and surprising behaviour.

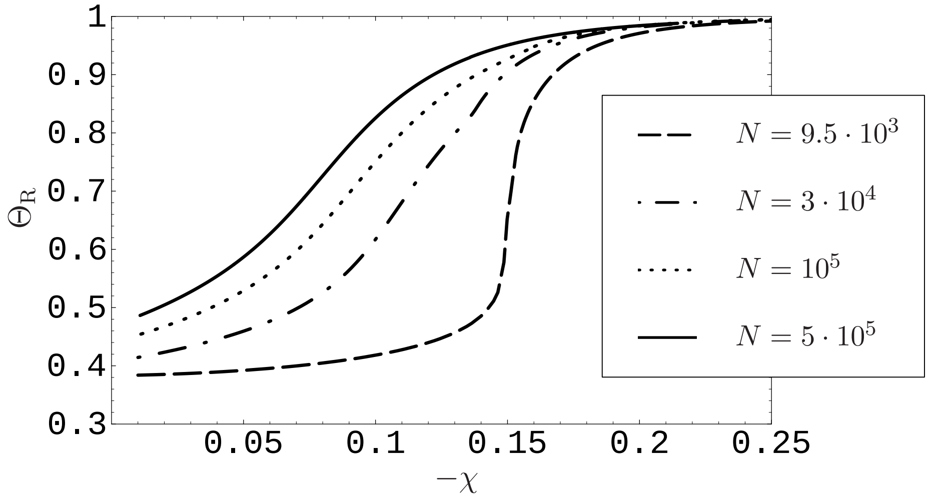

Figure 8.13: The fraction of stiff segments Θ_R is plotted as a function of χ for different chain lengths. The crossover transition becomes sharper with decreasing chain length.

Fig.(8.14) shows the nematic order parameter S as a function of χ for the four chain lengths. It can be seen that the increase in the order parameter is stronger for shorter chains. For $N = 5 \cdot 10^5$ and $\chi = -0.214$ the system is already so deep in the globular phase that the corresponding value of μ, which keeps the chain length fixed at $N = 5 \cdot 10^5$, is very close to the value at which $N(\mu)$ diverges (see Fig.(8.1)). The tuning of the chemical potential μ to ensure fixed chain length N becomes therefore numerically impossible for higher values of $|\chi|$. Although it might be difficult to see, the corresponding $\Theta_R(\chi)$-curve in Fig.(8.13) also ends at $\chi = -0.214$.

The transition point between amorphous and liquid-crystalline globule is defined as the inflection point of the $S(\chi)$-curve. Fig.(8.14), therefore, does not give a clear indication of the N-dependence of the transition point.

To demonstrate how the shape of the liquid-crystalline globule changes with chain length N, Fig.(8.15) shows colour-coded density plots of ρ_C and ρ_R for the four different values of the chain length at $\chi = -0.18$. The plots illustrate that the system changes from a cigar-like shape for $N = 10^4$ towards an almost cylindrical shape for $N = 5 \cdot 10^5$. Fig.(8.15) also demsonstrates that the the surface layer becomes smaller for larger systems, which indicates that a larger system is deeper

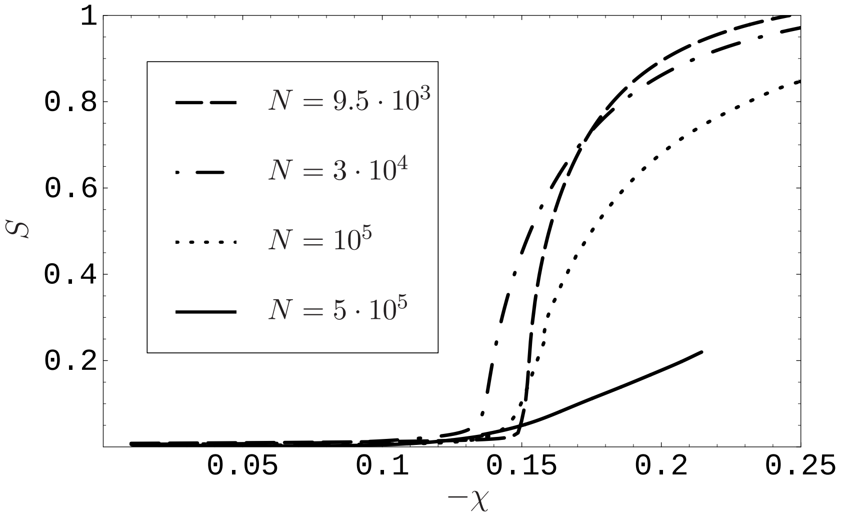

Figure 8.14: The nematic order parameter S is plotted as a function of χ for different chain lengths.

in the globular state at the same value of χ and v but at the same time showing less nematic order.

With increasing system size N the liquid-crystalline globule phase eventually vanishes (for $g = 0$). In the limit $N \to \infty$ the surface terms in Eqs.(6.35-6.37) vanishes. Since for $g = 0$ these terms are the only non-spherical symmetric terms, the system cannot adopt a liquid-crystalline globular state any more. Without explicit alignment interaction a liquid-crystalline globule with nematic order can therefore only form in finite systems. The crossover transition becomes sharper for smaller systems because the entropic surface terms become more important compared to the isotropic interaction terms. The total value of the isotropic bulk interaction energy roughly scales as the volume of the globule, whilst the surface energy scales as the surface area of the globule. This shows that the transition to a liquid-crystalline polymer globule is actually driven by entropy, due to the entropic origin of the surface energy.

Finally, in Fig.(8.16), the average length L_{R} of the stiff parts is plotted as a function of χ for $N = 10^4$ and $N = 5 \cdot 10^5$. The figure shows that the average length of the rods is equal to 1 for very small values of χ and $\epsilon = 0$. This is in agreement with the results from Section 8.3. For $N = 10^4$ it stays almost equal to 1 until the transition point is reached and then shows a rather strong increase. For very high values of χ it should reach an asymptotic value. However, for $\chi > 0.25$ the fraction of flexible segments ($1 - \Theta_{\mathrm{R}}$ see Fig.(8.11)) becomes unphysically small indicating that the mean field description within the self-consistent field treatment reaches the

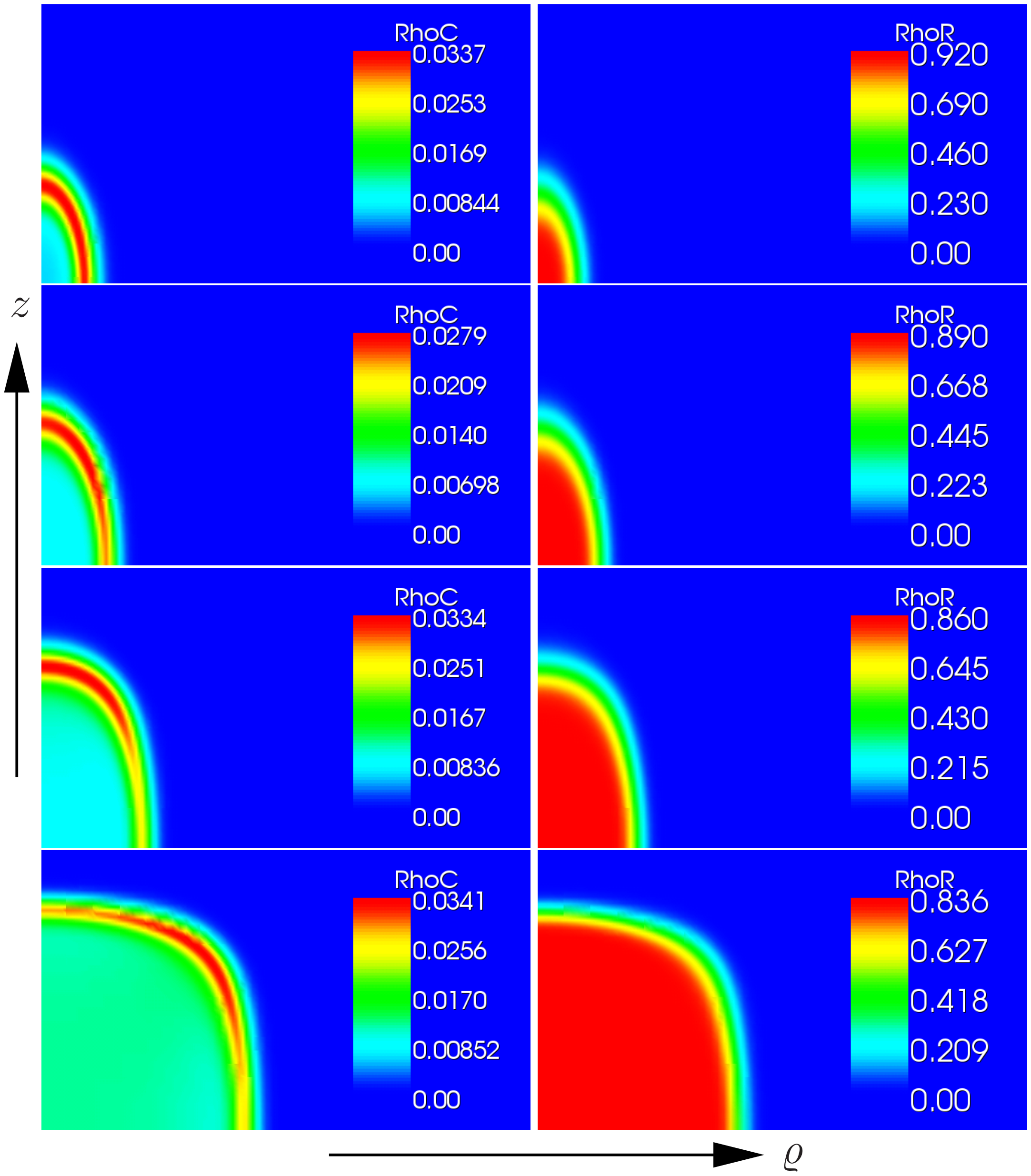

Figure 8.15: The density of the flexible segments is shown on the left and the density of the stiff segments on the right. $\sigma = 10^{-4}$, $\epsilon = g = 0.0$ and $\chi = -0.18$ for all plots. From top to bottom N increases as 10^4, $3 \cdot 10^4$, 10^5 and $5 \cdot 10^5$.

limit of its validity. For $N = 5 \cdot 10^5$ the crossover to a stronger increase in average rod length with $-\chi$ is much smoother analogous to Θ_{R} and S (see Figs.(8.13, 8.14)).

The stronger increase in average rod length for shorter polymers corresponding to

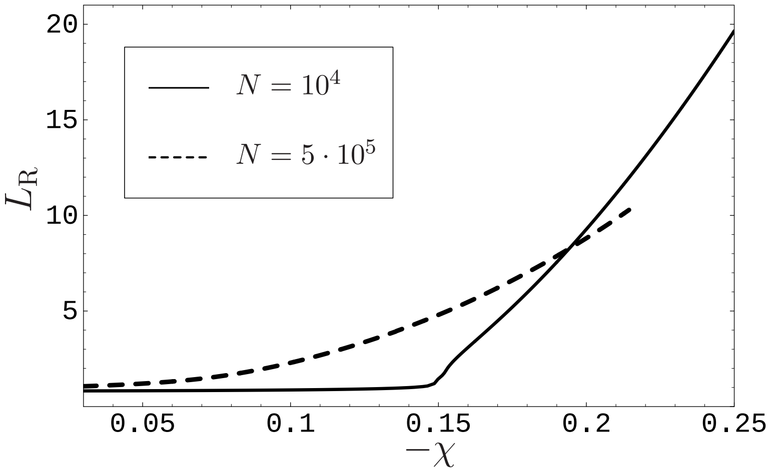

Figure 8.16: The average length L_R of the stiff parts is plotted as a function of χ for $N = 10^4$ and $N = 5 \cdot 10^5$.

a sharper isotropic-nematic transition indicates that this transition is also a cooperative process. To study the influence of cooperativity, the dependence of the isotropic-nematic transition on σ is discussed in the next subsection.

8.4.2. σ-dependence

The crossover from amorphous globule to liquid-crystalline globule is a cooperative process. As shown by Fig.(8.16), an increase in nematic order is not only accompanied by a strong increase in fraction of stiff segments but also by an increase in the average length of the stiff parts. To further investigate the cooperativity of the transition, the cooperativity parameter σ is varied for fixed chain length $N = 10^5$.

Fig.(8.17) shows that the crossover becomes sharper with increasing cooperativity (decreasing σ) as expected. For very high cooperativity ($\sigma = 10^{-5}$) and no selective interaction ($\chi \approx 0$), the fraction of stiff segments ($\Theta_\mathrm{R} = 0.2$) is much smaller than 1/2. When the transition point is approached, the fraction of stiff segments increases rapidly. For lower cooperativity (larger σ), not only is the crossover much smoother but the fraction of stiff segments at $\chi \approx 0$ is much higher ($\Theta_\mathrm{R} \approx 0.5$ for $\sigma = 10^{-3}$ and $\sigma = 5 \cdot 10^{-4}$). Both features clearly show the cooperativity of the transition.

The behaviour of the nematic order parameter S for different values of σ is shown in Fig.(8.18). For higher σ the increase in nematic order is less steep and the transition point is significantly shifted to higher values of $|\chi|$. For $\sigma = 5 \cdot 10^{-4}$ and higher, the system only develops a slight onset of order and S remains very small even deep in the globular state at $\chi = -0.25$. This also demonstrates the cooperativity of the

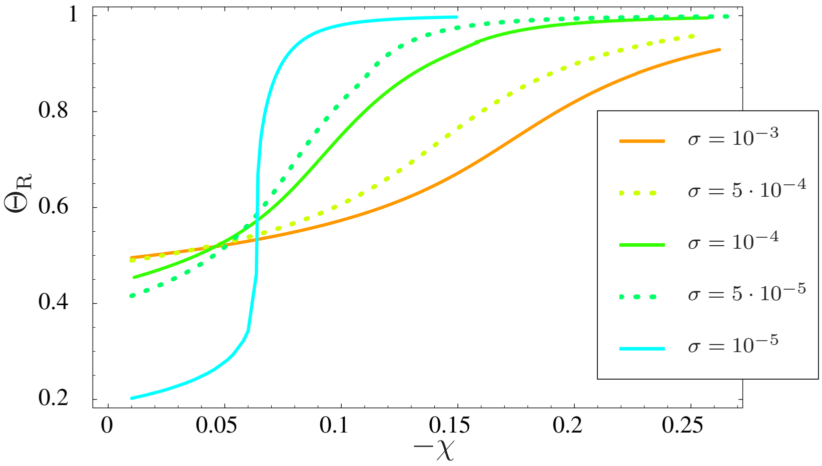

Figure 8.17: The fraction of stiff segments is plotted as a function of χ for different values of σ and $N = 10^5$, $\epsilon = g = 0$. The crossover transition becomes sharper with decreasing σ, i.e. increasing cooperativity.

transition.

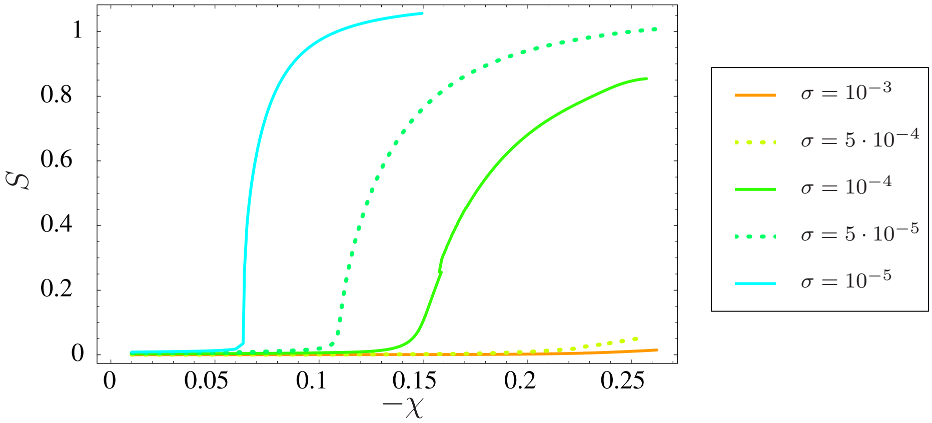

Figure 8.18: The nematic order parameter S is plotted as a function of χ for different values of σ and $N = 10^5$. The transition point is shifted to higher values of $|\chi|$ with increasing σ.

It is therefore of interest to investigate the average rod length L_{R}, which should also strongly depend on the cooperativity. Fig.(8.19) shows that the increase of L_{R} with $|\chi|$ after the transition point becomes steeper for smaller values of σ as one would expect.

The isotropic-nematic transition is enhanced by cooperativity and even becomes im-

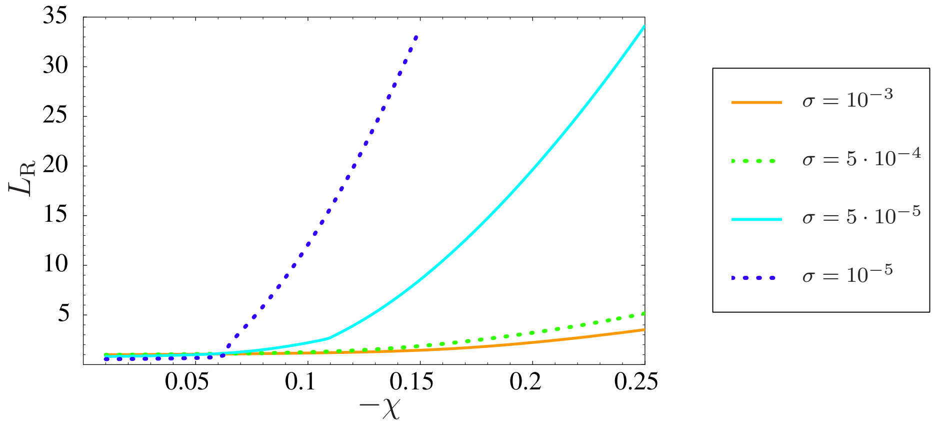

Figure 8.19: The average rod length L_R is plotted as a function of χ for different values of σ and $N = 10^5$.

possible if the cooperativity is too small. As can be seen from Fig.(8.19) and should be clear from the definition of the cooperativity parameter σ, only a cooperative system forms long rods and not just many very short ones. Remember, that σ is associated with the energy penalty for a boundary between rod and coil, see Section 6.1. The smaller σ is, the larger is this energy penalty and the more favourable is the formation of long rods rather than short ones. It is intuitively clear that long rods align much easier than very short ones. When the average rod length stays roughly equal to 1 for high values of $|\chi|$, alignment cannot happen. Hence cooperativity is important to drive this transition.

8.4.3. ϵ-dependence

In this subsection the ϵ-dependence of the transition from amorphous to liquid-crystalline globule is investigated. In Section 8.3, it was shown that the fraction of stiff segments increases with increasing energy gain ϵ per stiff segment. A higher value of ϵ yields a higher offset of Θ_R at $\chi = 0$ which should in turn lead to a smaller value of $|\chi|$ at the transition point.

Figs.(8.20, 8.21) demonstrate this behaviour. For all plots in this subsection the cooperativity parameter is set to $\sigma = 10^{-4}$ and the total chain length to $N = 10^5$. The explicit rod-rod alignment interaction is still switched off ($g = 0$). The onset of the transition is indeed shifted to lower values of $|\chi|$ with increasing energy gain per helical segments ϵ. This is due to an increase of bulk interaction energy for fixed χ with increasing number of stiff segments.

The curves for $\epsilon \geq 0.1$ in Figs.(8.20, 8.21) start at non-zero values of χ. These values

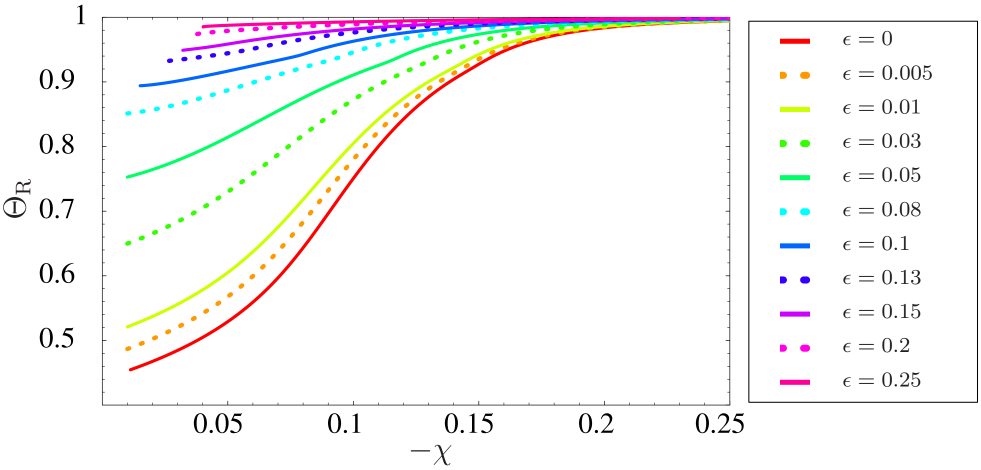

Figure 8.20: Fraction of helical segments Θ_R as a function of χ for different values of the energy gain per helical segment ϵ.

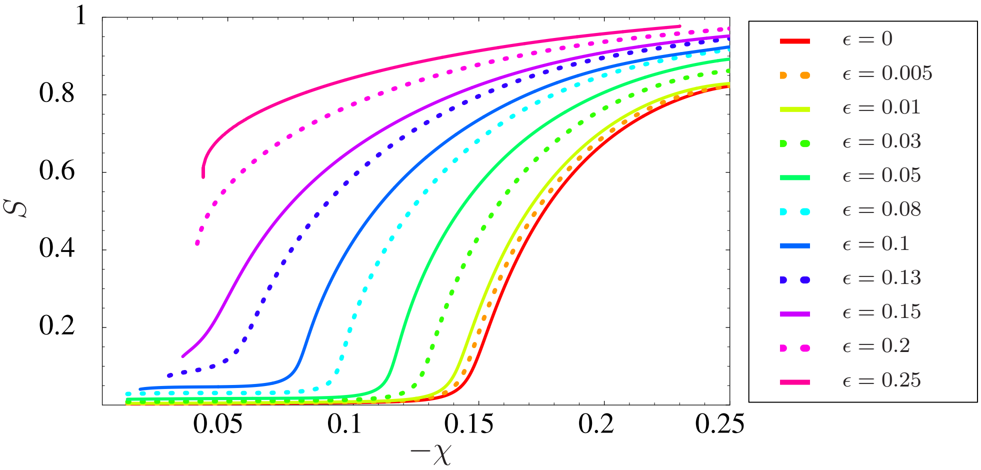

Figure 8.21: Nematic order parameter S as a function of χ for different values of ϵ.

of χ correspond to the transition point between open chain regime and globular regime, similar to the discussion in Section 8.2. The main difference in this case is that at $v = -0.2$ the non-selective attractive two-body interaction is not strong enough to drive the system into the globular state. The additional selective two-body interaction between the stiff segments only (with interaction paramter χ) is needed to drive the system into the globular state. That this is only the case for $\epsilon \geq 0.1$ can be explained as follows (see also Section 8.3). If there is no additional selective interaction energy which favours a compactification of the stiff segments, the stiffening of parts of the chain due to an increase of Θ_{R} with increasing ϵ pushes the chain segments further apart from each other and therefore leads to a more open structure. For $\epsilon \geq 0.1$, the system is thus pushed into the open chain regime at $\chi = 0$. Note, that this leads to a situation in which χ is now a critical parameter not only for the transtion from amorphous to liquid-crystalline globule but also from coil to globule. This is especially interesting for $\epsilon > 0.17$, since for these values, the system shows already at the transition point between coil and globule so much nematic order that $S(\chi)$ is on the right of its inflection point and the system is in the nematic phase.

These findings permit the computation of a complete phase diagram of the rod-coil copolymer in ϵ-χ space, see Fig.(8.24). But before this is done, it has to be checked whether the definition of the transition point between coil and globule as the minimum of the $N(\mu)$-curve is also reasonable in the case of strong nematic order. In Section 8.2 the radius R of the globule (defined as the point at which the total density has decreased to $\rho(R) = 10^{-3}\rho_0$) was plotted as a function of v, see Fig.(8.5). It showed a rapid increase when the transition point between globule and coil was approached. Here the globule shows nematic order and has an asymmetric shape. It is therefore necessary to distinguish between ϱ- and z-direction. The extensions of the globule in ϱ-direction R_ϱ and in z-direction R_z are defined - analogously to R in the case of a spherical globule - as $\rho(R_\varrho, 0) = \rho(0, R_z) = 10^{-3}\rho_0$. In Fig.(8.22) R_ϱ and R_z are plotted as functions of χ for $\epsilon = 0.25$. For this choice of ϵ, the system already shows strong nematic order at $\chi = -0.0396$ which corresponds to the transition point between globule and coil. Fig.(8.22) demonstrates that the definition of the transition point beween open chain and globular regime as the minimum of the N-μ curve is valid even if the system shows strong nematic order. Both curves in Fig.(8.22) show a rapid increase when approaching the transition point from the

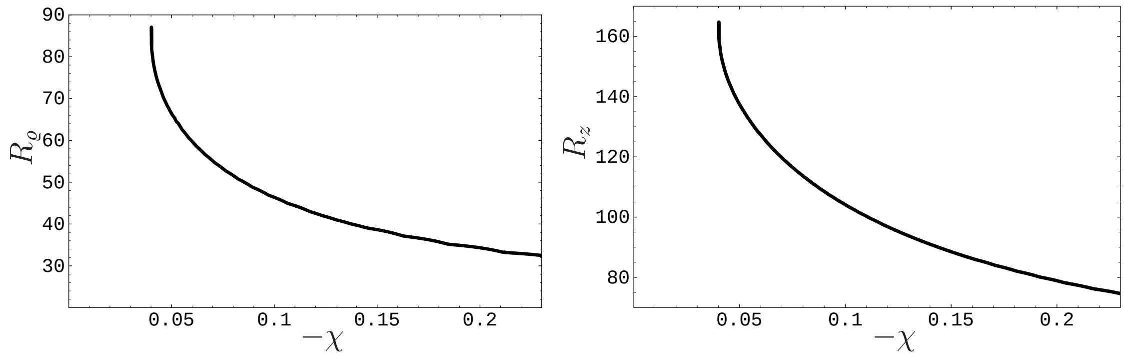

Figure 8.22: The extensions of the globule in ϱ-direction R_ϱ and in z-direction R_z are plotted as functions of χ for $\epsilon = 0.25$.

right. The different values of R_ϱ and R_z reflect the cylindrical shape of the globule due to the nematic order of the stiff segments. For $\epsilon = 0.25$ no isotropic globular phase exists and the crossover transition leads directly to a liquid-crystalline globule.

For $\epsilon = 0.1$ on the other hand, the system shows no nematic order at the transition point between open chain and globule ($\chi = -0.0138$). The system therefore undergoes two transitions. First from an open chain to an amorphous globule and then at higher $|\chi|$ from an amorphous to a liquid-crystalline globule. In Fig.(8.23) R_ϱ and R_z are plotted as functions of χ. When the transition point between open chain and globule (at $\chi = -0.0138$) is approached from the right, R_ϱ and R_z show the expected strong increase. When the transition point between amorphous and liquid-crystalline globule (at $\chi = -0.0812$) is approached from the left, R_ϱ and R_z show a different behaviour. In a small interval (corresponding to the width of the transition) R_z increases whilst R_ϱ decreases even stronger than before. In this interval the asymmetric shape of the globule is developed. This behaviour will be discussed further in Subsection 8.4.5.

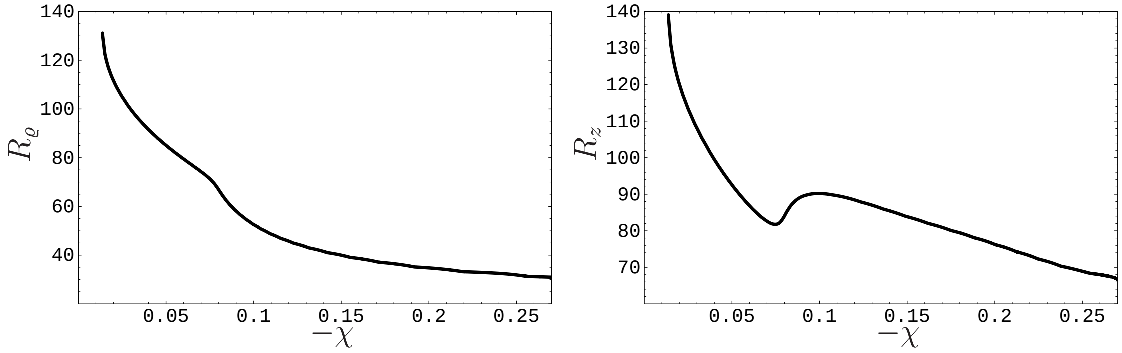

Figure 8.23: The extensions of the globule in ϱ-direction R_ϱ and in z-direction R_z are plotted as functions of χ for $\epsilon = 0.1$.

As already mentioned above, it is now possible to compute a complete phase diagram in ϵ-χ space. This phase diagram is shown in Fig.(8.24). The triangles are the transition points between open chain and globule. The squares are the transition points between amorphous and liquid-crystalline globule. Note, that the points plotted in the phase diagram, Fig.(8.24), are what is defined above as the points of rather broad crossover transitions. Therefore the boundaries in the phase diagram have to be understood as centre lines of broader regions in which the crossover from one phase to the other occurs. Quantitatively, the phase diagram depends on N, σ, g and v. The one shown in Fig.(8.24) represents a system with $N = 10^5$, $\sigma = 10^{-4}$, $g = 0$ and $v = -0.2$. However, the qualitative shape of the phase diagram stays the same. The discussions in the previous sections make it possible to anticipate how the phase diagram changes with N, σ and v. If $|v|$ is increased the open

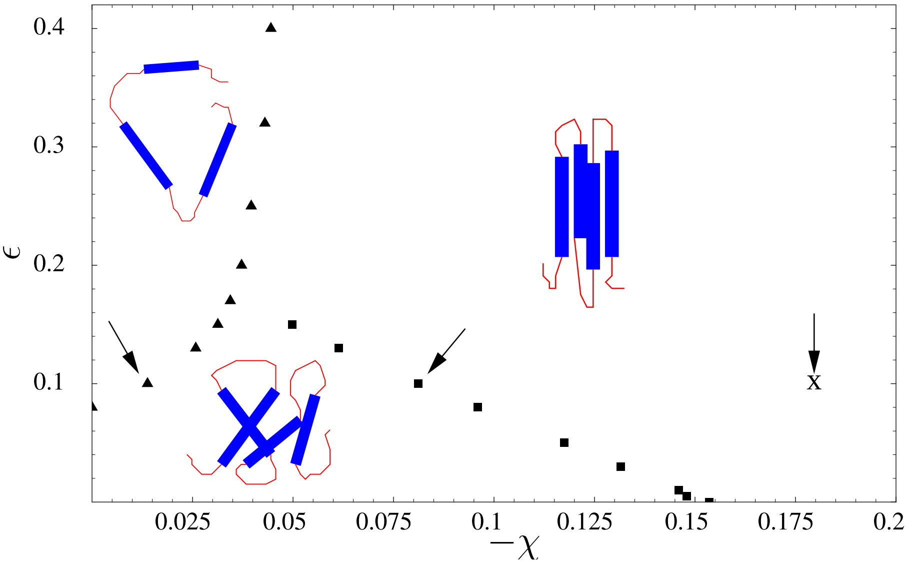

Figure 8.24: Phase diagram of a rod-coil copolymer in ϵ-χ space. The upper left area corresponds to an open chain, the lower left area to an amorphous globule and the right area to a nematic liquid-crystalline-globule. The little arrow to the left indicates the point in the phase diagram which corresponds to the top two pictures in Fig.(8.12). The arrow in the middle corresponds to the middle two pictures and the arrow to the right to the bottom ones. Parameters: $N = 10^5$, $\sigma = 10^{-4}$, $g = 0$.

chain region of the phase diagram becomes smaller (and disappears eventually). With decreasing σ the transition from a disordered to an ordered globule becomes sharper and the transition line between these two regions is shifted to smaller values of $|\chi|$, see Subsection 8.4.2. Since this transition occurs due to an interplay between surface energy and bulk interaction energy, the transition also becomes sharper for decreasing system size N. For smaller systems the surface energy plays a bigger role and therefore leads to a sharper transition, see Subsection 8.4.1. For $N \to \infty$ the ordered globule phase finally disappears, since the surface contributions to the free energy vanishes for infinite systems.

8.4.4. g-dependence

The transition from amorphous to liquid-crystalline globule occurs without an explicit angle-dependent alignment interaction between the rods. It is nevertheless interesting to switch the explicit rod-rod alignment interaction on and study its influence on the transition. The alingment interaction is chosen to be of the Maier-Saupe form and its strength is controlled by the interaction parameter g, see Eq.(6.32).

The influence of an attractive alignment interaction $g < 0$, which favours the alignment of the rods is studied first. In Fig.(8.25) the fraction of stiff segments is plotted as a function of χ for different values of g and $\sigma = 10^{-4}$, $\epsilon = 0$, $N = 9.5 \cdot 10^3$. The corresponding nematic order parameter S is shown in Fig.(8.26). The transition

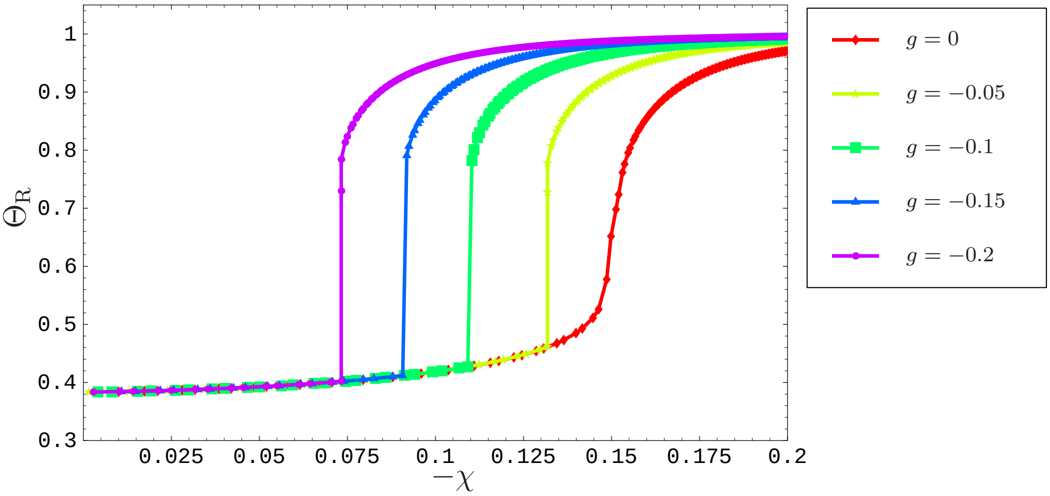

Figure 8.25: Fraction of helical segments Θ_R as a function of χ for different values of g.

is shifted to lower values of values of $|\chi|$ with increasing $|g|$. This is not suprising, since for $g < 0$ the alignment term provides an additional incentive for the system to generate nematic order and stiff segments. But the fact that almost up to the respective transition points the $\Theta_R(\chi)$-curves lie perfectly on top of each other is quite remarkable. This can be explained as follows. For $\psi_2 \equiv 0$ the alignment term in Eq.(6.32) is equal to zero. Therefore the system has to generate a finite ψ_2 (i.e. at least small nematic order) before the alignment interaction can have an effect on the system. As long as there is no nematic order in the system ($\psi_2 \equiv 0$) the alignment term is zero and the system behaves as the one with $g = 0$.

The increase of Θ_R and of S for $g < 0$ is slightly smoother than the curves joining the numerical data points in Figs.(8.25, 8.26) suggest. It is very hard to get numerical data points in this region of the curves due to the procedure of adjusting μ to fix

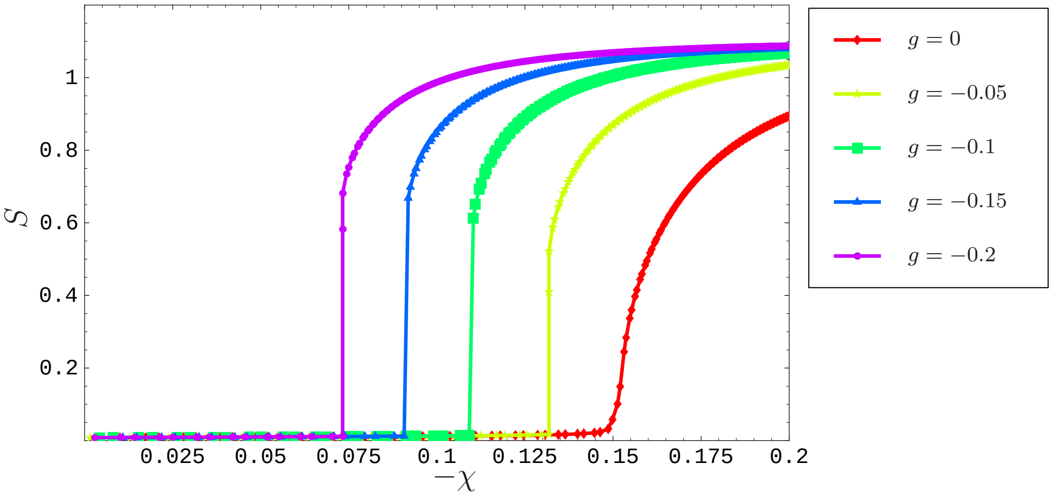

Figure 8.26: Nematic order parameter S as a function of χ for different values of g.

N. If N changes very sharply when χ is changed only slightly, the adjustment steps must be very small in order to control N. Therefore there are no points in a very small χ-interaval around the transition point for the curves with $g < 0$.

An attractive alignment interaction thus enhances the nematic order and shifts the transition point to lower values of $|\chi|$.

Instead of being attractive, the alignment interaction can also be chosen to be repulsive, that is $g > 0$. In Fig.(8.27) the fraction of stiff segments is plotted as a function of χ for $g = 1$ and, for comparison, $g = 0$. The system also shows a very strong increase in Θ_R at a certain value of χ, only slightly less than for $g = 0$. However, the nematic order parameter S stays very close to zero, as can be seen from Fig.(8.28). When the χ-value at which Θ_R starts to increase strongly is reached, the nematic order parameter increases to $S = 0.015$. But this in turn means that the alignment term increases as well. At $S = 0.015$ it is large enough to compensate the gain in surface energy due to the (still very small) nematic order and drives the system back into the isotropic regime with increasing $|\chi|$.

The colour-coded density plot in Fig.(8.29) demonstrates that the globule is still spherical for $\chi = -0.18$, although the fraction of stiff segments is very large ($\Theta = 0.87$) and the flexible segments are partly repelled from the centre of the globule.

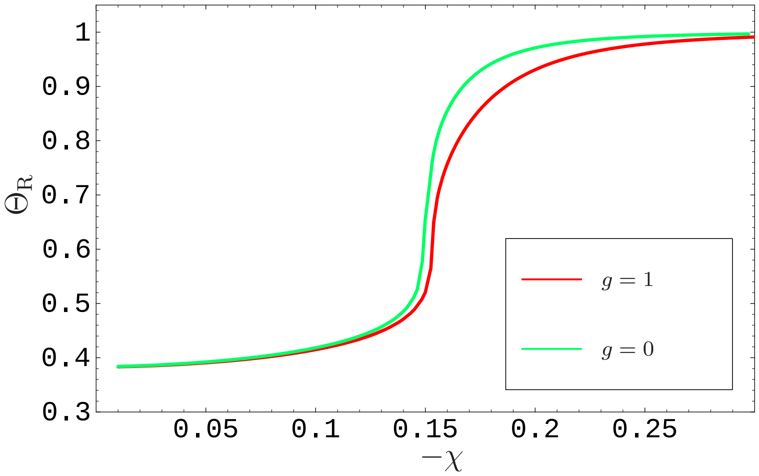

Figure 8.27: Fraction of stiff segments Θ_R as a function of χ for $g = 1$ and $g = 0$ (as a reference).

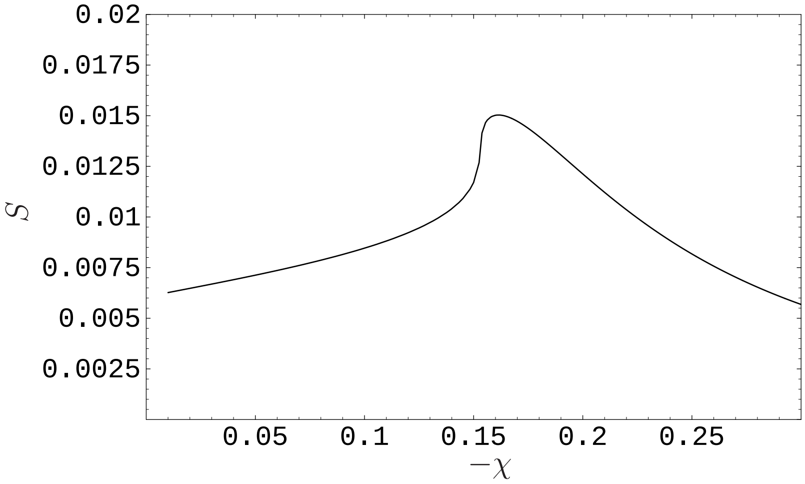

Figure 8.28: Nematic order parameter S as a function of χ for $g = 1$.

With a repulsive alignment interaction, it is possible to suppress the formation of a liquid-crystalline globule. In this case the system forms an amorphous globule with high fraction of stiff segments and a slight repulsion of the flexible segments from the centre of the globule to the surface layer. However, this situation is rather artificial and very unlikely to occur in real systems.

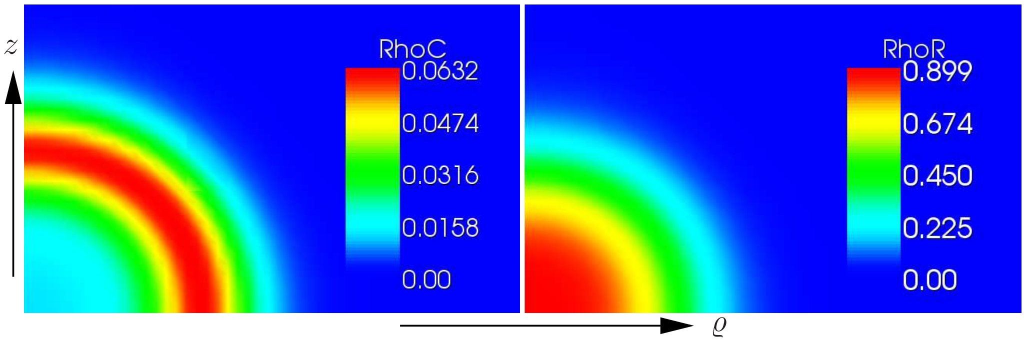

Figure 8.29: Densities of flexible and stiff segments, ρ_{c} and ρ_{R} respectively for $g = 1$ and $\chi = -0.18$.

8.4.5. Free energy

In this subsection the behaviour of the effective free energy and its individual contributions in the crossover region is investigated.

The effective saddle point grand potential Ω is given by Eq.(6.34). With the definition of the chemical potential used here (see Eq.(6.15) and Appendix A) the corresponding effective saddle point free energy is given by

$$F = \Omega - \mu N. \tag{8.3}$$

In Fig.(8.30) the free energy F is plotted as a function of χ for $\sigma = 10^{-4}$, $N = 9.5 \cdot 10^3$ and $\epsilon = g = 0$. These parameters are the same as the ones used in Fig.(8.11). Fig.(8.30) demonstrates that the free energy is changing its slope in the crossover region around the transition point as would be expected for a crossover. However, it is more interesting to look at the individual contributions to the saddle point free energy. These are plotted in Fig.(8.31). $F_{\varrho}^{\mathrm{surf}}$ denotes the terms of the surface contributions which contain derivatives with respect to ϱ and F_z^{surf} the ones which contain derivatives with respect to z. All other contributions are named after the parameters (interaction constants and σ) which control their strength. Fig.(8.31) shows that after the transition the interaction terms dominate the free energy. This is not surprising since the average density of the globule keeps increasing with increasing $|\chi|$. The contribution associated with the junctions between rod and coil F_{σ} is asymptotically approaching zero from below. This can be explained by an increase of average rod length as shown in Fig.(8.16) which leads to a decrease of the number of junction points between rod and coil.

At the beginning of Section 3.4 the occurrence of the transition from amorphous to liquid-crystalline globule was explained in terms of the interplay between surface energy and bulk interaction energy. Because of the anisotropy of the surface

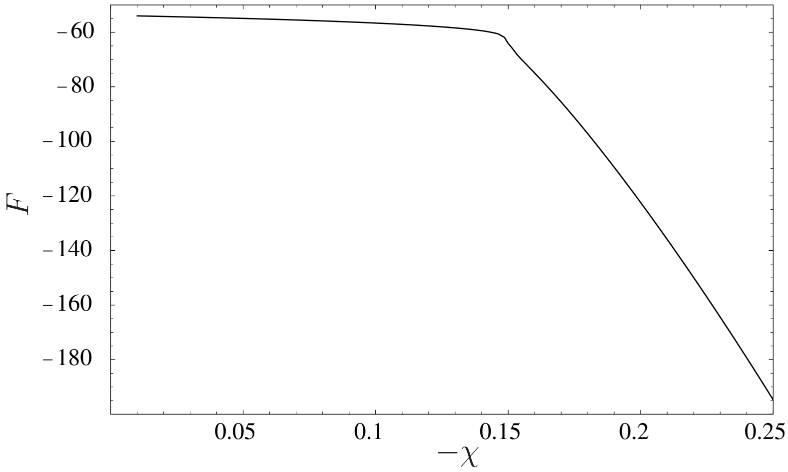

Figure 8.30: Free energy F plotted as a function of χ for $\sigma = 10^{-4}$, $N = 9.5 \cdot 10^3$ and $\epsilon = g = 0$.

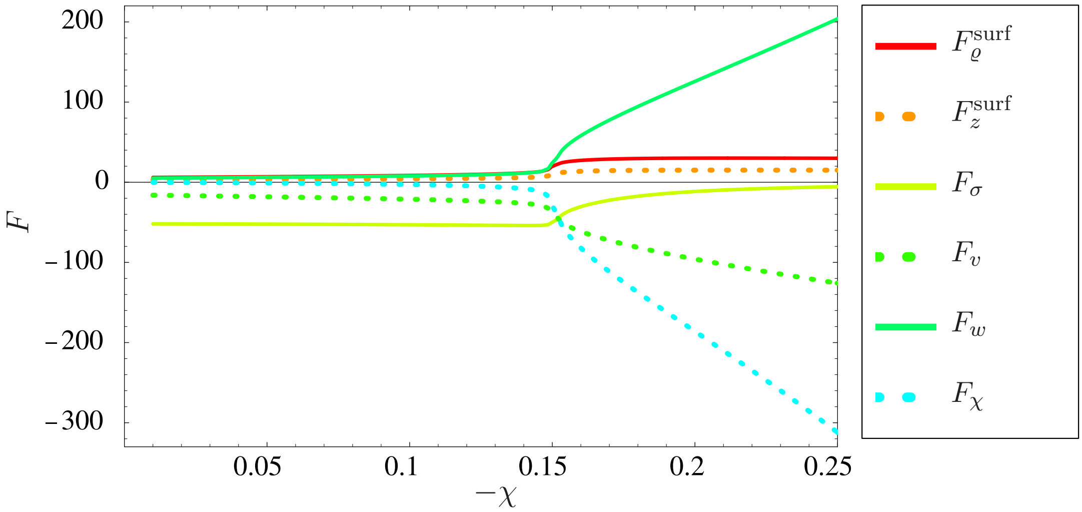

Figure 8.31: The individual contributions to the free energy F plotted as functions of χ for $\sigma = 10^{-4}$, $N = 9.5 \cdot 10^3$ and $\epsilon = g = 0$.

contributions which originate from the entropy of the rods, the globule tries to minimise its surface in z-direction and to maximise its surface in ϱ-direction. Before the transition the amorphous globule has a spherical shape. The surface energies in x-, y- and z-direction should therefore be all the same. For the cylindrical coordinates used here that implies $F_\varrho^{\mathrm{surf}} = 2F_z^{\mathrm{surf}}$. A magnification of the $F_\varrho^{\mathrm{surf}}$- and

F_z^{surf}-curves from Fig.(8.31) in Fig.(8.32) show that this is indeed the case. But also in the liquid-crystalline globule regime after the transition their ratio is roughly equal to 2 as can be seen from Fig.(8.32). The extension of the globule in ϱ- and z-direction on the other hand is now very different. It is therefore instructive to plot $F_\varrho^{\mathrm{surf}}$ and F_z^{surf} normalised by the corresponding cross sections of the globule. As an approximation of the cross section in z-direction R_ϱ^2 is chosen. The cross section in ϱ-direction is approximated by $R_\varrho R_z$, where R_ϱ and R_z are defined as in Subsection 8.4.3. In Fig.(8.33) the normalised surface contributions are plotted on the left hand side and R_ϱ and R_z one the right hand side. The plot on the left shows that the surface energy per area in z-direction becomes indeed larger than the one in ϱ-direction in the interval in which the crossover from amorphous globule

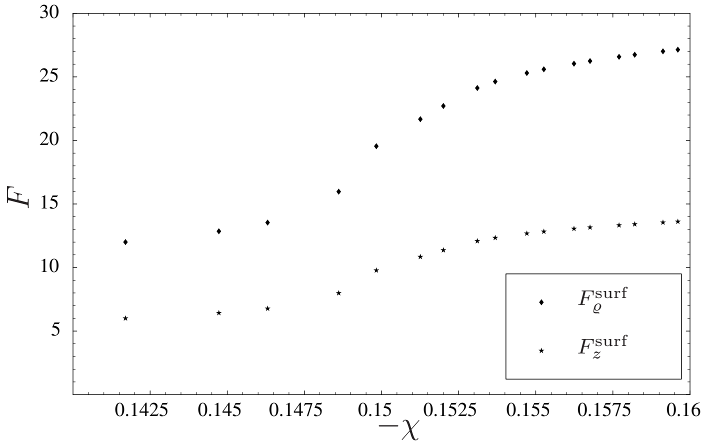

Figure 8.32: $F_\varrho^{\mathrm{surf}}$ and F_z^{surf} plotted as functions of χ for $\sigma = 10^{-4}$, $N = 9.5 \cdot 10^3$ and $\epsilon = g = 0$.

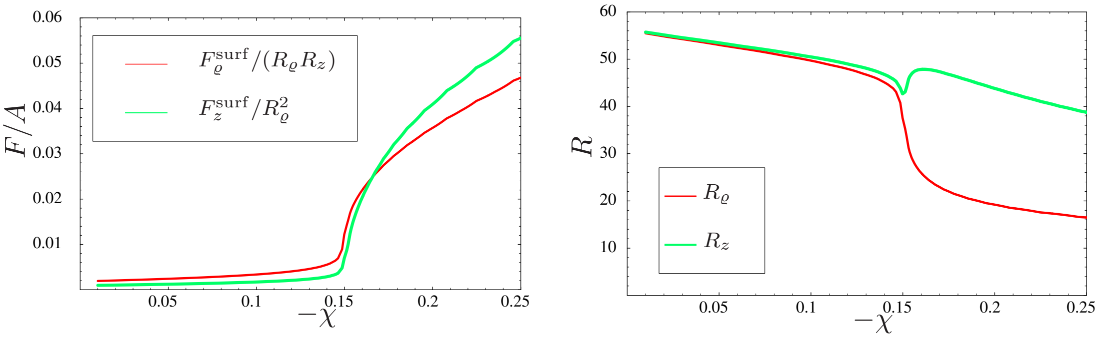

Figure 8.33: $F_\varrho^{\mathrm{surf}}/(R_\varrho R_z)$ and $F_z^{\mathrm{surf}}/(R_\varrho^2)$ plotted as functions of χ for $\sigma = 10^{-4}$, $N = 9.5 \cdot 10^3$ and $\epsilon = g = 0$.

to liquid-crystalline globule occurs. The corresponding extensions of the globule R_ϱ and R_z plotted on the right illustrate the enlargement of the globule in z-direction and the diminution in ϱ-direction in the crossover interval. When the final shape of the liquid-crystalline globule has developed the curves become parallel again and decrease both indicating the further compactification of the entire globule.

The investigations of the surface contributions to the free energy further visualise that it is the anisotropy of the entropic surface energy that drives the system into the nematic state.

8.5. Conclusions

In this section the results presented in the previous sections of Chapter 8 are compared to the literature and some remarks on their relevance to homopolypeptides and proteins are made.

The numerical solutions of the self-consistent field equations show that the rod-coil copolymer with variable composition can form three phase states, open chain, amorphous globule and nematic liquid-crystalline globule with high fraction of stiff segments. The transition between the first two states is similar to the coil-globule transition of a homopolymer. The formation of a liquid-crystalline globular state without explicit alignment interaction between the rods is a novel result and deserves further discussion.

Nematic liquid-crystalline phases in melts of rod-coil diblocks with fixed composition have been discussed theoretically in [85]. Also semiflexible polymers are able to form liquid-crystalline phases, see for instance [86–88]. The isotropic to nematic transition in multicomponent liquid-crystalline polymers has been discussed in [46]. A detailed review of early results concerning melts and solution of liquid-crystalline polymers can be found in [89]. In all these approaches the transition into an ordered nematic state is driven by an explicit angle-dependent alignment interaction.

The formation of a liquid-crystalline globule from a rod-coil multiblock copolymer with fixed composition has been discussed in an early theoretical work [38]. Phase states similar to the ones summarised in the phase diagram in Fig.(8.24) are seen in [90], where the authors consider a homopolymer in which each monomer carries a dipole moment and take into account explicit dipole-dipole interactions. However, the schematic phase diagram in [90] has been considered within the so-called volume approximation where the contribution of the surface energy can be neglected (at $N \to \infty$) [8] and the transition into the anisotropic globular state with nematic order is driven by dipole-dipole interactions.

In an early work [91] a cooperative helix-coil liquid-crystal transition was found, very similar to the transition from amorphous to liquid-crystalline globule discussed here. The formation of nematic order is also accompanied by a strong increase in fraction of stiff (or helical) segments. The main difference is again that the transition is driven by an explicit alignment interaction of Maier-Saupe type similar to the additional interaction ($g < 0$) considered in Section 8.4.4 and not by the entropic surface tension anisotropy.

In the context of secondary and tertiary structure formation in proteins the interplay of helix formation and liquid-crystalline order has been studied, see for instance [92, 93]. It was shown that liquid-crystalline ordering enhances the number of helical segments as well as the average length of the helices which is qualitatively similar to the results of the model presented here. This indicates that the model of a rod-coil multiblock copolymer with variable composition might be a good candidate to give a simple explanation for the formation of helix bundles in certain globular proteins. Both, simulations [60] and experiments [61] show that proteins can adopt not only the native state and completely denatured state (open chain) but also so-called premolten and molten globular states. For helix-bundle proteins the premolten globule, which does not show any order of the helices, corresponds to the amorphous globule in this model. The molten globule with ordered helices but without native contacts (and therefore also without the characteristic helix-helix angle found in the native state) corresponds to the liquid-crystalline globule. The model also shows that during the transition to a liquid-crystalline globule not only the amount of helical segments increases strongly but the globule also becomes more compact. The experimentally observed [79] correlation between the amount of secondary structure elements and compactness of proteins mentioned in Section 6.1 might therefore also be explained by this transition, at least in the case of helix bundle proteins.

Irrespective of the possible application to helix bundle formation in proteins, this model provides a relatively simple example of the general interplay between secondary structure (helices or stiff rods) and tertiary structure (liquid-crystalline order) in homopolypeptides.

9. Final conclusions and outlook

Two very different methods to theoretically treat rod-coil copolymers are discussed in this thesis, scaling methods and field theory. Copolymers with fixed composition of stiff and flexible parts are studied by means of scaling considerations. The equilibrium structures they form in a selective solvent are investigated, as well as their behaviour under tension due to an applied force. The adsorption behaviour of rod-coil diblocks to an attractive surface is investigated in a quasi two-dimensional approximation. The problem of copolymers with a variable composition of stiff and flexible segments is treated using a self-consistent field theory. The formation of amorphous and liquid-crystalline globules is observed and their influence on the composition of the copolymer is studied. It is found that the combination of scaling arguments and field theory provides a good understanding of the basic features of structure formation and self assembly of rod-coil copolymers in solution.

Immersed in a solvent which is poor for the rods and good or Θ-like for the coils, the systems with fixed composition form cylindrical micelles. The micelles are formed because the rods tend to aggregate in order to minimise their contact with the solvent and gain energy. This process is counterbalanced by the loss of entropy of the flexible coils. In equilibrium this leads to a structure of either one cylindrical micelle with two coronas formed by the coils or several connected micelles. The average aggregation number of the rods as well as the average number of micelles is calculated in Chapter 3. For the calculation of the latter it is assumed that all the micelles are of the same size. The number of micelles is mainly governed by the surface energy. For large surface energies the formation of only one micelle is favoured. If the surface energy is lower the system can adopt multi-micelle configurations. The results of Chapter 3 describe the structure a rod-coil multiblock copolymer adopts in selective solvent in a quantitative manner. This is certainly of interest for the study of synthetic systems. It is shown that the system might even serve as a very simple model to describe helical proteins. For different classes of helix bundle proteins the results provide a reasonable estimate for the number of helices in the bundle. Although the model is very simple, the right trend can be predicted for proteins with larger or smaller bundles.

For future considerations the simple scaling model could be extended by introducing different rod lengths within one multiblock. The aggregation of rods might then be sensitive to rod length in order to minimise the defect energy due to the mismatch of rods of different lengths. Also multi-micelle configurations in which rods of different lengths prefer to aggregate in different micelles are conceivable. It would then be natural to consider configurations with micelles of different size (i.e. aggregation number). To increase the applicability of the model to proteins it would be of interest to consider special geometrical shapes of the rods (for instance chiral ones) to model the characteristic angle between the helices which can be observed in bundles. This might then also lead to the possibility of a twisted phase in which the rods are not aligned parallel but are regularly twisted with respect to each other around their midpoint. For cylindrical rods this phase is energetically not stable.

Chapter 4 discusses how a rod-coil multiblock, that forms one micelle, unfolds under an external force. For simplicity it is assumed that the micelle is ordered in such a way that it is always possible to pull out the rods one after another from the outer shell of the micelle. The scaling approach used in Chapter 4 is only valid in equilibrium which corresponds to quasi static pulling. For this scenario it is shown that with increasing force it is energetically favourable to pull out one rod completely rather than to shift the rod slightly with respect to the other rods in the micelle. The unfolding is therefore a stepwise process. Assuming Θ-solvent conditions for the coils, it is possible to calculate the critical force at which this happens for each rod. It turns out that for parameters which are physically reasonable thermal fluctuations are very likely to dominate the energy barriers between the removal of individual rods. The unfolding process then turns into a one-step process showing one large plateau in the force-extension curve. In this case the assumption of an ordered micelle could be released since at a certain force the entire micelle unfolds at once anyway.

These considerations could also be extended to multi-micelle configurations and systems with different rod lengths within one multiblock. In this case micelles containing shorter rods might unfold at lower forces than the ones containing longer rods which would lead to a more complex force-extension curve showing several plateaus.

The adsorption behaviour of an aggregate of individual rod-coil diblocks is investigated in Chapter 5. It is assumed that the rods align only parallel to each other. A quasi two-dimensional approximation is considered in which the width of the system is equal to the rod diameter. It is shown that, within a certain range of parameters, the rods in an adsorbed aggregate shift with respect to each other so that their ends are not aligned to allow the chains to gain entropy. For small shifts (smaller than the splay of the chains) the shift profile is calculated. The stability of the adsorbed aggregate is discussed and its free energy is compared to the free energy of the other possible configurations, a mushroom (the aggregate adsorbs with the rods perpendicular to the surface), a configuration with only one rod adsorbed at the surface whereas the others form a free aggregate and a complete dissociation of the aggregate which leads to the adsorption of the individual rods at the surface. For a certain combination of parameters, a phase diagram of the configurations in L-N space is plotted.

The quasi two-dimensional approach is a very simplified model. To gain further insight a three-dimensional model of a cylindrical micelle formed by rod-coil diblocks should be constructed. The adsorbed micelle is expected to adopt a shape similar to a semicylinder. The profile of the shift is then expected to form a two-dimensional surface with the innermost rods close to the surface showing the maximum shift. The region of stability for such a finite three-dimensional aggregate is expected to be larger than the one for the quasi two-dimensional model which alters the phase diagram of possible configurations. It would also be of interest to study aggregates with other geometries or to study the adsorption behaviour of the multiblock copolymer micelles introduced in Chapter 3.

In Chapters 6-8 a rod-coil multiblock with a variable composition of stiff and flexible segments is investigated using self-consistent field theory. The system can undergo a coil-globule transition very similar to that of a homopolymer with almost no change in composition (for zero energy gain per stiff segment and zero cooperativity). If in the globular regime the energy gain ϵ per stiff segments is increased, the fraction of stiff segments Θ_{R} increases in a similar way as in the one-dimensional Zimm-Bragg type models of the helix-coil transition (although less strongly). At a certain fraction of stiff segments the stiffening of the polymer drives it into the open chain regime. The main result of these investigations is the finding of an additional crossover transition from an amorphous to a liquid-crystalline globule when a selective two-body interaction (χ) is switched on. The transition occurs even without explicit alignment interaction between the stiff segments. It is triggered by an interplay between anisotropic surface energy (which is of entropic origin) and bulk interaction energy. The transition coincides with a rapid increase in the fraction of stiff segments. It is shown that an attractive alignment interaction enhances this transition and shifts the transition point to lower values of $|\chi|$, whereas a repulsive one can suppress the formation of a liquid-crystalline globule without a significant change of the strong increase in Θ_{R}. Since the crossover to a liquid-crystalline globule is driven by the anisotropic surface energy, it gets sharper for shorter polymers and eventually vanishes in the limit of infinite chain length. The crossover is also sensitive to cooperativity. It gets sharper with increasing cooperativity and occurs at smaller values of $|\chi|$. An increasing energy gain per stiff segment increases the fraction of stiff segments at a given χ and therefore shifts the transition point to smaller values of $|\chi|$. For high enough ϵ the transition point of the amorphous to liquid-crystalline transition coincides with the one of the coil-globule transition. These findings are summarised in a phase diagram of the copolymer in ϵ-χ space. The switching of individual segments from stiff to flexible and the cooperativity of this behaviour can be related to the helix-coil transition. The transition to a liquid-crystalline globule with nematic order can be related to the molten globule state of helical proteins and might explain bundle formation. Since this transition increases the fraction of stiff segments and also further compactifies the globule, it might also provide a rather simple physical explanation of the correlation between the amount of secondary structure elements and compactness of proteins [79] in the case of helix bundle proteins.

There are many possibilities to further improve this model. Instead of using the expansion of ψ in Legendre polynomials, the full orientation dependence could be accounted for. However, this would significantly complicate the numerical problem, since it would involve solving integro-differential equations. A final attempt would be to go beyond the mean-field character of the self-consistent field theory. This would permit the study of the effect of fluctuations and the investigation of the open chain regime. A possible extension of the model would be the introduction of specific angle dependent interactions to model the characteristic tilting angle between helices in bundles.

A further general question which could be addressed is the effect of a selective solvent which is good for the rods and poor for the flexible coils. This would lead to the formation of completely different structures as the ones discussed in this thesis. Copolymers of alternating flexible parts and semiflexible parts of high stiffness under such solvent conditions have been studied computationally [94] and it has been suggested that they form lattice like structures, where the nodes are formed by the collapsed flexible parts and the links by the stiff parts. Another interesting area for further studies would be to impose a primary structure in terms of a sequence on the polymer chain. The polymer would then consist of a specific sequence of hydrophobic (H) and hydrophilic (P) segments. In this case the three-dimensional structure of the globule becomes sequence dependent. A specific sequence on the individual rods could lead to the formation of, for instance, twisted regimes and other structures different from aggregates in which the rods are simply aligned parallel. The force-extension curve of such a HP polymer can be used to read its sequence [95]. Another interesting question would be to study the adsorption behaviour of a HP rod-coil copolymer onto a patterned (partially attractive and partially repulsive) surface. For a flexible polymer this was done using a variational method [96]. A first attempt might be to study the adsorption of a single HP rod on a patterned surface.

A. Field theoretical representation of the partition function

In this appendix the grand canonical partition function represented in terms of a n-component field theory in the limit $n \to 0$ is derived.

As a start, the canonical partition function given by Eq.(6.11) is rewritten by introducing the collective coil, rod and orientation densities $\rho_{\mathrm{C}}(\mathbf{r})$, $\rho_{\mathrm{R}}(\mathbf{r})$ and $S^{ij}(\mathbf{r})$ respectively via δ-functions.

$$\begin{aligned}
Z(\{N_n\}, K) \;=\; & \int \mathcal{D}\rho_{\mathrm{C}}(\mathbf{r}) \int \mathcal{D}\rho_{\mathrm{R}}(\mathbf{r}) \int \mathcal{D}S^{ij}(\mathbf{r}) \int \prod_{n=1}^{K} D\mathbf{r}_n(s)\, \mathrm{d}^3R_n\, \mathrm{d}^2u_n \\
\times\; & \delta(\rho_{\mathrm{C}}(\mathbf{r}) - \hat{\rho}_{\mathrm{C}}(\mathbf{r}))\delta(\rho_{\mathrm{R}}(\mathbf{r}) - \hat{\rho}_{\mathrm{R}}(\mathbf{r}))\delta(S^{ij}(\mathbf{r}) - \hat{S}^{ij}(\mathbf{r})) \\
\times\; & \delta(|\mathbf{u}_n| - 1)\delta(\mathbf{r}_n(f_nN_n) - \mathbf{R}_n) \exp\left\{ -\frac{3}{2b^2} \int_0^{f_nN_n} \mathrm{d}s \left(\frac{\partial \mathbf{r}_n}{\partial s} \right)^2 \right\} \\
\times\; & \exp\left\{ -\chi \int \mathrm{d}^3r\, \rho_{\mathrm{R}}(\mathbf{r})\rho_{\mathrm{R}}(\mathbf{r}) - \frac{v}{2} \int \mathrm{d}^3r\, [\rho_{\mathrm{C}}(\mathbf{r}) + \rho_{\mathrm{R}}(\mathbf{r})]^2 \right. \\
-\; & \left. \frac{w}{3!} \int \mathrm{d}^3r\, [\rho_{\mathrm{C}}(\mathbf{r}) + \rho_{\mathrm{R}}(\mathbf{r})]^3 - g \int \mathrm{d}^3r\, \mathrm{Tr}\left[S^{ij}(\mathbf{r})S^{ij}(\mathbf{r}) \right] \right\} \qquad \text{(A.1)}
\end{aligned}$$

The density δ-functions in Eq.(A.1) can be represented as integrals in the following way

$$\delta(\rho_{\mathrm{C}}(\mathbf{r}) - \hat{\rho}_{\mathrm{C}}(\mathbf{r})) = \int \mathcal{D}h_{\mathrm{C}}(\mathbf{r}) \exp\left\{ i \int \mathrm{d}^3r\, h_{\mathrm{C}}(\mathbf{r})[\rho_{\mathrm{C}}(\mathbf{r}) - \hat{\rho}_{\mathrm{C}}(\mathbf{r})] \right\}. \qquad \text{(A.2)}$$

The partition function of the interacting polymer in Eq.(A.1) can then be represented in terms of the partition function $Z^{(0)}$ of a non-interacting polymer in the external fluctuating fields h_{C}, h_{R}, h_S^{ij}.

$$\begin{aligned}
Z(\{N_n\},K) &= \int \mathcal{D}\rho_{\mathrm{C}}(\mathbf{r}) \int \mathcal{D}\rho_{\mathrm{R}}(\mathbf{r}) \int DS^{ij}(\mathbf{r}) \int \mathcal{D}h_{\mathrm{C}}(\mathbf{r}) \int \mathcal{D}h_{\mathrm{R}}(\mathbf{r}) \int Dh_S^{ij}(\mathbf{r}) \\
&\times \exp\Bigg\{ -\chi \int \mathrm{d}^3r\, \rho_{\mathrm{R}}(\mathbf{r})\rho_{\mathrm{R}}(\mathbf{r}) - \frac{v}{2} \int \mathrm{d}^3r\, [\rho_{\mathrm{C}}(\mathbf{r}) + \rho_{\mathrm{R}}(\mathbf{r})]^2 \\
&- \frac{w}{3!} \int \mathrm{d}^3r\, [\rho_{\mathrm{C}}(\mathbf{r}) + \rho_{\mathrm{R}}(\mathbf{r})]^3 - g \int \mathrm{d}^3r\, \mathrm{Tr}\left[S^{ij}(\mathbf{r})S^{ij}(\mathbf{r})\right] \\
&+ i \int \mathrm{d}^3r\, \rho_{\mathrm{C}}(\mathbf{r})h_{\mathrm{C}}(\mathbf{r}) + i \int \mathrm{d}^3r\, \rho_{\mathrm{R}}(\mathbf{r})h_{\mathrm{R}}(\mathbf{r}) + i \int \mathrm{d}^3r\, S^{ij}(\mathbf{r})h_S^{ij}(\mathbf{r}) \Bigg\} \\
&\times Z^{(0)}(\{N_n\},K;[h_{\mathrm{C}}],[h_{\mathrm{R}}],\left[h_S^{ij}\right]) \qquad \text{(A.3)}
\end{aligned}$$

The partition function $Z^{(0)}$ of the non-interacting system in the external fields is given by

$$\begin{aligned}
&Z^{(0)}(\{N_n\},K;[h_{\mathrm{C}}],[h_{\mathrm{R}}],\left[h_S^{ij}\right]) \\
&= \int \prod_{n=1}^{K} \mathcal{D}\mathbf{r}_n(s)\, \mathrm{d}^3R_n\, \mathrm{d}^2u_n\, \delta(|\mathbf{u}_n|-1)\delta(\mathbf{r}_n(f_nN_n)-\mathbf{R}_n) \\
&\times \exp\Bigg\{ -\frac{3}{2b^2}\int_0^{f_nN_n} \mathrm{d}s \left(\frac{\partial \mathbf{r}_n}{\partial s}\right)^2 - i\int_0^{f_nN_n} \mathrm{d}s\, h_{\mathrm{C}}(\mathbf{r}_n(s)) \\
&- i\int_0^{(1-f_n)N_n} \mathrm{d}s\, h_{\mathrm{R}}(\mathbf{R}_n+\mathbf{u}_ns) \\
&- i\int_0^{(1-f_n)N_n} \mathrm{d}s\, h_S^{ij}(\mathbf{R}_n+\mathbf{u}_ns)\left(u_n^iu_n^j - \frac{1}{3}\delta^{ij}\right) \Bigg\}. \qquad \text{(A.4)}
\end{aligned}$$

The grand canonical partition function $Z^{(0)}(\mu,\epsilon,\sigma;[h_{\mathrm{C}}],[h_{\mathrm{R}}],\left[h_S^{ij}\right])$ of the non-interacting system in the external fields can be derived by using the polymeric correlation function.

$$Z^{(0)}(\mu,\epsilon,\sigma;[h_{\mathrm{C}}],[h_{\mathrm{R}}],\left[h_S^{ij}\right]) = \int \mathrm{d}1\mathrm{d}1'\, \Xi^{(0)}(1,1';\mu,\epsilon,\sigma;[h_{\mathrm{C}}],[h_{\mathrm{R}}],\left[h_S^{ij}\right]), \qquad \text{(A.5)}$$

where the grand canonical polymeric correlation function $\Xi^{(0)}(1,1';\mu,\epsilon,\sigma;[h_{\mathrm{C}}],[h_{\mathrm{R}}],\left[h_S^{ij}\right])$ gives the unnormalised probability of finding the first segments of the copolymer with variable composition at the coordinate 1 and the last segment at $1'$. 1 stands either for $(\mathbf{r}_1)$ or for $(\mathbf{r}_1,\mathbf{u}_1)$ depending on whether the first segment is a flexible one or a stiff one. The same applies for the coordinate

$1'$ of the last segment. The polymeric correlation function is therefore the partition function of the copolymer with variable composition for ends fixed at 1 and $1'$. In the following, $\Xi^{(0)}(1, 1'; \mu, \epsilon, \sigma; [h_{\mathrm{C}}], [h_{\mathrm{R}}], [h_S^{ij}])$ will be represented in terms of a gaussian two dimensional path integral over the field φ associated with the flexible segments and the field ψ associated with the stiff segments, see Eq.(A.26). It will be shown, that this path integral equals a geometric progression of convoluted rod and coil Green function operators, see Eq.(A.29). Note, that the path integral is gaussian, because at this stage it represents the polymeric correlation function of the non-interacting system.

A.1. Coil Green function

First, the inverse Green function operator for one non-interacting flexible part which is modelled by a Gaussian chain with M_{C} segments of segment length b in the external field $ih_{\mathrm{C}}(\mathbf{r})$ is derived, compare to e.g. [10, 49]. The Green function of a chain of length M_{C} with the end points at positions $\mathbf{R}'$ and $\mathbf{R}$ in the external field $ih_{\mathrm{C}}(\mathbf{r})$ is defined as follows

$$G_{\mathrm{coil}}(\mathbf{R}-\mathbf{R}'; M_{\mathrm{C}}) \equiv \frac{\displaystyle\int_{\mathbf{R}'}^{\mathbf{R}} \mathcal{D}\mathbf{r}(s) \exp\left\{-\frac{3}{2b^2}\int_0^{M_{\mathrm{C}}} \mathrm{d}s \left[\left(\frac{\partial \mathbf{r}}{\partial s}\right)^2 + ih_{\mathrm{C}}(\mathbf{r})\right]\right\}}{\displaystyle\int \mathrm{d}^3R'\,\mathrm{d}^3R \int_{\mathbf{R}'}^{\mathbf{R}} \mathcal{D}\mathbf{r}(s) \exp\left\{-\frac{3}{2b^2}\int_0^{M_{\mathrm{C}}} \mathrm{d}s \left(\frac{\partial \mathbf{r}}{\partial s}\right)^2\right\}}. \tag{A.6}$$

The Green function gives the probability of finding the end points at $\mathbf{R}'$ and $\mathbf{R}$ of the chain in the external field $ih_{\mathrm{C}}(\mathbf{r})$. For $h = 0$ the Green function reduces to the Gaussian probability distribution function, compare to Eq.(2.4) in Section 2.1

$$G^{(0)}_{\mathrm{coil}}(\mathbf{R}-\mathbf{R}'; M_{\mathrm{C}}) = \left(\frac{3}{2\pi M_{\mathrm{C}} b^2}\right)^{3/2} \exp\left(-\frac{3(\mathbf{R}-\mathbf{R}')^2}{2M_{\mathrm{C}} b^2}\right). \tag{A.7}$$

Now an equation of motion for $G_{\mathrm{coil}}(\mathbf{R}-\mathbf{R}'; M_{\mathrm{C}})$ is derived. It can be seen from the definition of the Green function in Eq.(A.6) that the following identity holds

$$G_{\mathrm{coil}}(\mathbf{R}-\mathbf{R}'; M_{\mathrm{C}}+\Delta M_{\mathrm{C}}) = \int \mathrm{d}^3R''\, G_{\mathrm{coil}}(\mathbf{R}-\mathbf{R}''; \Delta M_{\mathrm{C}}) G_{\mathrm{coil}}(\mathbf{R}''-\mathbf{R}'; M_{\mathrm{C}}). \tag{A.8}$$

Suppose ΔM_{C} is small. For $M_{\mathrm{C}} < s < M_{\mathrm{C}}+\Delta M_{\mathrm{C}}$, $\mathbf{r}(s)$ is then close to $\mathbf{R}$. Hence, if $h(\mathbf{r})$ is a smooth function, the integral over the external field ih in the small interval can be approximated as

$$i\int_{M_{\mathrm{C}}}^{M_{\mathrm{C}}+\Delta M_{\mathrm{C}}} \mathrm{d}s\, h(\mathbf{r}(s)) \approx i\Delta M_{\mathrm{C}} h(\mathbf{R}). \tag{A.9}$$

With this approximation $G_{\mathrm{coil}}(\mathbf{R}-\mathbf{R}''; \Delta M_{\mathrm{C}})$ can be obtained from Eq.(A.6)

$$G_{\mathrm{coil}}(\mathbf{R}-\mathbf{R}''; \Delta M_{\mathrm{C}}) = \exp(-i\Delta M_{\mathrm{C}} h(\mathbf{R})) G^{(0)}_{\mathrm{coil}}(\mathbf{R}-\mathbf{R}''; \Delta M_{\mathrm{C}}). \tag{A.10}$$

Eqs.(A.8, A.10) yield

$$\begin{aligned} G_{\mathrm{coil}}(\mathbf{R}-\mathbf{R}'; M_{\mathrm{C}}+\Delta M_{\mathrm{C}}) &= \exp(-i\Delta M_{\mathrm{C}} h(\mathbf{R})) \\ &\times \int \mathrm{d}^3R''\, G^{(0)}_{\mathrm{coil}}(\mathbf{R}-\mathbf{R}''; \Delta M_{\mathrm{C}}) G_{\mathrm{coil}}(\mathbf{R}''-\mathbf{R}'; M_{\mathrm{C}}). \end{aligned} \tag{A.11}$$

For small ΔM_{C}, $G^{(0)}_{\mathrm{coil}}(\mathbf{R}-\mathbf{R}''; \Delta M_{\mathrm{C}})$ has a sharp peak at $\mathbf{R}=\mathbf{R}''$. The integral in Eq.(A.11) can therefore be evaluated by expanding $G_{\mathrm{coil}}(\mathbf{R}''-\mathbf{R}'; M_{\mathrm{C}})$ with respect to $\mathbf{x}=\mathbf{R}-\mathbf{R}''$

$$\begin{aligned} I &= \int \mathrm{d}^3R''\, G^{(0)}_{\mathrm{coil}}(\mathbf{R}-\mathbf{R}''; \Delta M_{\mathrm{C}}) G_{\mathrm{coil}}(\mathbf{R}''-\mathbf{R}'; M_{\mathrm{C}}) \\ &= \int \mathrm{d}^3x\, G^{(0)}_{\mathrm{coil}}(\mathbf{x}; \Delta M_{\mathrm{C}}) G_{\mathrm{coil}}(\mathbf{R}-\mathbf{x}-\mathbf{R}'; M_{\mathrm{C}}) \\ &= \int \mathrm{d}^3x\, G^{(0)}_{\mathrm{coil}}(\mathbf{x}; \Delta M_{\mathrm{C}}) \left(1 - x_\alpha \frac{\partial}{\partial R_\alpha} + \frac{1}{2} x_\alpha x_\beta \frac{\partial^2}{\partial R_\alpha \partial R_\beta}\right) \\ &\times\ G_{\mathrm{coil}}(\mathbf{R}-\mathbf{R}'; M_{\mathrm{C}}). \end{aligned} \tag{A.12}$$

From Eq.(A.7) can be seen that

$$\begin{gathered} \int \mathrm{d}^3x\, G^{(0)}_{\mathrm{coil}}(\mathbf{x}; \Delta M_{\mathrm{C}}) x_\alpha = 0, \\ \int \mathrm{d}^3x\, G^{(0)}_{\mathrm{coil}}(\mathbf{x}; \Delta M_{\mathrm{C}}) x_\alpha x_\beta = \Delta M_{\mathrm{C}} \frac{b^2}{3} \delta_{\alpha\beta}. \end{gathered} \tag{A.13}$$

Therewith the integral I becomes

$$I = \left(1 + \frac{\Delta M_{\mathrm{C}} b^2}{6} \nabla^2_R\right) G_{\mathrm{coil}}(\mathbf{R}-\mathbf{R}'; M_{\mathrm{C}}). \tag{A.14}$$

To linear order in ΔM_C, Eq.(A.11) can now be written as

$$\begin{aligned}\left(1+\Delta M_\mathrm{C}\frac{\partial}{\partial M_\mathrm{C}}\right)G_\mathrm{coil}(\mathbf{R}-\mathbf{R}';M_\mathrm{C}) &= (1-i\Delta M_\mathrm{C}h(\mathbf{R})) \\ &\times \left(1+\frac{\Delta M_\mathrm{C}b^2}{6}\nabla_R^2\right)G_\mathrm{coil}(\mathbf{R}-\mathbf{R}';M_\mathrm{C}).\end{aligned} \tag{A.15}$$

Comparing all terms linear in ΔM_C gives the equation of motion for the coil Green function

$$\left[\frac{\partial}{\partial M_\mathrm{C}}-\frac{b^2}{6}\nabla_R^2+V(\mathbf{R})\right]G_\mathrm{coil}(\mathbf{R}-\mathbf{R}';M_\mathrm{C})=\delta(M_\mathrm{C})\delta(\mathbf{R}-\mathbf{R}'), \tag{A.16}$$

where the δ-functions account for the singularity at $M_\mathrm{C}=0$ and $\mathbf{R}=\mathbf{R}'$. Employing the standard Laplace transformation with respect to M_C yields the grand canonical Green function $G_\mathrm{coil}(\mathbf{R}-\mathbf{R}';\mu)$

$$G_\mathrm{coil}(\mathbf{R}-\mathbf{R}';\mu)=\int_0^\infty dM_\mathrm{C}\,G_\mathrm{coil}(\mathbf{R}-\mathbf{R}';M_\mathrm{C})e^{-\beta\mu M_\mathrm{C}}. \tag{A.17}$$

The inverse Green function operator $\widehat{G}_\mathrm{coil}^{-1}$ in the external field $ih_\mathrm{C}(\mathbf{r})$ is then given by

$$\widehat{G}_\mathrm{coil}^{-1}=\delta(\mathbf{r}-\mathbf{r}')\left(\beta\mu-\frac{b^2}{6}\nabla_r^2+ih_\mathrm{C}(\mathbf{r})\right). \tag{A.18}$$

A.2. Rod Green function

Now the Green function for one rod with the number of segments M_R of segment length b with the start point $\mathbf{R}$ and the end point $\mathbf{R}'$ in an external field is derived. The length of the rod is given by $L_\mathrm{R}=bM_\mathrm{R}$. The rods are assumed to have no chirality and the rod Green function should therefore be invariant with respect to flip $\mathbf{u}\to-\mathbf{u}$.

A suitably symmetric Green function can be constructed as follows

$$G_\mathrm{rod}(\mathbf{R}-\mathbf{R}';\mathbf{u};M_\mathrm{R})=\frac{1}{2}\left[\delta(\mathbf{R}-\mathbf{R}'-\mathbf{u}bM_\mathrm{R})+\delta(\mathbf{R}-\mathbf{R}'+\mathbf{u}bM_\mathrm{R})\right]. \tag{A.19}$$

Fourier transformation with respect to $\mathbf{R}-\mathbf{R}'$ yields the Green function in k-space

$$G_{\mathrm{rod}}(\mathbf{k};\mathbf{u};M_{\mathrm{R}}) = \frac{1}{2}\left[e^{ib\mathbf{u}\cdot\mathbf{k}\,M_{\mathrm{R}}} + e^{-ib\mathbf{u}\cdot\mathbf{k}\,M_{\mathrm{R}}}\right] = \cos(b\mathbf{u}\cdot\mathbf{k}M_{\mathrm{R}}). \tag{A.20}$$

The Laplace transformation has to be applied to calculate the grand canonical Green function in k-space.

$$\begin{aligned} G_{\mathrm{rod}}(\mathbf{k};\mathbf{u};\mu-\epsilon) &= \frac{1}{2}\left\{\int_0^\infty dM_{\mathrm{R}} e^{-[\beta(\mu-\epsilon)+ib\mathbf{u}\cdot\mathbf{k}]M_{\mathrm{R}}} + \int_0^\infty dM_{\mathrm{R}} e^{-[\beta(\mu-\epsilon)-ib\mathbf{u}\cdot\mathbf{k}]M_{\mathrm{R}}}\right\} \\ &= \frac{1}{2}\left\{\frac{1}{\beta(\mu-\epsilon)+ib\mathbf{u}\cdot\mathbf{k}} + \frac{1}{\beta(\mu-\epsilon)-ib\mathbf{u}\cdot\mathbf{k}}\right\} \\ &= \frac{\mu-\epsilon}{\beta^2(\mu-\epsilon)^2+b^2(\mathbf{u}\cdot\mathbf{k})^2}, \end{aligned} \tag{A.21}$$

where ϵ quantifies the energy gain due to formation of a stiff segment compared to a flexible one. The inverse Green function operator in k-space is then simply given by

$$\widehat{G}^{-1}_{\mathrm{rod},\mathbf{k}} = \beta(\mu-\epsilon) + \frac{b^2(\mathbf{u}\cdot\mathbf{k})^2}{\beta(\mu-\epsilon)}. \tag{A.22}$$

The corresponding equation of motion for the rod Green function G_{rod} takes the form

$$\left[\beta(\mu-\epsilon) + \frac{b^2(\mathbf{u}\cdot\mathbf{k})^2}{\beta(\mu-\epsilon)}\right] G_{\mathrm{rod}}(\mathbf{k};\mathbf{u};\mu-\epsilon) = 1. \tag{A.23}$$

In real space the equation of motion is given by

$$\left[\beta(\mu-\epsilon) - \frac{b^2(\mathbf{u}\cdot\nabla_R)^2}{\beta(\mu-\epsilon)}\right] G_{\mathrm{rod}}(\mathbf{R}-\mathbf{R}';\mathbf{u};\mu-\epsilon) = \delta(\mathbf{R}-\mathbf{R}'). \tag{A.24}$$

The external field that acts on the rod has to be taken into account. According to Eq.(A.4) the rod is moving in the external field $ih_{\mathrm{R}}(\mathbf{r})+i\overleftrightarrow{h}_S(\mathbf{r}):\overleftrightarrow{P}$, where the tensor $\overleftrightarrow{P}$ is given by $P^{ij}\equiv u^iu^j-\delta^{ij}/3$. The resulting inverse Green function operator reads

$$\widehat{G}^{-1}_{\mathrm{rod}} = \delta(\mathbf{r}-\mathbf{r}')\left(\beta(\mu-\epsilon) - \frac{b^2(\mathbf{u}\cdot\nabla_{\mathrm{R}})^2}{\beta(\mu-\epsilon)} + ih_{\mathrm{R}}(\mathbf{r}) + i\overleftrightarrow{h}_S(\mathbf{r}):\overleftrightarrow{P}\right). \tag{A.25}$$

A.3. Field theoretic representation

Knowing the inverse Green function operators the grand canonical polymeric correlation function can now be represented as the following Gaussian 2-dimensional path integral

$$\begin{aligned}\Xi^{(0)}(1,1';\mu,\epsilon,\sigma;[h_{\mathrm{C}}],[h_{\mathrm{R}}],\left[h_S^{ij}\right]) = \frac{1}{\Theta}\int \mathcal{D}\psi\mathcal{D}\varphi\,\psi(1)\,\varphi(1') \\ \times\exp\left\{-\frac{1}{2}\int \mathrm{d}3\,\mathrm{d}4 \begin{pmatrix}\psi(3)\\ \varphi(3)\end{pmatrix}^{\mathsf{T}} \begin{pmatrix}\widehat{G}^{-1}_{\mathrm{rod}} & -\sigma^{1/2}\\ -\sigma^{1/2} & \widehat{G}^{-1}_{\mathrm{coil}}\end{pmatrix} \begin{pmatrix}\psi(4)\\ \varphi(4)\end{pmatrix}\right\},\end{aligned} \tag{A.26}$$

where

$$\Theta = \int \mathcal{D}\psi\mathcal{D}\varphi\exp\left\{-\frac{1}{2}\int \mathrm{d}3\,\mathrm{d}4 \begin{pmatrix}\psi(3)\\ \varphi(3)\end{pmatrix}^{\mathsf{T}} \begin{pmatrix}\widehat{G}^{-1}_{\mathrm{rod}} & -\sigma^{1/2}\\ -\sigma^{1/2} & \widehat{G}^{-1}_{\mathrm{coil}}\end{pmatrix} \begin{pmatrix}\psi(4)\\ \varphi(4)\end{pmatrix}\right\}. \tag{A.27}$$

The choice of $\psi(1)\,\varphi(1')$ under the path integral yields one rod-coil unit as a basic building block, see Fig.(A.1) and Eq.(A.29). This choice assigns the coordinates (1) and (1′) to $(\mathbf{r},\mathbf{u})$ and $(\mathbf{r}')$ respectively. Similarly, (3), (4) is a shorthand notation for $(\mathbf{r}_3,\mathbf{u}_3)$, $(\mathbf{r}_4,\mathbf{u}_4)$.

The inversion of the 2×2-matrix in Eq.(A.26) reads

$$\begin{pmatrix}\widehat{G}^{-1}_{\mathrm{rod}} & -\sigma^{1/2}\\ -\sigma^{1/2} & \widehat{G}^{-1}_{\mathrm{coil}}\end{pmatrix}^{-1} = \frac{1}{\widehat{G}^{-1}_{\mathrm{rod}} * \widehat{G}^{-1}_{\mathrm{coil}} - \sigma}\begin{pmatrix}\widehat{G}^{-1}_{\mathrm{coil}} & \sigma^{1/2}\\ \sigma^{1/2} & \widehat{G}^{-1}_{\mathrm{rod}}\end{pmatrix}. \tag{A.28}$$

The calculation of the path integral in Eq.(A.26) yields the following result

$$\begin{aligned}\Xi^{(0)}(1,1';\mu,\epsilon,\sigma;[h_{\mathrm{C}}],[h_{\mathrm{R}}],\left[h_S^{ij}\right]) &= \frac{\sigma^{1/2}}{\widehat{G}^{-1}_{\mathrm{rod}} * \widehat{G}^{-1}_{\mathrm{coil}} - \sigma}\\ &= \sigma^{1/2}\widehat{G}_{\mathrm{rod}} * \widehat{G}_{\mathrm{coil}} * \Big[\widehat{1} + \sigma\widehat{G}_{\mathrm{rod}} * \widehat{G}_{\mathrm{coil}}\\ &+ \sigma^2\widehat{G}_{\mathrm{rod}} * \widehat{G}_{\mathrm{coil}} * \widehat{G}_{\mathrm{rod}} * \widehat{G}_{\mathrm{coil}} + \dots\Big].\end{aligned} \tag{A.29}$$

The asterisk in Eq.(A.29) is a shorthand notation for a convolution of Green function operators. The geometric progression with a convolution as a binary relation has a clear pictorial representation, see Fig.(A.1). The first term of this series has the

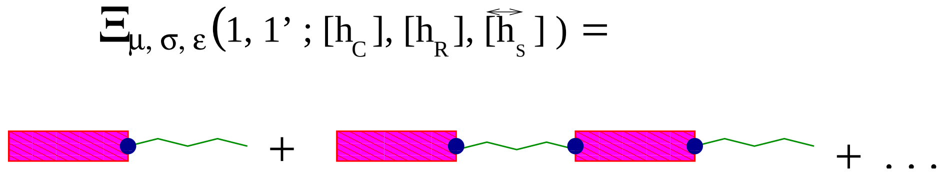

Figure A.1: Pictorial representation of the geometric progression in Eq.(A.29). One rod-coil unit constitutes the basic building block.

analytical expression $\sigma^{1/2}\widehat{G}_{\rm rod} * \widehat{G}_{\rm coil}$, whereas the ratio is equal to $\sigma\widehat{G}_{\rm rod} * \widehat{G}_{\rm coil}$, see also Fig.(A.2). The first term represents one rod-coil unit with one junction between rod and coil, hence the factor $\sigma^{1/2}$. If an additional building block is added, two more junctions are created, hence the factor σ in the ratio. This series gives a correct representation of the grand canonical polymeric correlation function.

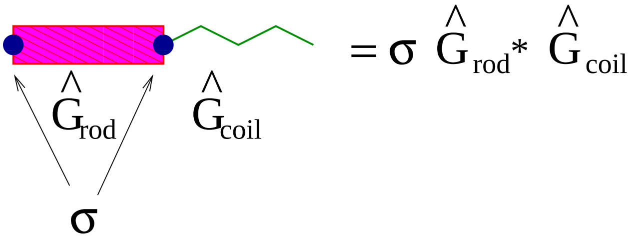

Figure A.2: Pictorial representation of the series ratio in Eq.(A.29): each bar (rod), zigzag line (coil) and fat dot correspond to $\widehat{G}_{\rm rod}, \widehat{G}_{\rm coil}$, and $\sigma^{1/2}$ respectively.

The denominator in Eq.(A.26) can be avoided by introducing de Gennes' $n \to 0$ trick [47, 48]. Consider the two n-component vector fields $\{\psi_\alpha, \varphi_\alpha\}$, where $\alpha = 1, 2, \ldots n$. Then Eq.(A.26) can be formally rewritten as

$$\Xi^{(0)}(1, 1'; \mu, \epsilon, \sigma; [h_{\rm C}], [h_{\rm R}], [h_S^{ij}]) = \lim_{n\to 0} \prod_{\alpha=1}^{n} \int \mathcal{D}\psi_\alpha \mathcal{D}\varphi_\alpha \, \psi_1(1)\, \varphi_1(1') \times \exp\Bigg\{ -\frac{1}{2} \int {\rm d}3{\rm d}4 \sum_{\alpha=1}^{n} \begin{pmatrix} \psi_\alpha(3) \\ \varphi_\alpha(3) \end{pmatrix}^{\sf T} \begin{pmatrix} \widehat{G}^{-1}_{\rm rod} & -\sigma^{1/2} \\ -\sigma^{1/2} & \widehat{G}^{-1}_{\rm coil} \end{pmatrix} \begin{pmatrix} \psi_\alpha(4) \\ \varphi_\alpha(4) \end{pmatrix} \Bigg\}. \tag{A.30}$$

Eq.(A.30) deserves an explanation. It is given by means of a simpler example. Consider the following correlation function

$$\Xi^{(0)}_{\rm s} = \frac{1}{\Theta_{\rm s}} \int \mathcal{D}\varphi \, \varphi(\mathbf{r})\varphi(\mathbf{r}') \exp\left\{ -\frac{1}{2} \int {\rm d}^3 r \, \varphi(\mathbf{r}) \widehat{G}^{-1} \varphi(\mathbf{r}) \right\}, \tag{A.31}$$

where

$$\Theta_{\rm s} = \int \mathcal{D}\varphi \, \exp\left\{ -\frac{1}{2} \int {\rm d}^3 r \, \varphi(\mathbf{r}) \widehat{G}^{-1} \varphi(\mathbf{r}) \right\}. \tag{A.32}$$

The following identity obviously holds

$$\frac{1}{\Theta_{\rm s}} = \lim_{n\to 0} \Theta_{\rm s}^{n-1}. \tag{A.33}$$

$\Theta_{\rm s}^{n-1}$ can be written as

$$\begin{aligned} \Theta_{\rm s}^{n-1} &= \left(\int \mathcal{D}\varphi \, \exp\left\{ -\frac{1}{2} \int {\rm d}^3 r \, \varphi(\mathbf{r}) \widehat{G}^{-1} \varphi(\mathbf{r}) \right\} \right)^{n-1} \\ &= \int \prod_{\alpha=1}^{n-1} \mathcal{D}\varphi_\alpha \, \exp\left\{ -\frac{1}{2} \int {\rm d}^3 r \, \sum_{\alpha=1}^{n-1} \varphi_\alpha(\mathbf{r}) \widehat{G}^{-1} \varphi_\alpha(\mathbf{r}) \right\}. \end{aligned} \tag{A.34}$$

This yields for the correlation function

$$\begin{aligned} \Xi_{\rm s}^{(0)} &= \int \mathcal{D}\varphi \, \varphi(\mathbf{r}) \varphi(\mathbf{r}') \exp\left\{ -\frac{1}{2} \int {\rm d}^3 r \, \varphi(\mathbf{r}) \widehat{G}^{-1} \varphi(\mathbf{r}) \right\} \\ &\times \lim_{n\to 0} \int \prod_{\alpha=1}^{n-1} \mathcal{D}\varphi_\alpha \, \exp\left\{ -\frac{1}{2} \int {\rm d}^3 r \, \sum_{\alpha=1}^{n-1} \varphi_\alpha(\mathbf{r}) \widehat{G}^{-1} \varphi_\alpha(\mathbf{r}) \right\} \\ &= \lim_{n\to 0} \int \prod_{\alpha=1}^{n} \mathcal{D}\varphi_\alpha \, \varphi_1(\mathbf{r}) \varphi_1(\mathbf{r}') \exp\left\{ -\frac{1}{2} \int {\rm d}^3 r \, \sum_{\alpha=1}^{n} \varphi_\alpha(\mathbf{r}) \widehat{G}^{-1} \varphi_\alpha(\mathbf{r}) \right\}. \end{aligned} \tag{A.35}$$

Eq.(A.35) is the equivalent to Eq.(A.30) for the example correlation function $\Xi_{\rm s}^{(0)}$. By taking into account Eq.(A.18) and Eq.(A.25) a more explicit form of $\Xi^{(0)}$ can be obtained from Eq.(A.30).

$$\begin{aligned} &\Xi^{(0)}(1, 1'; \mu, \epsilon, \sigma; [h_{\rm C}], [h_{\rm R}], [h_S^{ij}]) \\ &\quad = \lim_{n\to 0} \prod_{\alpha=1}^{n} \int \mathcal{D}\psi_\alpha \mathcal{D}\varphi_\alpha \, \psi_1(\mathbf{r}, \mathbf{u}) \, \varphi_1(\mathbf{r}') \exp\Bigg\{ -\frac{1}{2} \sum_{\alpha=1}^{n} \int {\rm d}^3 r \, {\rm d}^2 u \\ &\qquad \times \psi_\alpha(\mathbf{r}, \mathbf{u}) \Big[\beta(\mu - \epsilon) - \frac{b^2 \left(\mathbf{u} \cdot \nabla_r\right)^2}{\beta(\mu - \epsilon)} + i h_{\rm R}(\mathbf{r}) + i \overleftrightarrow{h}_S(\mathbf{r}) : \overleftrightarrow{P} \Big] \psi_\alpha(\mathbf{r}, \mathbf{u}) \\ &\qquad - \frac{1}{2} \sum_{\alpha=1}^{n} \int {\rm d}^3 r \, \varphi_\alpha(\mathbf{r}) \Big[\beta\mu - \frac{b^2}{6} \nabla_r^2 + i h_{\rm C}(\mathbf{r}) \Big] \varphi_\alpha(\mathbf{r}) \\ &\qquad + \sigma^{1/2} \sum_{\alpha=1}^{n} \int {\rm d}^3 r \, {\rm d}^2 u \, \psi_\alpha(\mathbf{r}, \mathbf{u}) \varphi_\alpha(\mathbf{r}) \Bigg\} \end{aligned} \tag{A.36}$$

This expression is convenient for the following calculations. Recalling Eqs.(A.3, A.5) the grand canonical partition function of the whole system can be represented in the form

$$\begin{aligned} Z(\mu,\epsilon,\mu_J) &= \int \mathcal{D}\rho_{\mathrm{C}}(\mathbf{r}) \int \mathcal{D}\rho_{\mathrm{R}}(\mathbf{r}) \int \mathcal{D}S^{ij}(\mathbf{r}) \int \mathcal{D}h_{\mathrm{C}}(\mathbf{r}) \int \mathcal{D}h_{\mathrm{R}}(\mathbf{r}) \int Dh_S^{ij}(\mathbf{r}) \\ &\times \exp\left\{ -\chi \int \mathrm{d}^3r\, \rho_{\mathrm{R}}(\mathbf{r})\rho_{\mathrm{R}}(\mathbf{r}) - \frac{v}{2} \int \mathrm{d}^3r \left[\rho_{\mathrm{C}}(\mathbf{r}) + \rho_{\mathrm{R}}(\mathbf{r})\right]^2 \right. \\ &- \frac{w}{3!} \int \mathrm{d}^3r \left[\rho_{\mathrm{C}}(\mathbf{r}) + \rho_{\mathrm{R}}(\mathbf{r})\right]^3 - g \int \mathrm{d}^3r\, \mathrm{Tr}\left[S^{ij}(\mathbf{r}) S^{ij}(\mathbf{r})\right] \\ &+ \left. i \int \mathrm{d}^3r\, \rho_{\mathrm{C}}(\mathbf{r}) h_{\mathrm{C}}(\mathbf{r}) + i \int \mathrm{d}^3r\, \rho_{\mathrm{R}}(\mathbf{r}) h_{\mathrm{R}}(\mathbf{r}) + i \int \mathrm{d}^3r\, S^{ij}(\mathbf{r}) h_S^{ij}(\mathbf{r}) \right\} \\ &\times \int \mathrm{d}1\, \mathrm{d}1'\, \Xi^{(0)}(1,1';\mu,\epsilon,\mu_J;[h_{\mathrm{C}}],[h_{\mathrm{R}}],[h_S^{ij}]). \end{aligned} \tag{A.37}$$

After substitution of Eq.(A.36) into Eq.(A.37) and integration over $h_{\mathrm{C}}(\mathbf{r}), h_{\mathrm{R}}(\mathbf{r})$ and $h_S^{ij}(\mathbf{r})$ a product of three δ-functions appears in the integrand,

$$\begin{aligned} &\delta\left(\rho_{\mathrm{C}}(\mathbf{r}) - \frac{1}{2}\sum_{\alpha=1}^{n} \varphi_\alpha^2(\mathbf{r})\right) \delta\left(\rho_{\mathrm{R}}(\mathbf{r}) - \frac{1}{2}\sum_{\alpha=1}^{n} \int \mathrm{d}^2u\, \psi_\alpha^2(\mathbf{r},\mathbf{u})\right) \\ &\quad \times\delta\left(S^{ij}(\mathbf{r}) - \frac{1}{2}\sum_{\alpha=1}^{n} \int \mathrm{d}^2u \left(u^i u^j - \frac{1}{3}\delta^{ij}\right) \psi_\alpha^2(\mathbf{r},\mathbf{u})\right). \end{aligned} \tag{A.38}$$

The subsequent integrations over $\rho_{\mathrm{C}}(\mathbf{r}), \rho_{\mathrm{R}}(\mathbf{r})$ and $S^{ij}(\mathbf{r})$ yield the final field theoretic representation of the grand canonical partition function

$$\begin{aligned} Z(\mu,\epsilon,\sigma) &= \lim_{n\to 0} \prod_{\alpha=1}^{n} \int \mathcal{D}\psi_\alpha \mathcal{D}\varphi_\alpha \left[\int \mathrm{d}^3r\, \mathrm{d}^2u\, \psi_1(\mathbf{r},\mathbf{u})\right] \left[\int \mathrm{d}^3r'\, \varphi_1(\mathbf{r}')\right] \\ &\times \exp\left\{ -\frac{1}{2}\sum_{\alpha=1}^{n} \int \mathrm{d}^3r\, \mathrm{d}^2u\, \psi_\alpha(\mathbf{r},\mathbf{u}) \Big[\beta(\mu-\epsilon) - \frac{b^2\left(\mathbf{u}\cdot\nabla_r\right)^2}{\beta(\mu-\epsilon)}\Big] \psi_\alpha(\mathbf{r},\mathbf{u}) \right. \\ &- \frac{1}{2}\sum_{\alpha=1}^{n} \int \mathrm{d}^3r \varphi_\alpha(\mathbf{r}) \Big[\beta\mu - \frac{b^2}{6}\nabla_r^2\Big] \varphi_\alpha(\mathbf{r}) \\ &- \frac{\chi}{4} \int \mathrm{d}^3r \left[\sum_{\alpha=1}^{n} \int \mathrm{d}^2u\, \psi_\alpha^2(\mathbf{r},\mathbf{u})\right]^2 \\ &- \frac{v}{8} \int \mathrm{d}^3r \left[\sum_{\alpha=1}^{n} \int \mathrm{d}^2u\, \psi_\alpha^2(\mathbf{r},\mathbf{u}) + \sum_{\alpha'=1}^{n} \varphi_{\alpha'}^2(\mathbf{r})\right]^2 \end{aligned} \tag{A.39}$$

$$
\begin{aligned}
&- \frac{w}{48}\int \mathrm{d}^3 r \left[\sum_{\alpha=1}^{n}\int \mathrm{d}^2 u\, \psi_\alpha^2(\mathbf{r},\mathbf{u}) + \sum_{\alpha'=1}^{n}\varphi_{\alpha'}^2(\mathbf{r})\right]^3 \\
&+ \sigma^{1/2}\sum_{\alpha=1}^{n}\int \mathrm{d}^3 r\, \mathrm{d}^2 u\, \psi_\alpha(\mathbf{r},\mathbf{u})\varphi_\alpha(\mathbf{r}) \\
&- \left.\frac{g}{4}\sum_{\alpha=1}^{n}\sum_{\alpha'=1}^{n}\int \mathrm{d}^3 r\, \mathrm{d}^2 u\, \mathrm{d}^2 u'\, P_2(\mathbf{u}\cdot\mathbf{u}')\, \psi_\alpha^2(\mathbf{r},\mathbf{u})\, \psi_{\alpha'}^2(\mathbf{r},\mathbf{u}')\right\}, \qquad \text{(A.39)}
\end{aligned}
$$

where the second Legendre polynomial is given by

$$
P_2(\mathbf{u}\cdot\mathbf{u}') = \frac{1}{2}\left(3\cos^2\theta - 1\right). \qquad \text{(A.40)}
$$

Eq.(A.39) is the same as Eq.(6.16) in Section 6.3, which is further evaluated using the self-consistent field treatment.

B. Numerical methods

In this appendix the adaptive finite element method implemented in the program package Gascoigne [58] is briefly described. A detailed mathematical discussion of the numerical methods can be found in [59].

B.1. Variational formulation and Newton's method

The given boundary value problem is transformed into a variational problem. How this is done is explained with a simple example. Consider the PDE in the region G

$$-\nabla_r^2 u(\mathbf{r}) + u^2(\mathbf{r}) = f(\mathbf{r}), \tag{B.1}$$

with $u = \nabla_r u = 0$ on the boundary of G. Multiplying Eq.(B.1) with a test function $v(\mathbf{r})$ that vanishes at the boundary and integrating over G gives

$$\begin{aligned} & \int_{(G)} \mathrm{d}^2 r \, \left(-\nabla_r^2 u + u^2\right) v = \int_{(G)} \mathrm{d}^2 r \, f v \\ \Leftrightarrow \quad & \int_{(G)} \mathrm{d}^2 r \, \left[(\nabla_r u)(\nabla_r v) + u^2 v\right] = \int_{(G)} \mathrm{d}^2 r \, f v. \end{aligned} \tag{B.2}$$

Eq.(B.2) is now a variational formulation of the boundary value problem given by Eq.(B.1). For this example Eq.(B.2) is non-linear. This is also the case for the corresponding variational formulations of Eqs.(6.35, 6.36, 6.37) which describe the rod-coil copolymer with variable composition.

The solution for u is iteratively approximated by Newton's method which yields a set of linear equations for each iteration step. This set of linear equations is then solved with the finite element method. The following notation is convenient

$$A(u,v) \equiv \int_{(G)} \mathrm{d}^2 r \, \left[(\nabla_r u)(\nabla_r v) + u^2 v\right] \tag{B.3}$$

$$F(v) \equiv \int_{(G)} \mathrm{d}^2 r \, f v. \tag{B.4}$$

$A(u, v)$ and $F(v)$ can also be regarded as general functionals obtained by the procedure described above.

The starting point of the Newton scheme is an arbitrary initial guess u^0 that fulfils the boundary conditions. For each iteration k, u^{k+1} can then be found by solving

$$\begin{aligned} A'(u^k, \Delta u, v) &= F(v) - A(u^k, v) && \text{(B.5)} \\ u^{k+1} &= u^k + \Delta u, && \text{(B.6)} \end{aligned}$$

where $A'(u^k, \Delta u, v)$ is a shorthand notation for

$$A'(u^k, \Delta u, v) = \frac{\partial}{\partial s} A(u^k + s\Delta u, v)\bigg|_{s=0} . \tag{B.7}$$

The derivative of A can be understood as a directional derivative in the direction of Δu, which is the direction of search for Newton's method. For the example variational problem (Eq.(B.2)) A' is given by

$$A'(u^k, \Delta u, v) = \int_{(G)} \mathrm{d}\mathbf{r} \, \left[(\nabla_r \Delta u)(\nabla_r v) + 2u^k \Delta u v \right] . \tag{B.8}$$

For each iteration step, Eq.(B.5) is solved for Δu with the finite element method. Note, that Eq.(B.5) is linear in Δu.

B.2. Finite element method

For the finite element method a mesh is generated on which the problem is discretised. After each iteration step of Newton's method the mesh is refined, this refinement will be described below.

As an ansatz for Δu in G,

$$\Delta u(\mathbf{r}) = \sum_i u_i v_i(\mathbf{r}) \tag{B.9}$$

is chosen, where i runs over all nodes of the mesh. The test functions $v_i(\mathbf{r})$ are chosen such that they are equal to 1 at position $\mathbf{r}_i$ of node i and equal to 0 at the positions of all other nodes. Between node i and all neighbouring nodes $v_i(\mathbf{r})$ decreases linearly from 1 to 0. The discrete set of test functions $\{v_i\}$ is thus fully determined by the choice of the mesh. The coefficients u_i are unknown and must be determined.

The linear equation (B.5) must be fulfilled for all test functions v_i. This yields the linear system of equations

$$\mathbf{M}\mathbf{u} = \mathbf{b}, \tag{B.10}$$

where the components of the vector $\mathbf{u}$ are the u_i and the components of $\mathbf{b}$ are given by

$$b_j = F(v_j) - A(u^k, v_j). \tag{B.11}$$

The elements of the matrix $\mathbf{M}$ are given by

$$M_{ij} = A'(u^k, v_i, v_j). \tag{B.12}$$

For the example variational problem (Eq.(B.2)) M_{ij} is given by

$$M_{ij} = \int_{(G)} \mathrm{d}\mathbf{r}\, \left[(\nabla_r v_i)(\nabla_r v_j) + 2u^k v_i v_j\right]. \tag{B.13}$$

The integrals in Eq.(B.12) are calculated with a Gauss integration formula using four sampling points for each cell of the mesh.

The solution $\mathbf{u}$ of this linear system of equations determines Δu and u^{k+1}.

This procedure is iterated a certain number of times. Each time the mesh is refined in some areas and coarsened in others. These regions are chosen according to the local error of u^k. The error is estimated basically by inserting $u^k(\mathbf{r})$ into the original PDE, Eq.(B.1), and calculating the residuals at the positions of the nodes. In the areas with a high error the mesh is refined and in the areas with a very low error the mesh is coarsened. Using this process, the total number of nodes is constrained within a certain interval, therefore a coarsening in some regions is necessary to allow refining in other regions. Generally, the local error is large in regions where the gradient of the solution is large and small in regions where the gradient is small. This yields a very dense mesh in regions over which u changes strongly and a very coarse mesh in regions where u is almost constant. For the copolymer globule considered in Chapter 8 this means, that the mesh is very fine in the surface layer and very coarse around the centre of the globule where the fields and hence the density is roughly constant. As an example, Fig.(B.1) shows a section of a highly adapted mesh together with the intensity of ψ_0.

B.3. Additional remarks

Gascoigne was used to solve the boundary value problem which models a rod-coil copolymer with variable composition, given by Eqs.(6.35, 6.36, 6.37) together with

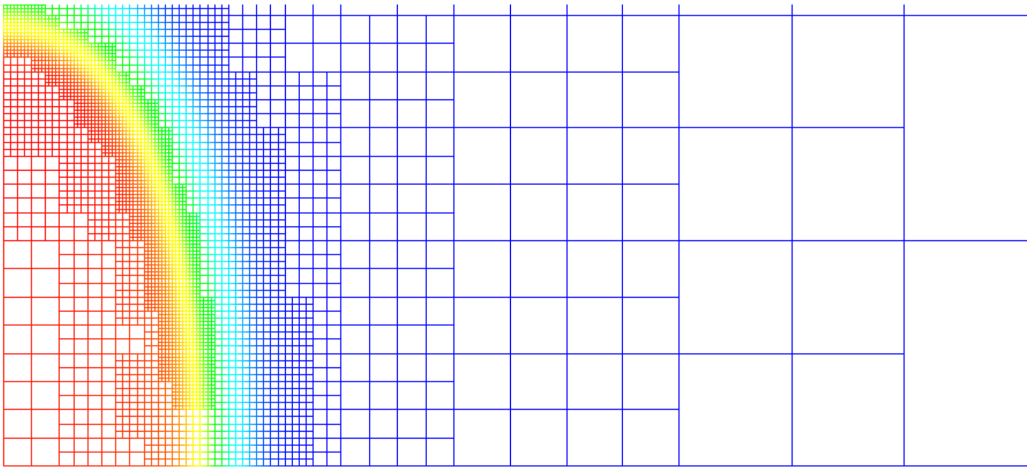

Figure B.1: Section of a highly adapted mesh. The colour coded plot on top of the mesh shows the intensity of ψ_0. The parameters are the same as the ones in the bottom two pictures in Fig.(8.12).

the boundary conditions in Eq.(6.38). In a numerical treatment the region on which the equations live has to be finite. The boundary conditions in Eq.(6.38) fix the values of the fields and their derivatives at infinity. The region which was used in the computation had therefore to be chosen large enough to ensure that the finite boundary did not influence the numerical solutions of Eqs.(6.35, 6.36, 6.37) in a significant way. It was checked that the region was always large enough, that slightly extending or reducing it did not change the numerical solutions.

For many results presented in Chapter 8 one of the parameters of the model (for instance χ) was changed over a large interval. For each step, the chemical potential μ was adjusted in order to adjust N. This was done in very small steps, where each step corresponded to one iteration in Newton's method. By choosing the steps small enough to ensure that the solution changes only slightly from one step to the next, it was possible to reach a very high accuracy, even with only one iteration per step. A typical number of steps for one of the curves in Fig.(8.21) was between $10^4 - 10^5$. By changing a parameter in discrete steps and by also adjusting μ in discrete steps it is, of course, not possible to keep N exactly fixed at one value. The stepwise adjustment of μ ensured that N stayed within a small interval around the desired value. From one step to the next N usually changes by less than 1%. All other computed values and also the corresponding parameters were then estimated for the chosen fixed N by linear interpolation.

Bibliography

[1] A.Y. Grosberg and A.R. Khokhlov, *Giant Molecules*, Academic Press, San Diego 1997

[2] B. Alberts, D. Bray, and J. Lewis, *Molecular Biology of the Cell*, 3rd edition, Garland Publishing Co., New York 1994

[3] S.I. Stupp, V. LeBonheur, K. Walker, L.S. Li, K.E. Huggins, M. Kesser, and A. Amstutz, Science **276**, 384 (1997);

[4] L.H. Radzilowski, B.O. Carragher, S.I. Stupp, Macromolecules **30**, 2110 (1997)

[5] S.A. Jenecke and X.L. Chen, Science **279**, 1903 (1998); S.A. Jenecke and X.L. Chen, Science **283**, 283 (1999)

[6] M. Lee, D.-W. Lee, B.-K. Cho, J.-Y. Yoon, and W.-C. Zin, J. Am. Chem. Soc. **120**, 13258 (1998); M. Lee, B.-K. Cho, Y.-G. Jang, and W.-C. Zin, J. Am. Chem. Soc. **122**, 7449 (2000); M. Lee, B.-K. Cho, N.-K. Oh, and W.-C. Zin, Macromolecules **34**, 1987, (2001)

[7] M. Lee, B.-K. Cho, and W.-C. Zin, Chem. Rev. **101**, 3869 (2001);

[8] A.Y. Grosberg and A.R. Khokhlov, *Statistical Physics of Macromolecules*, AIP Press, New York 1994

[9] M. Rubinstein and R.H. Colby, *Polymer Physics*, Oxford University Press, Oxford 2003

[10] M. Doi and S.F. Edwards, *The Theory of Polymer Dynamics*, Oxford University Press, Oxford 1986.

[11] C. Nowak and T.A. Vilgis, Europhys. Lett. **68**, 44 (2004).

[12] C. Nowak, V.G. Rostiashvili, and T.A. Vilgis, Macromol. Chem. Phys. **206**, 112 (2005).

[13] C. Nowak and T.A. Vilgis, J. Chem. Phys. *in print* (2006).

[14] C. Nowak, V.G. Rostiashvili, and T.A. Vilgis, Europhys. Lett. **74**, 76 (2006).

[15] P.J. Flory, J. Chem. Phys. **17**, 303 (1949).

[16] J.C. Le Guillou and J. Zinn-Justin, Phys. Rev. Lett. **39**, 95 (1977).

[17] M. Rief, F. Oesterhelt, B. Heymann, and H. Gaub, Science **275**, 1295 (1997).

[18] H. Li, M. Rief, F. Oesterhelt, and H. Gaub, Advanced Materiels **10**, 316 (1998).

[19] A. Courvoisier, F. Isel, J. Francois, and J. Maaloum, Langmuir **14**, 3727 (1998).

[20] H. Li, A.F. Oberhouser, S.B. Fowler, J. Clarke, and J.M. Fernandez, Proc. Natl. Acad. Sci. USA **97**, 6527 (2000).

[21] R. Merkel, Physics Reports **346**, 344 (2001).

[22] M. Kellermayer, S. Smith, H. Granzier, and C. Bustamante, Science **276**, 1112 (1997).

[23] L. Tskhovrebova, J. Trinick, J. A. Sleep, and R.M. Simmons, Nature (London) **387**, 308 (1997).

[24] J. Liphardt, B. Onoa, S. Smith, I. Tinoco Jr., and C. Bustamante, Science **292**, 733 (2001).

[25] A. Halperin and E.B. Zhulina, Europhys. Lett. **15**, 417 (1991).

[26] P. Pincus, Macromolecules **9**, 386 (1976).

[27] F. Dowell, Phys. Rev. A **28**, 3520, 3526 (1983).

[28] A.N. Semenov and S.V. Vasilenko, Sov. Phys. JETP **63**, 70 (1986).

[29] A. Halperin, Europhys. Lett. **10**, 549 (1989).

[30] A. Halperin, Macromolecules **23**, 2724 (1990).

[31] T.A. Vilgis and A. Halperin, Macromolecules **24**, 2090 (1991).

[32] D.R.M. Williams and G.H. Fredrickson, Macromolecules **25**, 3561 (1992).

[33] R. Holyst and M. Schick, J. Chem. Phys. **96**, 721, 730 (1992).

[34] R. Holyst and T.A. Vilgis, Macromol. Theory Simul. **5**, 573 (1996).

[35] A. Liu and G.H. Fredrickson, Macromolecules **26**, 2817 (1993).

[36] M.W. Matsen and C. Barrett, J. Chem. Phys. **109**, 4108 (1998).

[37] P. Friedel, A. John, D. Pospiech, D. Jehnichen, and R.R. Netz, Macromol. Theory Simul. **11**, 785 (2002).

[38] A.Y. Grosberg and A.R. Khokhlov, Adv. Polym. Sci. **41**, 53 (1981).

[39] A.N. Semenov and A.V. Subbotin, Sov. Phys. JETP **74**, 660 (1992).

[40] M. Daoud, M and J.P. Cotton, J. Phys. (Les Ulis, Fr.) **43**, 531 (1982).

[41] P.G. de Gennes, *Scaling Concepts in Polymer Physics*, Cornell Univ. Press, New York 1979.

[42] S.F. Edwards and P.J. Singh, J. Chem. Soc. Faraday Trans. II **75**, 1001 (1979).

[43] J. des Cloizeaux and G. Jannink, *Polymers in Solution*, Clarendon Press, Oxford 1990.

[44] T.A. Witten and P.A. Pincus, Macromolecules **19**, 2509 (1986).

[45] S. Alexander, J. Phys. (Les Ulis, Fr) **38**, 983 (1977).

[46] G.H. Fredrickson and L. Leibler, Macromolecules **23**, 531 (1990).

[47] S.V. Panyukov and Y. Rabin, Phys. Rep. **269**, 1 (1996).

[48] A.L. Kholodenko and K. F. Freed, J. Phys. A: Math Gen. **17**, 2703 (1984).

[49] K.F. Freed, Adv. Chem. Phys. **22**, 1 (1972).

[50] C.G. Gray and K.E. Gubbins, *Theory of Molecular Fluids*, v.1: Fundamentals, Clarendon press, Oxford 1984.

[51] P.G. de Gennes and J. Prost, *The Physics of Liquid Crystals*, Clarendon Press, Oxford 1993.

[52] D. Poland and H.A. Scheraga, *Theory of Helix - Coil Transitions in Biopolymers*, Academic Press, New York 1970.

[53] H. S. Chan and K. A. Dill, Proc. Natl. Acad. Sci. USA **87**, 6388 (1990); D. P. Yee, H. S. Chan, T. F. Havel, and K. A. Dill, J. Mol. Biol. **241**, 557 (1994);

[54] N. D. Socci, W. S. Bialek, and J. N. Onuchic, Phys. Rev. E **49**, 3440 (1994).

[55] B.H. Zimm and I.K. Bragg, J. Chem. Phys. **31**, 526 (1959).

[56] http://www.pdb.org

[57] A.G. Murzin, S.E. Brenner, T. Hubbard, and C. Chothia, J. Mol. Biol. **247**, 536 (1995).

[58] http://www.gascoigne.uni-hd.de

[59] W. Bangerth and R. Rannacher, *Adaptive Finite Element Methods for Differential Equations*, Birkhäuser, Basel 2003.

[60] Y. Zhou and M. Karplus, PNAS **94**, 14429 (1997)

[61] O.B. Ptitsyn, Adv. Prot. Chem. **47**, 83 (1995)

[62] S.I. Stupp et al., MRS Bull. **25**, 42 (2000).

[63] M. Sayar and S.I. Stupp, Macromolecules **34**, 7135 (2001).

[64] T.A. Vilgis, A. Johner, and J.-F. Joanny, Phys. Chem. Chem. Phys. **1**, 2077 (1999).

[65] E.M. Sevick and D.R.M. Williams, Colloids Surf A. **130**, 387 (1997).

[66] A.M. Donald and A.H. Windle, *Liquid Crystalline Polymers*, Cambridge University Press, Cambridge 1992.

[67] W. Maier and A. Saupe, Z. Naturf. **14a**, 882 (1959); **15a**, 287 (1960).

[68] A.V. Smith and C.K. Hall, Proteins **44**, 344 (2001).

[69] J. Ireta, J. Neugebauer, M. Scheffler, A. Rojo, and M. Galvan, J. Phys. Chem. B **107**, 1432 (2003).

[70] J.J.L.M. Cornelissen, Pure Appl. Chem. **74**, 2021 (2002).

[71] J.S. Crespo, S. Lecommandoux, R. Borsali, H.-A. Klok, and V. Soldi, Macromolecules **36**, 1253 (2003).

[72] A.A. Vedenov, A.M. Dykhne, and M.D. Frank-Kamenetski, Soviet Physics Usp. **14**, 715 (1972).

[73] O. Farago and P. Pincus, Eur. Phys. J. E **7**, 393 (2002).

[74] A. Buhot and A. Halperin, Europhys. Lett. **23**, 1 (1993).

[75] M.N. Tamashiro and P. Pincus, Phys. Rev. E **63**, 021909 (2001).

[76] S. Tanaka and H.A. Scheraga, Macromolecules **9**, 142, 159, 168 (1976).

[77] N.S. Skantzos, J. van Mourik, and A.C.C. Coolen, J. Phys. A.: Math. Gen. **34**, 4437 (2001).

[78] M. Vasquez, M.R. Pincus, and H.A. Scheraga, Biopolymers **26**, 351 (1987).

[79] V.N. Uversky and A.L. Fink, FEBS Letters **515**, 79 (2002).

[80] A. Sikorski and P. Romiszowski, Biopolymers **69**, 391 (2003).

[81] C. Clementi, A.E. Garcia, and J.N. Onuchic, J. Mol. Biol. **326**, 933 (2003).

[82] U. Mayor, N.R. Guydosh, C.M. Johnson, J.G. Grossmann, S. Sato, G.S. Jas, S.M.V. Freund, D.O.V. Alonso, V. Daggett, and A.R. Fersht, Nature, **421**, 863 (2003).

[83] V.S. Pande, A.Y. Grosberg, and T. Tanaka, Rev. Mod. Phys. **72**, 259 (2000).

[84] J. des Cloizeaux, J. de Physique **36**, 281 (1975).

[85] M. Reenders and G. ten Brinke, Macromolecules **35**, 3266 (2002).

[86] A.M. Gupta and S.F. Edwards, J. Chem. Phys. **98**, 1588 (1993).

[87] R.N. Netz and M. Schick, Phys. Rev. Lett. **77**, 302 (1996).

[88] H.N.W. Lekkerkerker and G.J. Vroege, Phil. Trans. R. Soc. Lond. A **344**, 419 (1993); A.M. Gupta and S.F. Edwards, J. Chem. Phys. **344**, 419 (1993).

[89] A.N. Semenov and A.R. Khokhlov, Sov. Phys. Usp. **31**, 988 (1989).

[90] E. Pitard, T. Garel, and H. Orland, J. Phys. I France **7**, 1201 (1997).

[91] Y.M. Kim and P.Pincus, Biopolymers **18**, 2315 (1979).

[92] Z. Luthey-Schulten, B.E. Ramirez, and P.G. Wolynes, J. Phys. Chem. **99**, 2177 (1995).

[93] J.G. Saven and P.G. Wolynes, J. Mol. Biol. **257**, 199 (1996).

[94] I.R. Cooke, Ph.D. thesis, Australian National University, Canberra 2003.

[95] N. Lee and T.A. Vilgis, Europhys. Lett. **57**, 817 (2002); N.-K. Lee and T.A. Vilgis, Eur. Phys. J. B **28**, 451 (2002).

[96] N.-K. Lee and T.A. Vilgis, Phys. Rev E **67**, 050901 (2003).